Numerical Modeling of Liquefaction-induced Settlement due to Reconsolidation

by

Devdeep Basu

A dissertation submitted to the Graduate Faculty of
Auburn University
in partial fulfillment of the
requirements for the Degree of
Doctor of Philosophy

Auburn, Alabama
August 7, 2021

Keywords: liquefaction, numerical modeling, reconsolidation, settlement, spatial variability

Approved by

Jack Montgomery, Chair, Assistant Professor, Department of Civil Engineering
Brian Anderson, Associate Professor, Department of Civil Engineering
Justin D. Marshall, Associate Professor, Department of Civil Engineering
Lorraine Wolf, Professor, Department of Geosciences

ACKNOWLEDGEMENTS

With immense gratitude I would like to acknowledge the support, help and encouragement of my advisor Dr. Jack Montgomery, Department of Civil Engineering, Auburn University. I sincerely thank him for constantly conveying a spirit of enthusiasm in regard to research.

I owe my gratitude to the members of my doctoral committee, Dr. Brian Anderson, Dr. Justin D. Marshall, Dr. Lorraine Wolf and the University Reader for my dissertation, Dr. Robert Pantazes for their precious suggestions in completing this work.

I am grateful to Mary Beth, Katie and Debbie for all the administrative help that enabled me to carry out my work smoothly.

I would also like to thank my colleagues Michael, Antonio, Dan, Dinu, Mengwei, Ashton, Patricia, Chukwuma for all their help in the past four years.

I would like to express my deep sense of gratitude to my parents and my sister for their unconditional love and support. This journey would not have been possible without them.

TABLE OF CONTENTS

ACKNOWLEDGEMENTS ii

LIST OF FIGURES vii

LIST OF TABLES xvi

ABSTRACT xvii

CHAPTER 1: INTRODUCTION 1

1.1 LIQUEFACTION BACKGROUND 1

1.2 LIQUEFACTION TRIGGERING CRITERIA 2

1.3 ASSESSMENT OF LIQUEFACTION-INDUCED SETTLEMENTS 5

1.4 SPATIAL VARIABILITY 8

1.5 PM4SAND: BRIEF INTRODUCTION 10

1.6 FLAC: BRIEF INTRODUCTION 12

1.7 REASONSING BEHIND CHOICE OF FLAC AND PM4SAND 14

1.8 2D VERSUS 3D NUMERICAL MODELING APPROACH: ADVANTAGES AND LIMITATIONS 16

1.9 MOTIVATION AND GOALS 16

1.10 RESEARCH OBJECTIVES 17

1.11 DISSERTATION ORGANIZATION 18

CHAPTER 2: OBSERVATIONS AND CHALLENGES IN SIMULATING POST-LIQUEFACTION RECONSOLIDATION SETTLEMENTS FROM CENTRIFUGE AND SHAKE TABLE TESTS 20

2.1 ABSTRACT 20

2.2 INTRODUCTION 21

2.3 CENTRIFUGE AND SHAKE TABLE EXPERIMENTS 22
2.4 NUMERICAL MODELING 24
2.4.1 Constitutive Model 26
2.4.2 Soil-specific Calibration 28
2.4.3 Hydraulic Conductivity 30
2.4.4 Input Motions 34
2.5 RESULTS 37
2.5.1 Simulation of Centrifuge Tests 37
2.5.2 Simulation of Shake Table Tests 42
2.6 DISCUSSION 44
2.7 CONCLUSIONS 49
CHAPTER 3: INVESTIGATION OF THE KEY ISSUES IN SIMULATING CENTRIFUGE EXPERIMENTS ON A SHEET-PILE WALL EMBEDDED IN A LIQUEFIABLE SAND .. 52
3.1 ABSTRACT 52
3.2 INTRODUCTION 53
3.3 BRIEF DESCRIPTION OF CENTRIFUGE MODEL TESTS 55
3.4 NUMERICAL MODEL 57
3.4.1 Calibration 57
3.4.2 Input Motions 59
3.4.3 Simulation Procedure and Boundary Conditions 60
3.5 SIMULATION RESULTS 63
3.5.1 Detailed Results for RPI-9 64
3.5.2 Effect of Permeability 69

3.5.3 Effect of D_R 72
3.5.4 Discussion on Wall Displacement: Numerical and Centrifuge Comparison 76
3.6 DISCUSSION AND CONCLUDING REMARKS 80
CHAPTER 4: NUMERICAL MODELING OF RECONSOLIDATION SETTLEMENTS FOR A SPATIALLY VARIABLE SOIL DEPOSIT 84
4.1 ABSTRACT 84
4.2 INTRODUCTION 85
4.3 DESCRIPTION OF THE HOLLYWOOD TEST SITE 86
4.4 NUMERICAL MODELING 90
4.4.1 Soil Properties and PM4Sand Calibration 91
4.4.2 Input Motions 95
4.5 RESULTS 98
4.5.1 Excess Pore Pressure Response 99
4.5.2 Shear Strain Response 106
4.5.3 Reconsolidation and Differential Settlement 114
4.5.4 Correlation between Input Motion Parameters CAV_5, *ASI* and Reconsolidation Settlement 121
4.5.5 Sensitivity Analyses 123
4.6 SUMMARY AND CONCLUDING REMARKS 126
CHAPTER 5: SUMMARY, CONCLUSIONS AND FUTURE RESEARCH 129
5.1 SUMMARY AND CONCLUSIONS 129
5.2 FUTURE RESEARCH 134
CHAPTER 6: REFERENCES 136

6.1 REFERENCES (CHAPTER 1)..... 136

6.2 REFERENCES (CHAPTER 2)..... 141

6.3 REFERENCES (CHAPTER 3)..... 145

6.4 REFERENCES (CHAPTER 4)..... 148

LIST OF FIGURES

Figure 1-1: (a) Liquefaction-induced foundation failure of Kawagishi-cho apartment buildings during the 1964 Niigata earthquake (Source: Kramer 2013) and (b) consequences of liquefaction following the 2011 Christchurch earthquake in New Zealand (Source: www.geotech.hr) 3

Figure 1-2: Typical stress-strain and pore pressure responses observed during a cyclic direct simple shear loading (El Ghoraiby and Manzari 2020): (a) shear stress versus shear strain response, variation of (b) r_u and (c) shear strain with number of loading cycles 5

Figure 1-3: Ishihara and Yoshimine (1992) correlation between volumetric stain and maximum shear strain at various relative densities 6

Figure 1-4: (a) Centrifuge apparatus at Rensselaer Polytechnic Institute (Ha et al. 2006) and (b) a shake table apparatus (Srilatha et al. 2013) 7

Figure 1-5: Schematic of the rotated dilatancy line added to PM4Sand along with the yield, critical, dilatancy and bounding lines in q-p space (Source: Boulanger and Ziotopoulou 2017). Relative location of dilatancy and bounding lines corresponds to dense-of-critical states of stress 11

Figure 1-6: FLAC model to monitor horizontal displacements in a sand deposit retained by a sheet-pile wall structure 14

Figure 2-1: Typical FLAC meshes for (a) full-scale 2D model and (b) 1D column from the center of the 2D model highlighting pore pressure transducers (PPTs) and settlement sensors (LVDTs). Note: W and H correspond to the width and height, respectively, from the experiments as stated in Table 2-1 25

Figure 2-2: Volumetric strain versus maximum shear strain from single-element cyclic DSS simulations compared to Ishihara and Yoshimine (1992) curves. Simulations are for a relative density of 35% with a G_o of 476 and an h_{po} of 0.53 after Boulanger and Ziotopoulou (2017) 27

Figure 2-3: Liquefaction triggering curves developed from fitting experimental data on (a) Hostun (b) Ottawa F-65 and (c) Monterey sands that are used for h_{po} calibration. The cyclic stress ratio (CSR) corresponds to 15 cycles of sinusoidal loading in cyclic DSS test. Symbols correspond to experimental data and solid lines represent the simulation data fit..... 29

Figure 2-4**:** Soil-specific calibration of reconsolidation parameter $f_{sed,min}$ for Hostun sand using data from Adamidis and Madabhushi (2016) 30

Figure 2-5: Relationship between α and D_{10} developed based on numerical simulations of experiments for five different sands. The power law correlation fit is based upon the results from the present study while the results from other numerical and experimental studies are also shown. The 95% confidence interval on the best fit relationship is highlighted with hatched lines 34

Figure 2-6: Acceleration time histories used as input motions for the experiments by (a) Adamidis and Madabhushi (2018) (b) Ramirez et al. (2018) (c) Mehrzad et al. (2018) (d) Ecemis (2021) (e) Thevanayagam et al. (2009) 36

Figure 2-7: Excess pore pressure time histories for the centrifuge tests on (a) Hostun sand – CK model (b) Hostun sand – VK model (c) Ottawa F-65 sand – CK model (d) Ottawa F-65 sand – VK model (e) No. 306 sand – CK model (f) No. 306 sand – VK model. Dashed lines represent the experiment and solid lines represent the simulations 39

Figure 2-8: Dynamic phase excess pore pressure time histories compared between the numerical simulation and experiment considering a D_r of 90% for the dense Ottawa F-65 sand layer (as reported) and the CK model. Dashed lines represent the experiment and solid lines represent the simulations 40

Figure 2-9: Settlement time histories for the centrifuge tests on (a) Hostun sand – default reconsolidation calibration (b) Hostun sand – modified reconsolidation calibration (c) Ottawa F-65 sand (d) No. 306 sand 41

Figure 2-10: Time histories of total settlement for Adamidis and Madabhushi (2018) centrifuge tests and numerical simulations from the sensitivity analysis study using half timestep (HT), half mesh size (HM) and 2D mesh 42

Figure 2-11: Excess pore pressure time histories for the shake table tests on (a) M-1 sand sand – CK model (b) M-1 sand – VK model (c) Ottawa F-55 sand – CK model (d) Ottawa F-55 sand – VK model. Dashed lines represent the experiment and solid lines represent the simulations 43

Figure 2-12: Settlement time histories for the shake table tests on (a) M-1 sand (b) Ottawa F-55 sand 44

Figure 2-13: Normalized settlements from simulations using the (a) CK model and the (b) VK model compared to the normalized experimental settlements 46

Figure 2-14: Correlation between observed bias and (a) D_{50} (b) D_{10} for each test considered in this study 47

Figure 3-1: Geometry of the numerical setup in FLAC (prototype scale). The locations of the sensors correspond to RPI-9 56

Figure 3-2: Triggering relationship for Ottawa F-65 sand used for calibrating PM4Sand parameters 59

Figure 3-3: Acceleration-time histories and response spectra (5% damped) for horizontal components of the RPI motions 60

Figure 3-4: Excess pore pressure time histories at the end of dynamic phase for test RPI-9 at sensors: (a) PB3 (b) PM2 (c) PW1 (d) PD (e) PFWB. Dashed lines represent excess pore pressure corresponding to a r_u of 100% 66

Figure 3-5: Response spectra (5% damped) at the end of dynamic phase for test RPI-9 at sensors: (a) AHB1 (b) AHM2 (c) AHW3 (d) AHD (e) AHFW 67

Figure 3-6: (a) Wall displacement and (b) surface settlement time histories at the end of dynamic shaking for RPI-9 68

Figure 3-7: Wall displacement time histories at sensor WY_{-T}/WY_{+T} for RPI-9 from the sensitivity analysis using the baseline simulation, simulations with half the baseline timestep and half the baseline mesh size 68

Figure 3-8: Excess pore pressure time histories for different cases of permeability (simulations use mass-based D_R) at sensors (a) PB3 (b) PW1. Dashed lines represent excess pore pressure corresponding to a r_u = 100% 71

Figure 3-9: (a) Wall displacement and (b) surface settlement time histories for different cases of permeability (simulations use mass-based D_R) 71

Figure 3-10: Excess pore pressure time histories at sensor PW1 for the five RPI tests. Dashed lines represent excess pore pressure corresponding to a r_u = 1 73

Figure 3-11: Response spectra (5% damped) at sensor AHW3 for the five RPI tests 74

Figure 3-12: Wall displacement time histories at sensor WY_{-T}/WY_{+T} for the five RPI tests 75

Figure 3-13: Settlement time histories at sensor WY-/WY+ for the five RPI tests..... 76

Figure 3-14: Normalized wall displacements at sensor WY_{-T}/WY_{+T} for each of the 11 centrifuge tests (KyU-1 and KyU-3 do not have CPT data). Solid symbols correspond to the mass-based D_R values while hollow symbols correspond to lower and upper bounds of CPT-based D_R 78

Figure 3-15: Normalized wall displacement vs relative density for (a) simulations and (b) experiments corresponding to RPI tests. Solid symbols correspond to the mass-based D_R values while hollow symbols correspond to lower and upper bounds of CPT-based D_R 79

Figure 4-1: Plan view of the Hollywood test site showing the locations of the various explorations performed (modified from Bong and Stuedlein 2018)..... 87

Figure 4-2: (a) Cross-section of the general soil profile at Hollywood site along with the FLAC mesh and (b) cone tip resistance (q_c) measurements at two locations through CPT tests (based on Stuedlein and Bong 2017) 88

Figure 4-3: q_{c1Ncs} distribution at two sections at distances of 1 m (Section 5) and 2.75 m (Section 12) in the EW direction..... 89

Figure 4-4: Cumulative distribution function of q_{c1Ncs} for each of the 13 sections at Hollywood 89

Figure 4-5: Boulanger and Idriss (2016) liquefaction triggering curve used for h_{po} calibration. The cyclic stress ratio (CSR) corresponds to 15 cycles of sinusoidal loading in cyclic DSS test 93

Figure 4-6: Some typical input motions used in this study: (a) a ramped sinusoidal input motion with a peak acceleration of 0.25g and three linearly-scaled transient motions: (b) M1 - Imperial Valley-06 (M1) (c) M4 - Helena, Montana-01(d) M7 – Sitka, Alaska 97

Figure 4-7: Response spectra for the transient motions used in this study scaled to a peak acceleration of 0.25g 98

Figure 4-8: Excess pore pressure time histories for the stochastic section 12 (2.75 m in EW direction) under ramped sinusoidal motions at three different peak accelerations of (a) 0.13g (b) 0.25g (c) 0.4g. The dashed black lines correspond to a r_u of 1 at the three depths 99

Figure 4-9: r_u distribution in stochastic section 12 at the end of shaking using the ramped sinusoidal motions at peak accelerations of (a) 0.13g (b) 0.25g and (c) 0.4g 100

Figure 4-10: Excess pore pressure time histories at a depth of 7.75 m within the stochastic section 12 using ramped sinusoidal motion having a peak acceleration of 0.25g. The dashed black line corresponds to a r_u of 1 101

Figure 4-11: r_u distribution in stochastic section 12 at the end of shaking using the motions (a) M1 (b) M4 and (c) M7. All motions correspond to an acceleration level of 0.25g..... 103

Figure 4-12: r_u distribution in stochastic section 12 at the end of shaking using the motions (a) M1 (b) M4 and (c) M7. All motions correspond to an acceleration level of 0.528g..... 104

Figure 4-13: Simulated end-of-shaking excess pore pressure histories at different depths within the liquefiable layer in section 12 (at 2.75 m in E-W direction) of the stochastic model using the 0.25g peak acceleration transient motions. The solid lines correspond to the excess pore pressure histories and dashed lines correspond to a r_u of 1..... 105

Figure 4-14: Simulated end-of-shaking excess pore pressure histories at different depths within the liquefiable layer in section 12 (at 2.75 m in E-W direction) of the stochastic model using the 0.528g peak acceleration transient motions. The solid lines correspond to the excess pore pressure histories and dashed lines correspond to a r_u of 1 106

Figure 4-15: Shear strain distribution in section 12 using ramped sinusoidal motions at peak accelerations of (a) 0.13g (b) 0.25g (c) 0.4g 109

Figure 4-16: End-of-shaking shear strain distribution in section 12 corresponding to the transient motions (a) M1 (b) M4 (c) M7. Each motion corresponds to an acceleration level of 0.25g 110

Figure 4-17: End-of-shaking shear strain distribution in section 12 corresponding to the transient motions (a) M1 (b) M4 (c) M7. Each motion corresponds to an acceleration level of 0.528g 111

Figure 4-18: Lateral variation of shear strain with q_{c1Ncs} at various depths in section 12 using ramped sinusoidal motions with peak acceleration of (a) 0.13g (b) 0.25g (c) 0.4g..... 112

Figure 4-19: Lateral variation of shear strain with q_{c1Ncs} at various depths in section 12 using transient motions (a) M1 (b) M4 (c) M7. All motions correspond to a peak acceleration of 0.25g..... 113

Figure 4-20: Lateral variation of shear strain with q_{c1Ncs} at various depths in section 12 using transient motions (a) M1 (b) M4 (c) M7. All motions correspond to a peak acceleration of 0.528g..... 114

Figure 4-21: Contours of reconsolidation settlement at Hollywood test site using ramped sinusoidal motions having peak accelerations of: (a) 0.05g (b) 0.13g (c) 0.25g and (d) 0.4g 116

Figure 4-22: Maximum values of differential settlement for each stochastic section using ramped sinusoidal motions having different peak acceleration level 117
Figure 4-23: Maximum values of simulated differential settlement across the entire surface area at the Hollywood site using ramped sinusoidal motions having various peak acceleration levels 117
Figure 4-24: Comparison of simulated mean reconsolidation settlements from the stochastic and the uniform sections to peak accelerations of the ramped sinusoidal input motion. Solid lines represent the 13 stochastic sections whereas the symbols correspond to the uniform sections 118
Figure 4-25: Simulated reconsolidation settlement profiles from the stochastic model (section 12) and uniform model (using a representative median q_{c1Ncs} value from the stochastic model) using the seven transient motions having peak accelerations of: (a) 0.25g and (b) 0.528g. The solid lines correspond to the stochastic model whereas the broken lines correspond to the uniform model 120
Figure 4-26: Comparison of simulated reconsolidation settlements from stochastic (section 12) and uniform section (using a representative median q_{c1Ncs} value from the stochastic model) at acceleration levels of (a) 0.25g and (b) 0.528g 120
Figure 4-27: Comparison of simulated reconsolidation settlements from stochastic (section 12) and uniform section (using a representative 33rd percentile q_{c1Ncs} value from the stochastic model) at acceleration levels of (a) 0.25g and (b) 0.528g 121
Figure 4-28: Correlation between the mean reconsolidation settlements observed for the stochastic model section and CAV_5 122

Figure 4-29: Correlation between the mean reconsolidation settlements observed for the stochastic model section and *ASI* 122

Figure 4-30: Correlation between the mean reconsolidation settlements observed for the uniform model and CAV_5 using (a) median and (b) 33rd percentile q_{c1Ncs} values 123

Figure 4-31: Comparison of time histories for (a) excess pore pressure generation and (b) reconsolidation settlement between the r_u – dependent variable hydraulic conductivity and the constant hydraulic conductivity simulations using ramped sinusoidal motion having a peak acceleration of 0.25g. The solid lines correspond to the constant *k* simulation whereas the dotted lines represent the variable *k* simulation 124

LIST OF TABLES

Table 1-1: PM4Sand parameters that are commonly calibrated to specific soils 12

Table 2-1: Parameters for the setup of the centrifuge experiments and shake table tests considered in the present study. The dimensions are presented in prototype units..... 23

Table 2-2: Geotechnical properties of the sands used in the numerical models for this study... 23

Table 2-3: PM4Sand calibration parameters used for the sands in the numerical simulations .. 29

Table 2-4: Variable hydraulic conductivity model parameters used for the sands considered in this study 33

Table 2-5: Statistical parameters corresponding to the numerical fit of centrifuge settlements based on the tests considered in this study..... 47

Table 2-6: Experimental and numerical settlements observed for the five different tests considered in the current study..... 48

Table 3-1: Some of the main features of the centrifuge experiments 56

Table 3-2: Relative density estimates from mass-based and CPT-based measurements in the centrifuge tests and corresponding h_{po} values selected for the numerical simulations... 58

Table 3-3: Properties of Ottawa F-65 sand utilized in the numerical simulations..... 59

Table 3-4: Statistical parameters corresponding to the numerical fit of centrifuge-observed wall displacements based on the 11 tests considered in this study 78

Table 4-1: Uniform soil properties for the non-liquefiable layers..... 93

Table 4-2: Characteristics of recorded earthquake motions considered in this study..... 96

ABSTRACT

Soil liquefaction poses a major threat to human life and property. Settlement following liquefaction has been one of the major sources of liquefaction-induced damage in past earthquakes and creating resilient infrastructure requires methods to predict this settlement for various types of soil and site conditions. Empirical methods are commonly utilized in practice to evaluate settlements. However, these methods have some inherent limitations that might hinder the accuracy of settlement predictions for specific soils and site conditions. Numerical models are a may be used to predict post-liquefaction responses of soil while accounting for the complexities encountered in the field, such as variable stratigraphy, partial drainage, and soil-structure interaction. In order to have confidence in the results of these numerical models, they must first be validated using results from physical models or well-documented case histories. Another important factor in evaluating liquefaction-induced damage is the effect of spatial variability in soil properties. Many previous studies have focused on the response of soil layers with uniform properties, but this is a simplification of the true variability encountered in the field. It is not well-understood how spatial variability in soil properties affects reconsolidation settlements, so a more in-depth assessment is required. The primary motivation for this study was to improve the existing numerical protocols for liquefaction modeling in order to accurately predict observed liquefaction responses for a range of soil types and explore important factors that influence the magnitude and distribution of reconsolidation settlements. Previous studies in this area have primarily focused on a single site or a single type of soil. This precludes the ability to examine how soil type influences settlement patterns or to assess whether a numerical protocol can predict accurate settlements under various loading paths. This study fills this gap by applying a single numerical protocol (the numerical platform Fast Lagrangian Analysis of Continua, FLAC, and constitutive model PM4Sand) to

model both excess pore pressure generation and dissipation for three types of problems (uniform centrifuge and shake table tests, centrifuge tests with a retaining wall, and a spatially variable field site) with six different types of soil. The necessity of soil-specific calibration of post-liquefaction stiffness for reliable estimation of reconsolidation strains is investigated. The importance of using an excess pore pressure ratio-dependent hydraulic conductivity to accurately model the pore pressure generation and dissipation patterns is analyzed. A new relationship between increase in hydraulic conductivity due to liquefaction and grain size diameter is proposed based on the results from this study and previous research. The importance of accurate estimation of relative density for reliable numerical predictions of post-liquefaction responses is also investigated. Overall, the displacements and settlements predicted by the numerical framework used in this study are within 50-200% of the corresponding experimental values, although this level of agreement can likely be improved through calibration of both dynamic and reconsolidation properties. This level of uncertainty is similar to those observed for other liquefaction problems by previous researchers, such as lateral spreading displacements observed in post-earthquake reconnaissance and centrifuge tests, and free-field settlements observed in numerical studies and comparisons with empirical relationships in Christchurch. Finally, the numerical methodology developed in this study is used to model a spatially variable soil deposit from Hollywood, South Carolina. The ability of the numerical framework in capturing the physical mechanisms involved in such a problem is investigated. The effects of various soil properties and input motion parameters on reconsolidation settlement are evaluated.

CHAPTER 1: INTRODUCTION

1.1 LIQUEFACTION BACKGROUND

Liquefaction is a complex and important phenomenon in geotechnical earthquake engineering that occurs as a result of cyclic loading, such as an earthquake and can lead to a complete loss in soil strength causing it to behave like a fluid [1]. Liquefaction occurs when excess pore pressures are generated in soils, resulting in simultaneous reduction in effective stress and soil stiffness. For gently sloping ground conditions, liquefaction can cause a liquefied soil mass to move downslope, (i.e., lateral spreading). Lateral spreads can extend over very large areas and can lead to catastrophic damage to structures and foundations. Even for level-ground conditions, liquefaction can result in large volumetric strains and settlements as the excess pore pressures dissipate due to outflow of pore water from the liquefied mass. This post-liquefaction soil settlement is often referred to as reconsolidation settlement. Settlement can cause cracks in overlying structures and can even cause them to tilt or collapse [2, 3]. Liquefaction research began in earnest following the earthquakes of Alaska (M_w 9.2) and Niigata (M_s 7.5) in 1964, where liquefaction-induced damage like slope failures, bridge failures and floatation of buried structures took place on a large scale [4-6]. Consequently, extensive liquefaction studies [e.g., 5-7] have been undertaken across the world to understand its causes, to better understand the mechanisms that govern liquefaction, and also to quantify its effects on the basis of various parameters.

Many researchers have reported the occurrence of liquefaction during recent earthquakes. Soga [8] reported severe liquefaction of loose fill materials, accompanied by ground settlements of 20–50 cm and lateral spreading of the range 1-2 m in the port and harbor regions of Kobe following the 1995 Kobe earthquake. During the 2001 Bhuj earthquake in north-western India,

Rajendran et al. [9] observed widespread liquefaction, giving rise to craters, lateral spreading that caused damages to underground pipes and systems. Wakamatsu et al. [2] investigated the liquefaction induced catastrophe (tilting of structures, ground settlement as high as 50 cm) caused by the Chuetsu earthquake (2004) all across the alluvial plains of the Shinano River. During the 2010-2011 Christchurch earthquakes, Cubrinovski et al. [10] reported severe manifestation of liquefaction in the suburbs of Christchurch and its central business district. Figure 1-1 illustrates some of the liquefaction induced damages observed during the 1964 Niigata earthquake and the 2011 Christchurch earthquake. Liquefaction-induced damages had also been reported during the 2010 Haiti earthquake [11], 2018 Indonesia earthquake [12], the 2019 Greece earthquake [13], and the 2020 Croatia earthquake [14].

1.2 LIQUEFACTION TRIGGERING CRITERIA

Liquefaction commonly occurs in saturated, loose, sandy soil deposits. Non-plastic and cohesionless coarse silts that have a bulky particle shape are also susceptible to liquefaction [15]. Liquefaction has also been observed for gravels [16], especially, when excess pore pressure dissipation is impeded due to the presence of thin impermeable layers that result in undrained conditions. The liquefaction susceptibility of a soil decreases with an increase in relative density (D_r), fines content, and plasticity of fines and it increases with an increase in confining pressure. Cohesive soils are still susceptible to strength loss due to cyclic loading [17-19], but this is not the focus of this dissertation.

Several definitions have been used in the past to quantify liquefaction triggering. The onset of liquefaction is commonly defined through the magnitude of excess pore pressure ratio, r_u, which is the ratio of excess pore pressure to the initial vertical effective stress. A r_u of 1, corresponding

to a zero effective stress condition, is often defined as the criterion that governs the onset of liquefaction [20]. However, Ishihara [15] suggested that liquefaction can occur at r_u values less than 1, such as in silty sands or sandy silts where r_u values often level out at 0.9-0.95. Moreover, a r_u value of 1 is not achieved in various other situations such as in dense clean sands and/or for sloping ground conditions [21].

Figure 1-1: (a) Liquefaction-induced foundation failure of Kawagishi-cho apartment buildings during the 1964 Niigata earthquake (Source: Kramer [22]) and (b) consequences of liquefaction following the 2011 Christchurch earthquake in New Zealand (Source: www.geotech.hr).

The strain-based criterion to define liquefaction triggering has gained more popularity in recent liquefaction studies [e.g., 15, 21, 23]. The cyclic strain-based laboratory tests performed by Ladd et al. [23] resulted in the conclusion that excess pore pressures do not build-up below a threshold cyclic shear strain of 0.01%. This threshold value was also reported to be independent of D_r and confining pressure but dependent on the overconsolidation ratio (OCR). The strain level corresponding to the occurrence of zero effective stress (r_u = 1), has been investigated based on laboratory tests like cyclic triaxial (CTX) test or cyclic direct simple shear (DSS) test. Seed and Lee [20] considered a double amplitude (DA) shear strain of 20% as the liquefaction triggering criterion based on CTX tests. Subsequently, liquefaction triggering criteria of 5% DA shear strain based on CTX tests and 6% DA shear strain based on DSS tests were suggested by Ishihara [15] and Wu et al. [21], respectively. Figure 1-2 shows some of the stress-strain and pore pressure responses due to loading in a cyclic DSS test.

Liquefaction triggering criteria have also been defined using semi-empirical correlations [e.g., 24-26]. These criteria use data from in-situ field tests like standard penetration tests (SPTs) and cone penetration tests (CPTs) to develop charts that can be used to predict liquefaction occurrence based on soil penetration resistances and earthquake magnitudes. These correlations consider data from sites where earthquake events have occurred in the past and liquefaction may/may not have been reported.

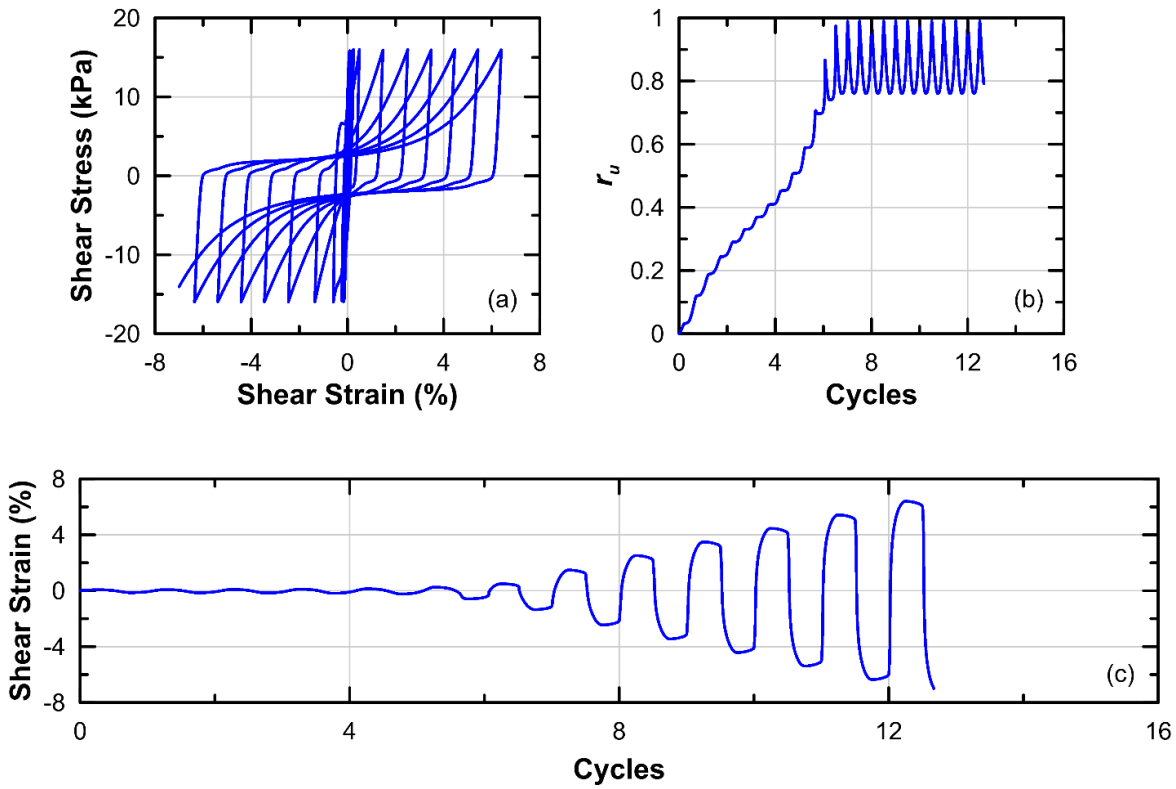

Figure 1-2: Typical stress-strain and pore pressure responses observed during a cyclic direct simple shear loading [27]: (a) shear stress versus shear strain response, variation of (b) r_u and (c) shear strain with number of loading cycles.

1.3 ASSESSMENT OF LIQUEFACTION-INDUCED SETTLEMENTS

Several empirical models have been developed that use laboratory experiments and field observations to estimate liquefaction-induced settlements in the free-field [e.g., 28-34]. These models often rely on SPTs or CPTs and use estimates of earthquake intensity to predict volumetric strain (and, therefore settlements) within a soil profile. However, most of these simplified empirical models exhibit distinct limitations. For example, settlements predicted using procedures proposed by Ishihara and Yoshimine [29] or Zhang et al. [31] are often conservative for saturated soil layers in deposits that do not reach initial liquefaction [35]. Moreover, these empirical models cannot take into account the effects of partial saturation or partial drainage [36], thin layers and

lenses [37], non-liquefiable crusts [38, 39] or soil fabric and aging [40, 41]. These models also cannot take into account the effects of soil-structure or soil-foundation interactions and they do not have the ability to incorporate spatially variable soil properties. Figure 1-3 illustrates the popular empirical framework by Ishihara and Yoshimine [29] that estimates the post-liquefaction volumetric strain based upon the maximum shear strain developed during shaking.

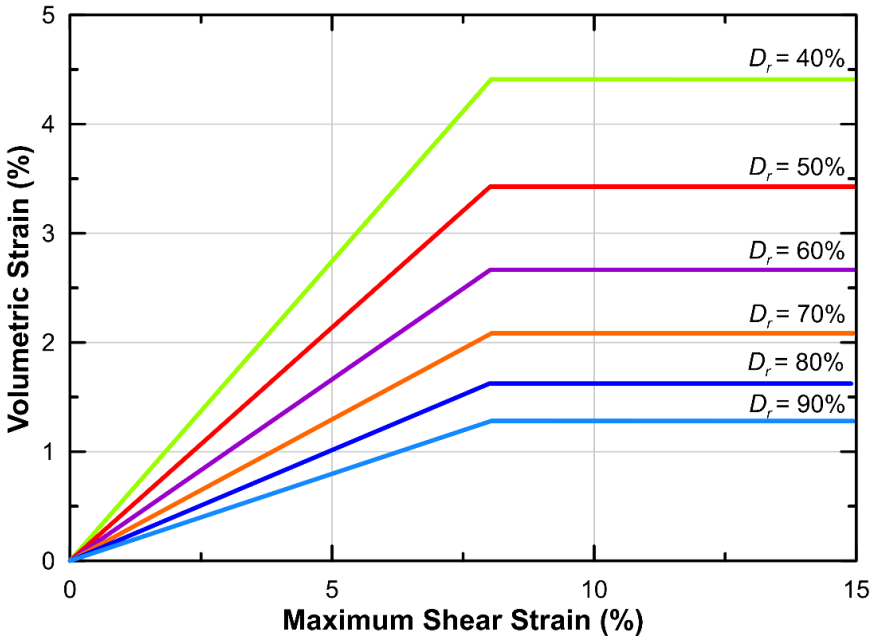

Figure 1-3: Ishihara and Yoshimine [29] correlation between volumetric stain and maximum shear strain at various relative densities.

Experiments like centrifuge tests [e.g., 42, 43] and shake table tests [e.g., 44] are often used to physically model liquefaction in a geosystem. These experiments can incorporate some of the complexities encountered in the field such as sloping ground conditions, soil heterogeneity, soil-structure interaction to list a few. Fully transient earthquake motions can also be applied through a mechanical shaker that is commonly connected to the apparatus. Centrifuge experiments are conducted under an acceleration field that is several times larger than the acceleration due to

gravity (g). This enables the use of a small-scale model to represent a full-scale prototype geotechnical system whose dimensions are scaled down as per relevant centrifuge scaling laws [45]. Shake table tests, on the other hand, are conducted at 1g acceleration field. The prototype geometry is often modeled at a smaller scale in shake table tests, whereby, the model parameters are scaled using relevant scaling laws, such as those proposed by Iai et al. [46]. Figure 1-4 shows a typical centrifuge and a shake table apparatus.

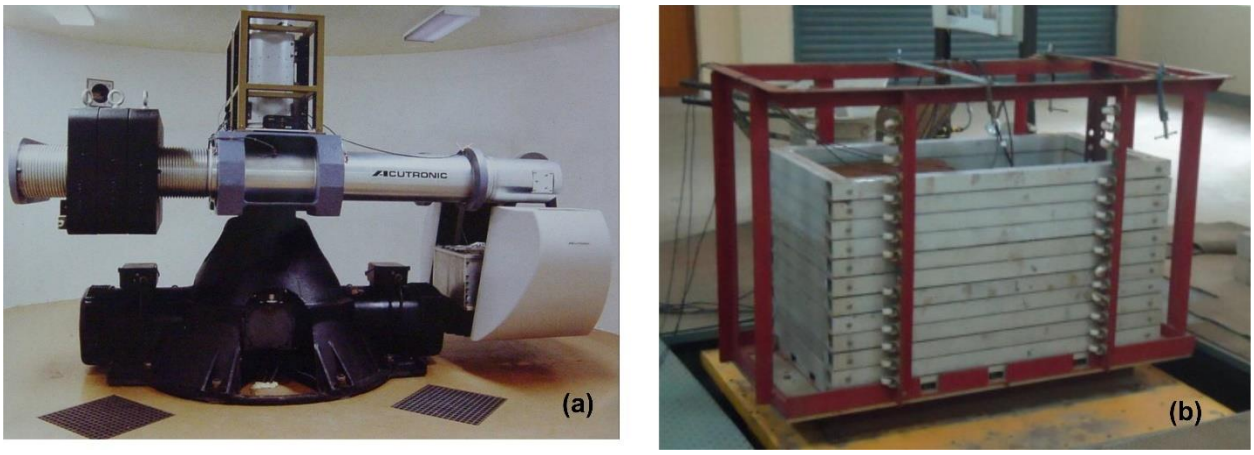

Figure 1-4: (a) Centrifuge apparatus at Rensselaer Polytechnic Institute (Source: Ha et al. [47]) and (b) a shake table apparatus (Source: Srilatha et al. [48]).

Numerical models have some advantages over empirical models as they can more directly examine the effects of topography, heterogeneous soil conditions, and structural and foundation interactions on liquefaction-induced deformations [49-53]. Numerical models have their advantages over laboratory experiments as they are quicker and often cheaper to perform. However, proper validation of numerical models to laboratory experiments [e.g., 50, 54] and field case histories [e.g., 55, 56] is essential to be able to use them for liquefaction assessment.

The effectiveness of a numerical framework in modeling soil liquefaction depends on the efficacy of the stress-strain constitutive relationship being employed to model the soil. Multiple

constitutive models are available that can be calibrated to simulate the triggering of liquefaction and deformations during cyclic loading, such as UBCSAND [57], PM4Sand [58], WANG2D [59], PDMY02 [60], and modified Manzari and Dafalias [61]. However, many constitutive models underpredict the volumetric strains (and therefore settlements) associated with reconsolidation of liquefied soils by an order of magnitude due to their inability to model sedimentation and ejecta [54, 62, 63]. Ziotopoulou and Boulanger [62] proposed a phenomenological approach to capture volumetric strains during reconsolidation by reducing the elastic modulus of the soil following seismic loading to increase volumetric strains. The magnitude of this reduction was calibrated based on the empirical relationships developed by Ishihara and Yoshimine [29] to predict the post-liquefaction settlement and incorporated into the PM4Sand constitutive model [58]. It is unclear if this single calibration is applicable to all soils and loading conditions or not. This approach has been used to successfully evaluate reconsolidation settlements for several case histories [e.g., 62, 64], but uncertainty in both the numerical modeling and field observations makes it difficult to draw conclusions regarding model validation or calibration from these comparisons. Moreover, multi-directional seismic loading that takes place in field is not replicated in 2D numerical models. This might result in considerable underprediction of reconsolidation settlement [65]. Carefully controlled physical models, such as centrifuge and shaking table tests, can be used to both validate procedures for adjusting post-shaking compressibility in constitutive models and to examine whether a single calibration is sufficient for all soils.

1.4 SPATIAL VARIABILITY

Most of the state-of-practice liquefaction assessment protocols, including both empirical frameworks and laboratory experiments, consider liquefiable soil deposits with uniform properties. However, in most cases a soil deposit in the field will be heterogeneous with the properties varying

spatially in both vertical and lateral directions. This spatial variability in soils generally arises from the (1) spatial variability in thickness of a given soil layer [66], (2) variability in lateral extent of a given soil layer [67], (3) the inherent variability within the given layer [68, 69], and/or (4) as a result of combination of all of these sources. While the variability arising from Sources 1 and 2 can be reasonably estimated through a sufficient number of soil explorations, the inherent variability (Source 3) in a soil stratum can never be fully quantified through any cost-effective number of explorations. Many in-situ field tests and analytical studies have been performed to explore inherent spatial variability and quantify it for geosystems [e.g., 68, 70-72]. Spatial variability in a soil deposit can lead to differential settlement over a loaded area and structural damage [3].

The inherent soil variability may be modeled using random field theory (RFT; [73]). For example, a spatially varying soil property of interest, $g(z)$ may be separated into a deterministic trend function $t(z)$ and a randomly fluctuating component $w(z)$ [68, 70] as shown in Equation 1:

$$g(z) = t(z) + w(z) + \varepsilon(z) \quad (1)$$

where z is the depth and $\varepsilon(z)$ is the measurement error. The spatially varying soil property is characterized by its mean (i.e., through the trend function), the variance or coefficient of variation (COV) of the fluctuating component, and the autocorrelation length or the scale of fluctuation, which is the distance within which soils demonstrate a reasonably strong correlation [74]. The horizontal scale of fluctuation (δ_h) is larger than the vertical scale of fluctuation (δ_v) for most modes of geologic deposition. Hence, characterization of δ_h for foundation soils generally provides more information regarding expected differential settlements. The coefficient of inherent variability,

COV_w, defined as the ratio of the standard deviation of the fluctuating component to the trend function, is also commonly used in geotechnical engineering [68].

Therefore, it is important to incorporate this variability in liquefaction assessment studies in order to produce reasonable prediction of responses for a field phenomenon like liquefaction. Empirical models, owing to their one-dimensional (1D) formulation necessarily treat the soil as laterally homogeneous. It is also extremely difficult to model the in-situ field variability in laboratory experiments. Numerical models, on the other hand, can incorporate this variability using data from soil exploration tests. Penetration resistance data from SPT or CPT tests are used in the random field modeling framework to produce soil models with geospatial properties [e.g., 69, 75]. These geospatial properties may be used in numerical models to conduct liquefaction assessment and predict post-liquefaction responses such as excess pore pressures, lateral spreading, and reconsolidation settlement. The effects of spatial variability in soil properties have been taken into account by using numerical models [e.g., 76, 77], but these models are not commonly used in practice.

1.5 PM4SAND: BRIEF INTRODUCTION

This study utilizes PM4Sand Version 3.1 (formulation and implementation described in Boulanger and Ziotopoulou [58], compiled for FLAC 8.0 in 2017) for the numerical simulations. PM4Sand is a nonlinear constitutive model which was specifically developed to model the behavior of sands and non-plastic silts in earthquake engineering problems. It is a stress-ratio controlled, critical-state compatible, bounding-surface plasticity model, based on the plasticity model initially developed by Dafalias and Manzari [78] and described in detail by Boulanger and Ziotopoulou [58]. It is cast in terms of relative state ξ_r (i.e. the difference between the relative density D_r and

the relative density at critical state $D_{r,cs}$ for the current confining pressure), such that the soil properties can change during the simulation as a function of the change in state (i.e., changes in mean effective stress and/or void ratio). A schematic of some of the essential features of the model are outlined in Figure 1-5.

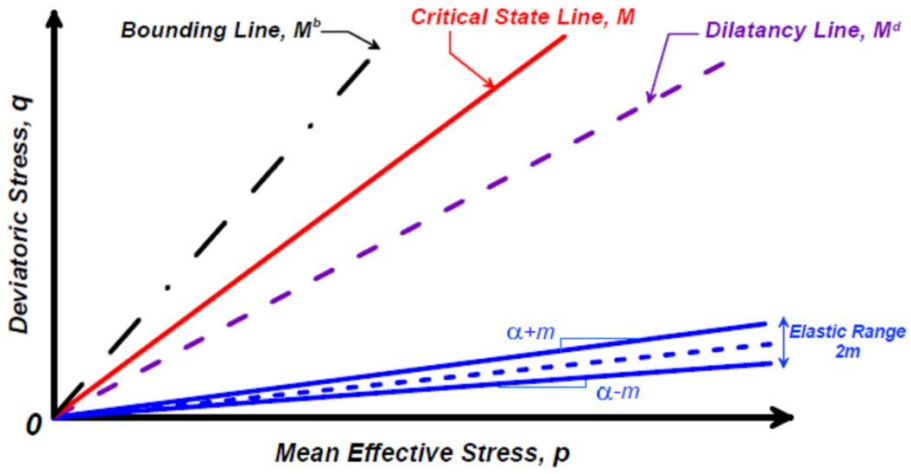

Figure 1-5: Schematic of the rotated dilatancy line added to PM4Sand along with the yield, critical, dilatancy and bounding lines in q-p space (Source: Boulanger and Ziotopoulou [58]). Relative location of dilatancy and bounding lines corresponds to dense-of-critical states of stress.

The model has three primary input parameters, 21 secondary parameters, and two flags. The primary PM4Sand model parameters are D_r, the contraction rate parameter h_{po}, and shear modulus coefficient (G_o). Table 1-1 highlights some of the parameters that are commonly calibrated to match the response a specific soil. The model was developed such that it can be used with only the three primary parameters, while all secondary parameters have been calibrated by the developers to reasonably approximate the range of behaviors exhibited by the broader body of data on clean sands. The secondary parameters can be modified to better capture observed behaviors when laboratory test or any other data are available. The parameters controlling the

reconsolidation response (volumetric strain and, therefore, reconsolidation settlement) in PM4Sand are $f_{sed,min}$ and $p_{sed,o}$. These adjust the post-shaking modulus in a liquefied soil to account for the effects of sedimentation [62, 63]. The values of $f_{sed,min}$ and $p_{sed,o}$ are calibrated to the Ishihara and Yoshimine [29] framework as described in the PM4Sand manual [58].

Table 1-1: PM4Sand parameters that are commonly calibrated to specific soils.

Parameter	Comments
D_r	**Apparent relative density:** Primary variable controlling dilatancy and stress-strain response characteristics
G_o	**Shear modulus coefficient:** Primary variable controlling the small strain shear modulus, G_{max}.
h_{po}	**Contraction rate parameter:** Primary variable that adjusts contraction rates and hence can be adjusted to obtain a target cyclic resistance ratio. Commonly calibrated to approximate the strength degradation during strain-controlled loading.
e_{max}	**Maximum void ratio:** Default value is 0.8.
e_{min}	**Minimum void ratio:** Default value is 0.5.
n_b	**Dial controlling bounding ratio** $M_b = Mexp(-n_b \xi_r)$: Default value is 0.50 (chosen in order to honor Bolton's Dilatancy relationship). Controls dilatancy via and thus also the peak effective friction angles. If modified, it controls post-triggering strain accumulation for undrained loading.
Φ'_{cv}	**Critical state friction angle:** Default value is 33.

1.6 FLAC: BRIEF INTRODUCTION

FLAC 8.0 [79] is a two-dimensional (2D) explicit finite difference program for engineering mechanics computations. The program simulates the behavior of structures built of soil, rock or other materials that may undergo plastic flow when their yield limits are reached. Materials are represented by zones, or elements, which form a grid that is adjusted by the user to fit the shape of the structure to be modeled. Internally, FLAC divides each user-defined quadrilateral zone into

two sets of overlaid constant-strain triangles. Each element behaves according to a prescribed linear or nonlinear stress/strain law in response to the applied forces or boundary restraints. At each node of the zones the force vector is the mean force exerted by the overlaid triangles. The explicit, Lagrangian calculation scheme and the mixed-discretization zoning technique used in FLAC ensure that plastic collapse and flow are modeled accurately. The explicit formulation of the program requires a small dynamic time-step be used to ensure an accurate solution. FLAC can simulate coupled hydro-mechanical response which is critical for liquefaction modeling.

FLAC solves the full dynamic equations of motion for each zone and follows an explicit integration scheme: the equations of motion are first invoked to derive new velocities and displacements from stresses and forces. Then, strain rates are derived from velocities, and new stresses from strain rates. It takes one time step for every cycle around the loop. That time step is small enough (often an order of 10^{-5} s) that information cannot physically pass from one element to another in that interval and this way the computational information is always ahead from the physical information. No iteration process is necessary when computing stresses from strains in an element, even if the constitutive law is wildly nonlinear (as is the case with PM4Sand). A disadvantage of the explicit method is the small time-step, which means that large numbers of steps must be taken, and thus long computational time is required for an analysis. Figure 1-6 illustrates lateral displacement contours obtained from a typical numerical model in FLAC.

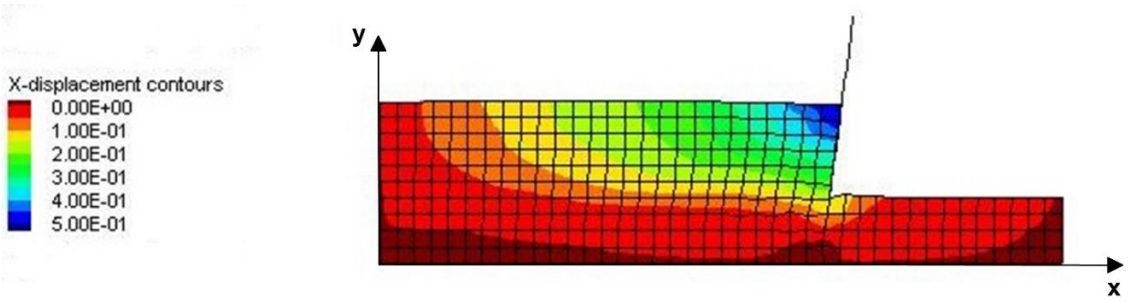

Figure 1-6: FLAC model to monitor horizontal displacements in a sand deposit retained by a sheet-pile wall structure.

1.7 REASONSING BEHIND CHOICE OF FLAC AND PM4SAND

FLAC being an explicit finite difference numerical code has its own advantages over finite element codes which often use an implicit scheme. The explicit nature of FLAC allows for a non-iterative calculation scheme at each element in the model at every timestep. This means that the responses at an element do not depend on the responses of the surrounding elements at every step. This might seem contradictory to the actual mechanisms that are in action in a physical system, but the timestep selected is small enough that no information can get physically transmitted across the elements within that small amount of time. This means that the computational wave speed is faster than the physical wave speed, and over several timesteps the disturbances in an element would propagate to the surrounding elements as would be expected physically. The element-level stiffness matrices need not be converted to a global stiffness matrix at each timestep in FLAC unlike in finite element programs. This makes FLAC computationally faster at each timestep and requires less memory. Moreover, since global stiffness matrices are not required in FLAC, it is a trivial task to update the coordinates of the numerical grid at each timestep. This allows the usage of the Lagrangian scheme in FLAC where the grid moves and deforms with the material it

represents. FLAC also requires lesser computational effort in solving nonlinear, large strain problems than finite element programs.

PM4Sand presents its advantages over many other constitutive models on sand owing to its kinematic hardening formulation along with bounding surface which capture the plastic response of cyclically loaded liquefiable sand well. It is also a stress-ratio controlled model which means that the deviator stress is normalized with respect to mean effective stress, thus making it convenient to compare the current stress state with the yield and failure surfaces. Volumetric strains that develop during post-shaking reconsolidation of sand are difficult to model using the traditional constitutive approach of separating them into elastic and plastic components since a large portion of these reconsolidation strains are due to sedimentation effects which are not easy to incorporate in either the elastic or plastic strain components [62, 63]. Most of the traditional constitutive models underpredict the reconsolidation strains observed in experiments by an order of magnitude due to their inability to capture sedimentation strains. In PM4Sand a pragmatic approach of post-shaking moduli reduction is used, thereby compensating for the sedimentation strains that are not explicitly modeled. This approach enables a much more reasonable prediction of volumetric strains as compared to many other constitutive frameworks.

The numerical simulations described in this study were performed using a high-performance workstation with two Intel® Xeon® Gold 6136 CPUs with twelve 3.00 GHz cores. The RAM capacity of this computer was 128 GB. The usual runtime for each simulation varied between 4 to 8 hours depending upon the size of FLAC mesh and permeability of the zones.

1.8 2D VERSUS 3D NUMERICAL MODELING APPROACH: ADVANTAGES AND LIMITATIONS

In this study, the geosystems are modeled using a 2D approximation of soil profiles from experiments or from the field. This approach is reasonable in case of plane-strain conditions [63] where there is no significant asymmetry in model geometry or boundary conditions in the cross-lateral (perpendicular out-of-plane) direction. Therefore, 2D numerical modeling is appropriate in case of soil deposits with consideration of uniformly distributed properties such as those described in Chapters 2 and 3 in this dissertation. Under these circumstances, a 2D numerical model is computationally more efficient than a 3D model, while not sacrificing significant accuracy. However, for a soil deposit with properties varying spatially in both in- and out -of-plane directions, a 3D model would be more suited in capturing the full response even though pseudo 3D analysis using multiple 2D sections have been used for such scenarios in previous studies [80, 81]. This is a limitation of the work presented in Chapter 4 where multiple 2D soil sections in the out-of-plane direction are used to represent a 3D spatially variable soil geometry. The interaction effects between the sections are not captured in this pseudo 3D analysis and this remains an area for future research.

1.9 MOTIVATION AND GOALS

Soil liquefaction poses a major threat to human life and property, as had been discussed in the previous sections of this chapter. Reconsolidation settlements observed during liquefaction have been a major source of damage in past earthquakes. Hence, it is necessary to design methodologies to be able to predict this settlement for various types of soil and site conditions. Numerical models are an efficient tool that can achieve the above-mentioned targets. Assessment of the parameters that have the most severe effects on the liquefaction prediction capabilities of a numerical model

is an important step in expanding the use of these models. Many previous studies have evaluated the efficacy of constitutive models in predicting liquefaction responses by comparison to responses observed in physical models like centrifuge or shake table tests [e.g., 44, 50, 54, 82, 83]. However, most of these numerical methodologies were focused on simulating the responses for one particular soil type and might fall short if used for a different soil. The primary motivation for this study is to improve the existing numerical protocols for liquefaction modeling in order to accurately predict observed liquefaction responses for a range of soil types. The goal is to establish a standard numerical approach and constitutive model calibration procedure that can be employed to predict reconsolidation responses (with primary focus on settlements) successfully for a variety of soils, input motions and boundary conditions. Moreover, most of the existing numerical frameworks are limited to evaluating the liquefaction-induced responses of soil deposits whose properties are assumed to be uniformly distributed to simplify calculations. However, a uniform soil layer is often an over-simplification of the field reality. Hence, the predictions from a numerical model with the consideration of a uniform deposit may not reflect the real field behavior. Therefore, a more in-depth assessment of the effects of spatially variable soil properties on reconsolidation settlements is required. In this study, spatial variability is incorporated in the numerical modeling framework to investigate its effects for actual site conditions.

1.10 RESEARCH OBECTIVES

The main objectives of this research are outlined below:

- To evaluate the ability of the numerical platform FLAC and constitutive model PM4Sand to capture the liquefaction-induced responses observed in free-field uniform soil deposits,

geosystems involving soil-structure interaction effects, and soil deposits with spatially variable properties.

- To examine the necessity of soil-specific calibration of reconsolidation parameters for a constitutive model to ensure reasonable prediction of reconsolidation settlements.
- To investigate the effect of potential changes in hydraulic conductivity (k) due to liquefaction on excess pore pressure, lateral displacement and settlement responses of geosystems.
- To explore the influence of inherent spatial variability in soil properties on the post-liquefaction response of a level-ground site.

1.11 DISSERTATION ORGANIZATION

This dissertation is divided into 5 chapters as follows:

- *Chapter 1 – Introduction*: This chapter presents a general background on liquefaction-induced reconsolidation settlement, and numerical modeling approach to capture liquefaction responses. Additionally, it highlights the motivation and objectives for this study and outlines the dissertation structure.
- *Chapter 2 – Observations and challenges in simulating post-liquefaction reconsolidation settlements from centrifuge and shake table tests*: This chapter utilizes centrifuge and shaking table tests to examine the ability of the PM4Sand model to capture the observed reconsolidation settlements including the need for soil-specific calibration of reconsolidation parameters. The effect of hydraulic conductivity variation due to liquefaction is also investigated and a variable hydraulic conductivity relationship is incorporated into the numerical model.

- *Chapter 3 – Investigation of the key issues in simulating centrifuge experiments on a sheet-pile wall embedded in a liquefiable sand*: This chapter presents the results from a numerical study performed as part of the Liquefaction Experiments and Analysis Project (LEAP) 2020 exercise that aims at simulating centrifuge tests modeling a soil-retaining wall system. The key soil and model parameters that affect the prediction of liquefaction responses are studied.
- *Chapter 4 – Numerical modeling of reconsolidation settlements for a spatially variable soil deposit*: This chapter focuses on estimation of reconsolidation settlements for a soil site at Hollywood in South Carolina incorporating spatially variable soil properties. The physical mechanisms associated with liquefaction in such a deposit are evaluated.
- *Chapter 5 – Summary, conclusions, and future research*: This chapter summarizes the findings from this research and discusses their applicability in practice. Future research opportunities in this area are also discussed.

CHAPTER 2: OBSERVATIONS AND CHALLENGES IN SIMULATING POST-LIQUEFACTION RECONSOLIDATION SETTLEMENTS FROM CENTRIFUGE AND SHAKE TABLE TESTS

This chapter is based on a paper submitted by Devdeep Basu, Jack Montgomery and Armin Stuedlein to the journal *Soil Dynamics and Earthquake Engineering.*

Basu, D., J. Montgomery, and A. Stuedlein. 2021. "Observations and challenges in simulating post-liquefaction reconsolidation settlements from centrifuge and shake table tests." Soil Dynamics and Earthquake Engineering (Elsevier). Paper Under Review.

This chapter was altered from the version that was submitted to *Soil Dynamics and Earthquake Engineering* for the purpose of avoiding redundancy and maintaining better flow in this dissertation. My primary contributions to the paper included: (i) evaluating the importance of soil parameters like hydraulic conductivity and soil-specific constitutive model calibration to accurately simulate laboratory tests, (ii) gathering and reviewing literature, (iii) development and design of numerical approach, (iv) processing, analyzing, and interpretation of the results, (v) most of the writing.

2.1 ABSTRACT

Liquefaction-induced reconsolidation settlements occur as excess pore pressures generated during shaking dissipate and can lead to significant damage to overlying infrastructure. Designing resilient infrastructure in areas affected by liquefaction requires methods to predict these settlements for different soil types and boundary conditions. Simplified empirical models are commonly utilized to evaluate settlements but they exhibit several limitations that might hinder the accuracy of settlement predictions, including effects of partial drainage, thin layers, non-

liquefiable crusts, or soil fabric. Numerical models can capture these effects but require proper calibration and validation. This study uses a numerical approach to simulate centrifuge and shake table experiments with free-field level, ground conditions and five different sands for evaluating reconsolidation settlements. The numerical platform FLAC and constitutive relationship PM4Sand are utilized. The necessity of soil-specific calibration of post-liquefaction stiffness and an excess pore pressure ratio dependent hydraulic conductivity to accurately model the observed pore pressures and settlements is analyzed. A new relationship between the increase in hydraulic conductivity due to liquefaction and grain size diameter is proposed. The numerical simulations are able to capture the general trends, but the bias in the results appears to be correlated with the grain size of the tested soil.

2.2 INTRODUCTION

This chapter leverages centrifuge and shaking table tests to examine the ability of the PM4Sand model to capture the observed reconsolidation settlements including the need for soil-specific calibration. Numerical simulations are developed and calibrated using available lab data and the recorded experimental responses during the dynamic phase of the tests. All of the tests represent free-field and level ground conditions in order to isolate the effects of reconsolidation of the liquefiable soils from other aspects, such as spatial variability or soil-structure-interaction, which will be examined in future studies. The objectives of the study are to examine the effects of the model calibrations and potential changes in hydraulic conductivity due to liquefaction on the settlements of different soils subjected to various shaking intensities. The results show that the numerical simulations capture the overall patterns of settlement and dissipation, but the dissipation rates observed in the centrifuge tests are not captured well numerically. Using a variable-hydraulic conductivity model [1] improves the agreement of the simulations and experiments and the

magnitude of the increase in hydraulic conductivity due to liquefaction correlates to the effective grain diameter of the sand. The use of soil-specific calibration for post-liquefaction stiffness considerably improves agreement for the experiment where such data is available.

2.3 CENTRIFUGE AND SHAKE TABLE EXPERIMENTS

Three centrifuge tests [2-4] and two shake table tests [5, 6] focusing on free-field settlement of liquefiable deposits with level ground conditions were examined in this study. The above-mentioned experiments were selected because they had sufficient data to characterize both the generation and dissipation of excess pore pressures and the original authors did not report any issues with settlement measurements that may have impacted the validity of the comparisons. Table 2-1 highlights the geometry of the test specimens in prototype units and the centrifugal acceleration used for each experiment. The ground water table was located at the top of soil surface in all of the tests, and all of the experiments were performed using laminar box containers. Some of the input motion characteristics are also included for each test. Table 2-2 outlines selected properties of the uniformly-graded, fine-to-medium coarse sands used in the study. The grain shapes of the sands are included in Table 2-2 when available. The centrifuge experiments were performed on either single-layered (two experiments) or multi-layered (one experiment), saturated, homogeneous soil deposits replicating level ground conditions in prototype. The sands were placed using air pluviation techniques and saturated with a viscous fluid scaled to match the viscosity of water during spin in the centrifuge tests.

Table 2-1: Parameters for the setup of the centrifuge experiments and shake table tests considered in the present study. The dimensions are presented in prototype units.

No.	Authors	Centrifugal Acc. (g)	Width (m)	Height (m)	Input Motion Type	Peak Acc. (g)	Duration (s)	Arias Intensity (m/s)
1	Adamidis and Madabhushi [2]	50	25	12	Synthetic; pseudo-harmonic	0.29	20	5.01
2	Ramirez et al. [3]	70	67.7	18	Recorded; 1995 Kobe earthquake[2]	0.41	50	1.99
3	Mehrzad et al. [4]	80	56.8	24	Synthetic; pseudo-harmonic	0.18	10	1.69
4	Ecemis [5][3]	1	14.4	14.4	Synthetic; pseudo-harmonic	0.09	38	2.06
5	Thevanayagam et al. [6][4]	1	5	5	Synthetic; staged-harmonic[5]	0.01; 0.05; 0.15; 0.3	35	8.86

1. The centrifuge model was a multi-layered deposit with a 6 m thick loose liquefiable Ottawa F-65 sand layer (D_r = 40%), overlain by a 2 m thick dense Monterey 0/30 sand layer (D_r = 90%) and underlain by a 10 m thick dense Ottawa F-65 sand layer (D_r = 90%).
2. The earthquake motion was recorded at Takatori station in Kobe, Japan.
3. The model units for the shake table test by Ecemis [5] were scaled according to relevant scaling laws by Iai et al. [7], as recommended by the original authors.
4. The shake table test by Thevanayagam et al. [6] was simulated without scaling.
5. A wave packet consisting of four harmonic motions were applied successively.

Table 2-2: Geotechnical properties of the sands used in the numerical models for this study.

No.	Sand	D_r (%)	G_s	e_{max}	e_{min}	Φ_{crit}	k (mm/s)	Grain shape	D_{50} (mm)	D_{10} (mm)	C_u	C_c
1	Hostun	40	2.65	1.01	0.555	33°	0.5	Angular to subangular	0.335	0.209	2.01	1.03
2	Monterey 0/30	90	2.66	0.84	0.54	33°	0.53	Subangular to subrounded	0.4	0.28	1.3	1.11
	Ottawa F-65	40	2.65	081	0.53	30°	0.141	Subrounded	0.21	0.16	1.71	0.86
	Ottawa F-65	90	2.65	0.81	0.53	30°	0.119	Subrounded	0.21	0.16	1.71	0.86
3	No. 306	55	2.65	0.92	0.59	33°	0.747	-	0.193	0.147	1.21	0.99
4	M-1[1]	28	2.61	0.79	0.6	33°	0.23	Subangular	0.21	0.12	1.17	1.29
5	Ottawa F-55	40	2.67	0.8	0.61	33°	0.12	Subrounded	0.24	0.155	1.57	1.04

1. This is a mixed sand that was prepared by mixing a few different natural sands [5].

2.4 NUMERICAL MODELING

The laboratory experiments were modeled using the 2D finite difference program FLAC version 8.0 [8]. FLAC uses an explicit finite difference formulation to solve the equations of motions and is capable of modeling complex behaviors like multistage problems, large strains, and nonlinear material behavior. The problem domain is discretized into quadrilateral zones or elements that form a mesh. Prescribed constitutive laws are used at the element level which govern the response of elements to applied forces and boundary constraints. For the current study, PM4Sand [9] was used as the constitutive model for all stages.

All of the tests in this study examined the free-field response of laterally homogenous sand deposits in laminar containers to approximate a one-dimensional (1D) response. These experiments were therefore simulated using a 1D column of elements in FLAC (baseline simulations) for computational efficiency. The baseline simulation for each test used a 0.5 m square mesh. Figure 2-1 shows the numerical mesh for a typical model. Sensitivity studies were performed using a 2D mesh (also shown in Figure 2-1) to verify the 1D simulations were representative.

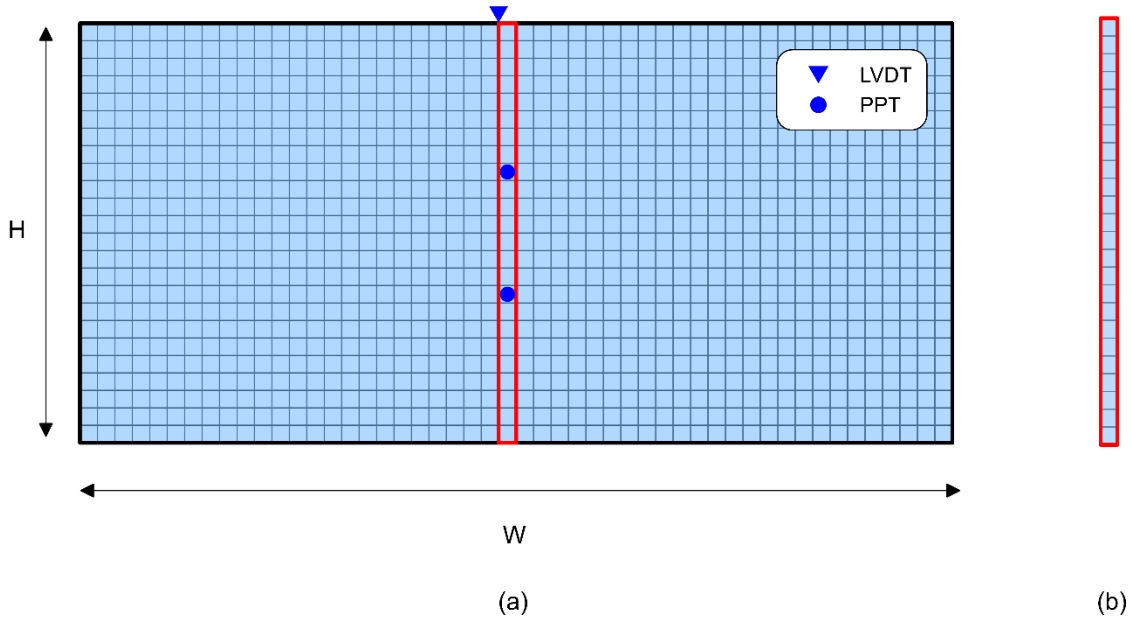

Figure 2-1: Typical FLAC meshes for (a) full-scale 2D model and (b) 1D column from the center of the 2D model highlighting pore pressure transducers (PPTs) and settlement sensors (LVDTs). Note: W and H correspond to the width and height, respectively, from the experiments as stated in Table 2-1.

Each simulation was performed in three phases: (1) static equilibrium, (2) dynamic shaking, and (3) reconsolidation. During the first phase, the model geometry, boundary conditions, and soil properties were defined, and the geostatic stress state was obtained. Horizontal movement was restrained at the model sides and both horizontal and vertical movements were fixed at the base in the first and third phases. Hydrostatic pore pressure conditions were set up across the model to match the depth of initial ground water table reported in the experiments. The dynamic phase analysis was performed by applying the input motions as acceleration-time histories at the model base (as discussed in Section 2.4.4). Periodic boundary conditions were applied to the nodes along the sides of the model to match the displacement conditions enforced by the laminar boxes. Vertical and horizontal flow and corresponding redistribution of excess pore pressures within the model were allowed throughout the duration of simulations. Drainage could occur from the top of

the model, but the sides were considered no flow boundaries. Rayleigh damping of 0.5% centered at the predominant frequencies of the input motions was used to mitigate numerical noise. During the reconsolidation phase, the soil deposit was allowed to settle until all excess pore pressures developed during shaking had dissipated.

2.4.1 CONSTITUTIVE MODEL

The stress-ratio controlled, bounding surface plasticity constitutive model PM4Sand v3.1 [9] was used to capture the cyclic mobility and reconsolidation phases of liquefaction. Three primary parameters were used to calibrate the cyclic response of the model, the relative density (D_r), shear modulus coefficient (G_o), related to the maximum shear modulus, G_{max}, and contraction rate parameter (h_{po}). The reported D_r for each experiment was used, whereas G_o was defined based on shear wave velocity (V_s) measurements or G_{max} relationships developed for each of the sands, as shown in Equations 1 and 2.

$$G_{max} = \rho\, V_s^2 \tag{1}$$

$$G_o = \frac{G_{max}}{p_A}\left(\frac{p_A}{p'}\right)^{0.5} \tag{2}$$

where, ρ is the soil density, p_A is the atmospheric pressure and p' is the mean effective confining pressure. The contraction rate parameter controls the cyclic strength of the soil and must be calibrated to match liquefaction triggering data as determined through laboratory tests or empirical models or comparisons of the observed excess pore pressure generation during the experiments and described below.

Stress ratio-based constitutive models exhibit inherent limitations in capturing the reconsolidation strains following liquefaction as they are unable to capture sedimentation effects;

thus, the reconsolidation process is typically elastic and produces small volumetric strains [10, 11]. PM4Sand attempts to compensate for this limitation by reducing the elastic moduli during the reconsolidation process to increase the volumetric strains [11]. The reconsolidation process is activated by the user through a flag variable, *PostShake*, and the magnitude of the volumetric strains is controlled by two parameters, $f_{sed,min}$ and $p_{sed,o}$, which control the magnitude of modulus reduction and the range of mean effective stresses over which the reduction is active, respectively. Boulanger and Ziotopoulou [9] developed a D_r -dependent relationship for $f_{sed,min}$ (Equation 3) through calibration to the empirical relationship suggested by Ishihara and Yoshimine [12].

$$f_{sed,min} = 0.03 \exp(2.6 D_r) \quad (3)$$

Boulanger and Ziotopoulou [9] selected $p_{sed,o}$ = 20 kPa noting that volumetric strains were relatively insensitive to increases in $p_{sed,o}$ beyond 20 kPa (Figure 2-2). The effects of these parameters are shown in Figure 2-2 using data from single element, cyclic direct simple shear (DSS) simulations on a hypothetical sand at a D_r of 35% described in Boulanger and Ziotopoulou [9]. For any particular soil at a predetermined D_r, the volumetric strains increase with an decrease in $f_{sed,min}$ and increase in $p_{sed,o}$.

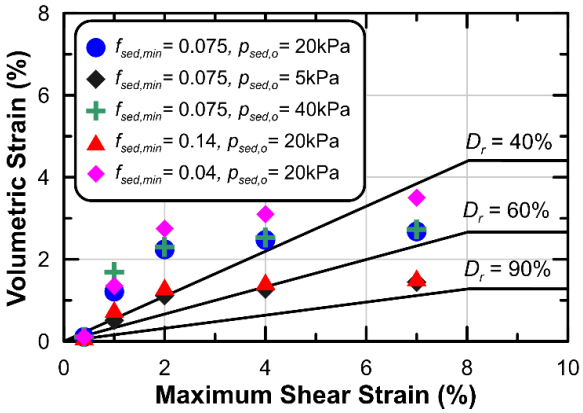

Figure 2-2: Volumetric strain versus maximum shear strain from single-element cyclic DSS simulations compared to Ishihara and Yoshimine [12] curves. Simulations are for a relative density of 35% with a G_o of 476 and an h_{po} of 0.53 after Boulanger and Ziotopoulou [9].

2.4.2 SOIL-SPECIFIC CALIBRATION

Soil-specific G_{max} or V_s data was available for Hostun sand [13, 14], Monterey 0/30 sand [3], Ottawa F-65 sand [15], No. 306 sand [16], and Ottawa F-55 sand [6]. The default relationship between G_o vs. D_r suggested by Boulanger and Ziotopoulou [9] was used for M-1 sand due to the lack of available information on small-strain stiffness. This relationship was developed by combining the Andrus and Stokoe [17] correlation between normalized shear wave velocity, V_{s1}, and corrected SPT blow count, $(N_1)_{60}$, and the Idriss and Boulanger [18] correlation between D_r and $(N_1)_{60}$.

Laboratory data on liquefaction triggering (Figure 2-3) was available for Hostun [19-21], Ottawa F-65 [15, 22-24], and Monterey 0/30 [25] sands and was used to calibrate h_{po}. This calibration was performed using single element cyclic DSS simulations to match the cyclic resistance ratio to reach 3% single amplitude shear strain in 15 cycles (CSR_{15cyc}). This number of cycles was selected since the input motions used for all the tests used 10 to 20 cycles of strong loading. The relative density of laboratory test specimens did not exactly match the D_r used in the experiments, so an interpolation was performed by fitting a cyclic strength curve with a functional form similar to Idriss and Boulanger [18], to the available data (Figure 2-3). As insufficient laboratory data was available to develop such triggering curves for No. 306, Ottawa F-55 and M-1 sands, the h_{po} values for these sands were selected to match the excess pore pressure build-up observed during the dynamic portion of the corresponding experiment. All secondary PM4Sand parameters were set to their default magnitudes with the exception of the parameter n_b for Ottawa F-65 sand. For Ottawa F-65 sand, n_b was slightly modified from its default value to match the rate of strain accumulation that occurred after triggering as discussed in Basu et al. [26]. Table 2-3 outlines the calibration parameters selected for each sand.

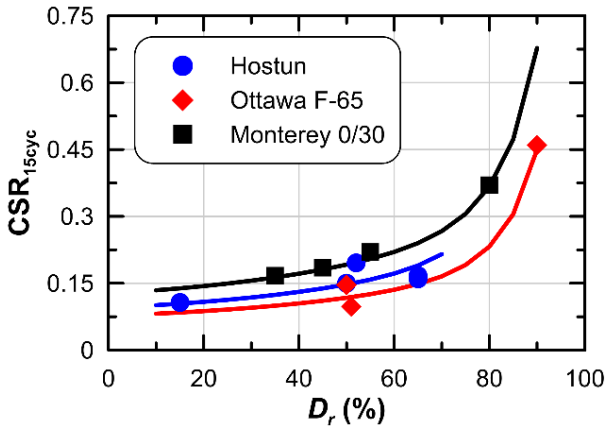

Figure 2-3: Liquefaction triggering curves developed from fitting experimental data on (a) Hostun (b) Ottawa F-65 and (c) Monterey sands that are used for h_{po} calibration. The cyclic stress ratio (CSR) corresponds to 15 cycles of sinusoidal loading in cyclic DSS test. Symbols correspond to experimental data and solid lines represent the simulation data fit.

Table 2-3: PM4Sand calibration parameters used for the sands in the numerical simulations.

No.	Sand	h_{po}	n_b	G_o
1	Hostun	1.5	0.5	670
2	Monterey 0/30	0.15	0.5	1324
	Ottawa F-65	0.35	0.6	195
	Ottawa F-65	0.31	0.6	725
3	No. 306	0.025	0.5	522
4	M-1	0.01	0.5	480
5	Ottawa F-55	0.12	0.5	192

The default values for the reconsolidation calibration parameters ($p_{sed,o}$ and $f_{sed,min}$) were selected by the model developers [9] to reasonably approximate the empirical relationships developed by Ishihara and Yoshimine [12]. As discussed earlier, calibration of these parameters against soil-specific data might improve post-shaking volumetric strain estimates in cases where such data are available. Vargas et al. [24] performed hollow cylinder cyclic torsional shear tests on Ottawa F-65 sand and found that the Ishihara and Yoshimine [12] relationships work well in predicting volumetric strains following liquefaction for D_r between 50% and 70%. Adamidis and

Madabhushi [27] performed oedometer tests on Hostun sand in order to measure the constrained modulus at low effective stresses (Figure 2-4). These stiffnesses are much larger than those produced by the default reconsolidation calibration used in PM4Sand (Figure 2-4). Adjusting $f_{sed,min}$ from the default value of 0.085 to 0.22 produces a much better fit to the experimental the data for effective stress less than 15 kPa (critical for reconsolidation). This type of soil-specific calibration for reconsolidation settlement is not commonly performed, but considerably improved the agreement of the simulation and observations as discussed later.

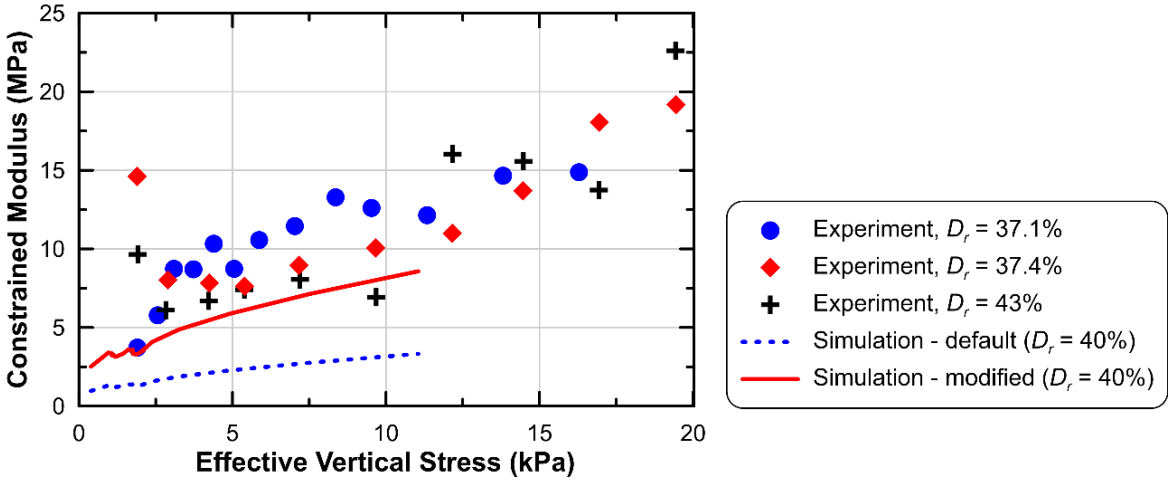

Figure 2-4: Soil-specific calibration of reconsolidation parameter $f_{sed,min}$ for Hostun sand using data from Adamidis and Madabhushi [27].

2.4.3 HYDRAULIC CONDUCTIVITY

Previous literature [e.g., 28-31] has suggested that liquefaction causes hydraulic conductivity, *k*, to increase due to loss of contact between soil grains in its liquefied state. As the liquefied soil reconsolidates, the contacts between grains are re-established and the hydraulic conductivity returns to some magnitude that may or may not reflect its initial fabric. Ueng et al. [32] and Bayoumi et al. [33] had observed a 5-fold and 1.5-fold increase in *k* during centrifuge tests on Vietnam and Ottawa C-109 sands, respectively. Su et al. [30] had observed an increase in *k* up to

six times larger in centrifuge tests on Toyoura sand, whereas Wang et al. [31] had observed a 4-fold increase in *k* during shake table tests on the same sand. Balakrishnan [34] and Shahir et al. [1] had observed a maximum increase in *k* of 20-fold corresponding to an excess pore pressure ratio, r_u (defined as the ratio of excess pore pressure to initial vertical effective stress) of 100% in centrifuge tests on Nevada sand. Gao et al. [35] had observed a maximum increase in *k* of 25-fold (at r_u = 100%) through numerical simulations of centrifuge tests on Fujian sand. Other numerical studies on Fraser River sand [36], Ottawa F-55 sand [37], Toyoura sand [38] had reported a maximum increase in *k* of 10, 25 and 4-folds, respectively. However, Adamidis and Madabhushi [27] noted a negligible increase in *k* during liquefaction of Hostun sand, on the order of 1.2 times the initial hydraulic conductivity, k_i, when effective stresses were smaller than 0.1 kPa. Thus, the findings in previously reported studies suggest some disagreement on the role of elevated excess pore pressures on *k*.

Ishihara [39] had observed that settlements can take place during shaking due to partial drainage. Since the rate of excess pore pressure generation exceeds the rate of dissipation during intense shaking the net accumulation of excess pore pressure is observed. However, with a considerable increase in *k*, the rate of dissipation during shaking might increase considerably to result in a lower overall rate and magnitude of excess pore pressure generated during ground motion compared to the case of constant *k*. Shahir et al. [1] extended the Manzari and Arulanandan [40] variable hydraulic conductivity model to account for the apparent dependence of *k* on r_u and it has been used in subsequent numerical studies [e.g., 35, 41-43]. The hydraulic conductivity relationship for dynamic phase is given by:

$$\begin{aligned} {k_m}/{k_i} &= 1 && r_u \le 0 \\ &= 1 + (\alpha - 1) \times r_u^{\beta_1} && r_u \le 1 \end{aligned} \tag{4}$$

$$= \alpha \qquad r_u > 1$$

whereas the relationship for reconsolidation phase is given by:

$$\begin{aligned} {k_m}/{k_i} &= 1 && r_u \le 0 \\ &= 1 + (\alpha - 1) \times r_u^{\beta_2} && r_u \le 1 \\ &= \alpha && r_u > 1 \end{aligned} \tag{5}$$

where k_m is the modified hydraulic conductivity, α is the factor by which hydraulic conductivity increases at $r_u = 1.0$, and β_1 and β_2 control the rates at which hydraulic conductivity increases with r_u during, and decreases with r_u following, shaking, respectively. Usually, the rate at which k decreases during reconsolidation has been observed to be higher than the rate at which k increases during shaking. At any particular r_u, k has been observed to be larger during shaking as compared to during reconsolidation [1, 35]. This is due to the fact that a reconsolidating liquefied soil mass has less void spaces between the grains as they settle in comparison to the same soil mass when it is in the process of getting liquefied (and hence the grains getting separated from each other) during cyclic loading. Shahir et al. [1] recommended values of 20, 1 and 8.9 for the variable hydraulic conductivity model constants α, β_1 and β_2, respectively, based on calibration to match the dynamic excess pore pressure generation and post-shaking dissipation rates observed in centrifuge tests on Nevada sand. Rahmani et al. [42], Shahir et al. [44] and Gao et al. [35] had suggested that the constants of the Shahir et al. [1] hydraulic conductivity model be calibrated for different sand types through laboratory studies.

In the present study, two sets of simulations were carried out for each test to examine the effects of using an r_u-dependent k. The first simulation was performed using the reported k (Table 2-2), which was kept constant throughout the simulation, whereas the second simulation implemented Equations 4 and 5 to allow the variation in k with r_u using a FISH function that

updated k in each element every 0.01 s based on the time-averaged r_u. Exponents β_1 and β_2 were set to 1 and 2, respectively, for all models, whereas α was iteratively adjusted until a reasonable match was observed with the dissipation rate in the experiment (discussed in Section 2.5). Table 2-4 summarizes the variable- hydraulic conductivity model parameters used for the sands considered in this study.

Table 2-4: Variable hydraulic conductivity model parameters used for the sands considered in this study.

No.	Sand	β_1	β_2	α	D_{10} (mm)
1	Hostun	1	2	1.2	0.209
2	Ottawa F-65	1	2	5	0.16
3	No. 306	1	2	20	0.147
4	M-1	1	2	15	0.12
5	Ottawa F-55	1	2	5	0.155

The α values found in this study were combined with those from previous studies [e.g., 1, 30, 32, 33, 35-38] to examine possible correlation, and indicated an apparent relationship with the effective grain diameter (D_{10}; Figure 2-5). The sands represented in Figure 2-5 are clean, uniformly-graded fine to medium sands with D_{10} between 0.09 and 0.22 mm. Previous studies have found that hydraulic conductivity [45, 46] and capillary rise [47] in clean sands can also be correlated with D_{10}. A negative power law-type correlation with D_{10} provides a reasonable approximation to much of the data ($R^2 = 0.42$). The original recommendation by Shahir et al. [1] is highlighted in Figure 2-5 and is in general agreement with the proposed correlation. The numerical study by Dobry et al. [37] is also highlighted as they reported an α value of 25 for Ottawa F-55 sand, higher than that obtained in this study ($\alpha = 5$) for the same sand and the R^2 for the proposed correlation improves to 0.64 when this data point is excluded. This correlation could be used to estimate α for clean sands when soil-specific data is not available, although a reasonable

range should be considered to estimate the sensitivity of the results to the selected α value based on the scatter in Figure 2-5.

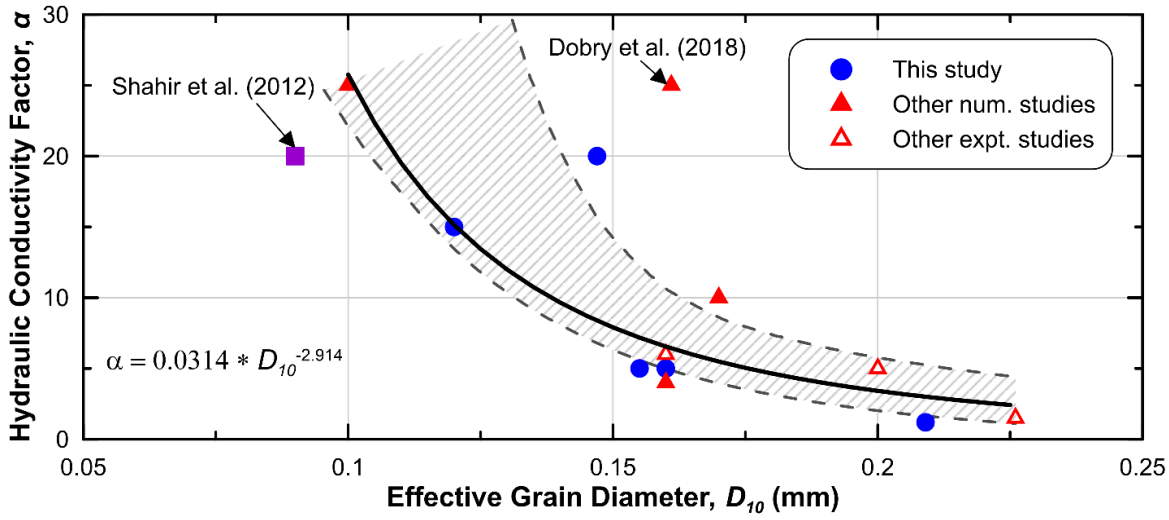

Figure 2-5: Relationship between α and D_{10} developed based on numerical simulations of experiments for five different sands. The power law correlation fit is based upon the results from the present study while the results from other numerical and experimental studies are also shown. The 95% confidence interval on the best fit relationship is highlighted with hatched lines.

2.4.4 INPUT MOTIONS

The various input motions used in the experiments selected for this study are shown in Figure 2-6. The tests were subjected to a variety of motions, including pseudo-harmonic, staged harmonic, and transient and are quantified in Table 2-1. Synthetic pseudo-harmonic motions with peak accelerations of 0.29g, 0.18g and 0.09g were used for the experiments on Hostun, No. 306 and M-1 sands, respectively. The frequencies of the motions used for these three tests were 1, 2, and 2 Hz, respectively. The experiment on Ottawa F-55 sand used a series of synthetic harmonic input waves at a frequency of 2 Hz that were applied in four stages. The peak accelerations for the four successive motions were 0.01, 0.05, 0.15 and 0.3g. The first motion was applied for a duration of 5 s whereas the following three motions were applied for durations of 10 s each. A linearly scaled

version of the fault normal horizontal component of the 1995 Kobe earthquake motion (M_w = 6.9) recorded at the Takatori station in Kobe, Japan was used for the experiment on Ottawa F-65 sand. The motion had a peak acceleration of 0.41g, significant duration of 12 s and a mean spectral period of 0.87 s (1.15 Hz). The base acceleration from the experiments were applied to the base of the models as horizontal acceleration time histories during the dynamic phase of the simulation procedure. The recorded base motion was available for the test on Ottawa F-65 sand, while target motions were used for the other experiments.

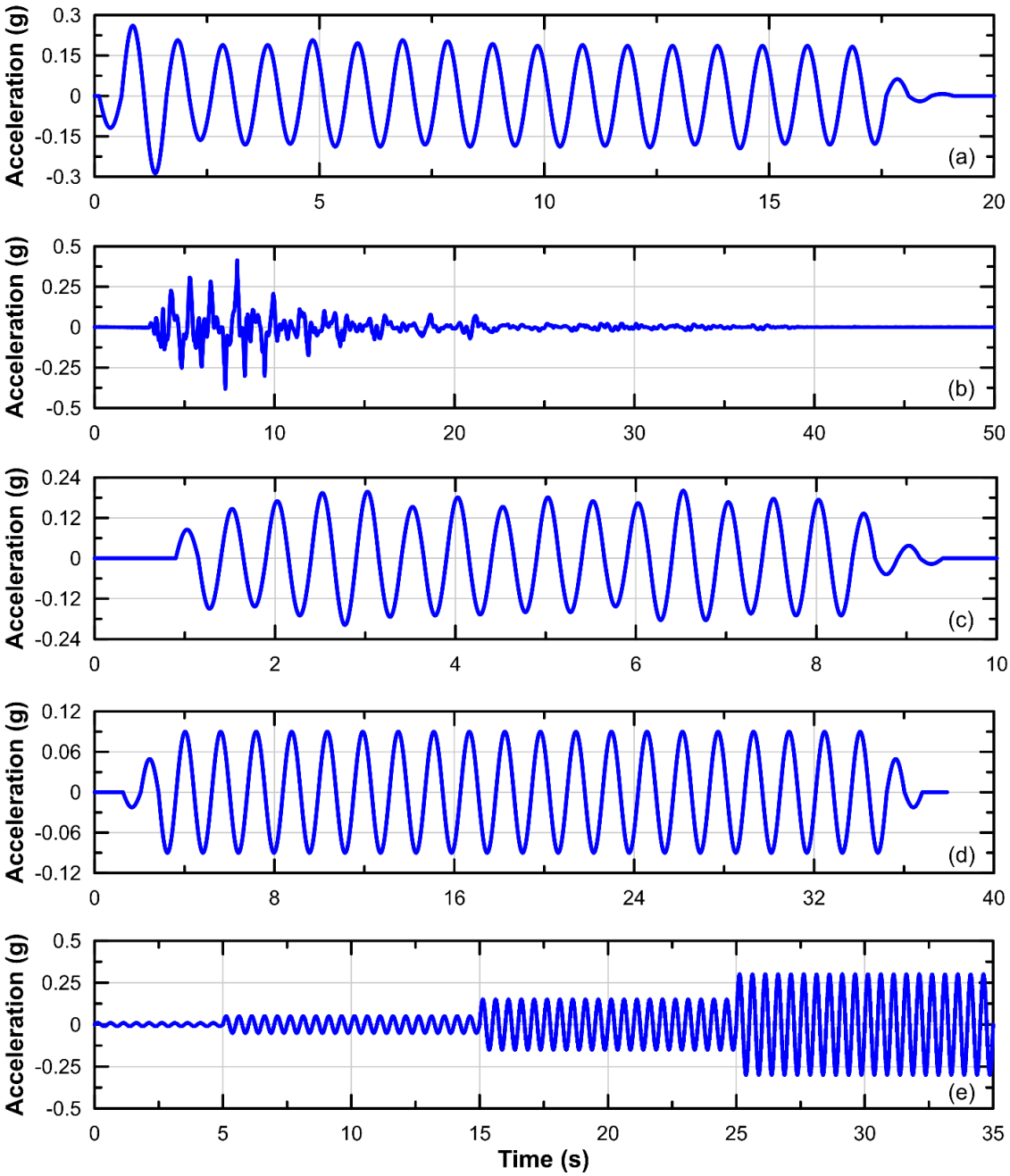

Figure 2-6: Acceleration time histories used as input motions for the experiments by (a) Adamidis and Madabhushi [2] (b) Ramirez et al. [3] (c) Mehrzad et al. [4] (d) Ecemis [5] (e) Thevanayagam et al. [6].

2.5 RESULTS

Numerical simulations were performed in FLAC 8.0 for each of the five experiments considered. For each experiment, two simulations were conducted: one assuming a constant k (CK) throughout the entire duration, the other using the r_u-dependent k (VK) relationship by Shahir et al. [1] with the coefficents in Table 2-4. Additionally, simulations using a half timestep, half mesh size, and 2D model were performed for the test on Hostun sand to examine the sensitivity of the results to these model conditions.

2.5.1 SIMULATION OF CENTRIFUGE TESTS

This section highlights the excess pore pressure and settlement responses from the centrifuge test simulations and their comparison to experimental observations. Figure 2-7 shows the time histories of excess pore pressure during shaking and reconsolidation from the CK and VK model simulations compared to corresponding experimental observations. The original study [27] presented isochrones of excess pore pressure at fixed time intervals at the center of the Hostun sand model for the dissipation phase. In general, the end-of-shaking excess pore pressures were reasonably predicted for all three tests although the excess pore pressures at greater depths are slightly underpredicted by the simulations. As compared to the CK model, greater excess pore pressure dissipation occurred in the VK model during the last few seconds of shaking (when the motion intensity starts decreasing). The excess pore pressure dissipation rate following shaking was underpredicted with the CK simulations, requiring as much as 30 times the duration of dissipation compared to the experimentally-observed excess pore pressures for the tests on Ottawa F-65 and No. 306 sands. The VK simulations resulted in an improved prediction of dissipation rate, especially for the tests on Hostun and No. 306 sand. However, considerable differences in the shape of the dissipation curves exist between simulated and observed responses. The reasons for

this difference are unclear, but could be due to a simultaneous dissipation of excess pore pressure in vertical and radial directions that took place in the experiments which was not possible to replicate in a 1D or 2D numerical simulation (e.g., horizontal flow in the out of plane direction and/or upward flow at the boundaries of the laminar boxes).

The results shown in Figures 2-7c and 2-7d use a D_r of 75% for the dense Ottawa F-65 sand layer (8 – 18 m) at the model base instead of the D_r of 90% reported by Ramirez et al. [3]. The experimental results showed considerable excess pore pressure generation within this layer, which was not seen when the reported D_r was used in the simulation (Figure 2-8). It is common to observe considerable mismatch in D_r estimated from mass-volume based measurements in contrast to D_r evaluated from CPT based measurements [48]. No CPT measurements are available for this study, but the modified value of D_r substantially improves the prediction of excess pore pressures for the layer (Figure 2-7c).

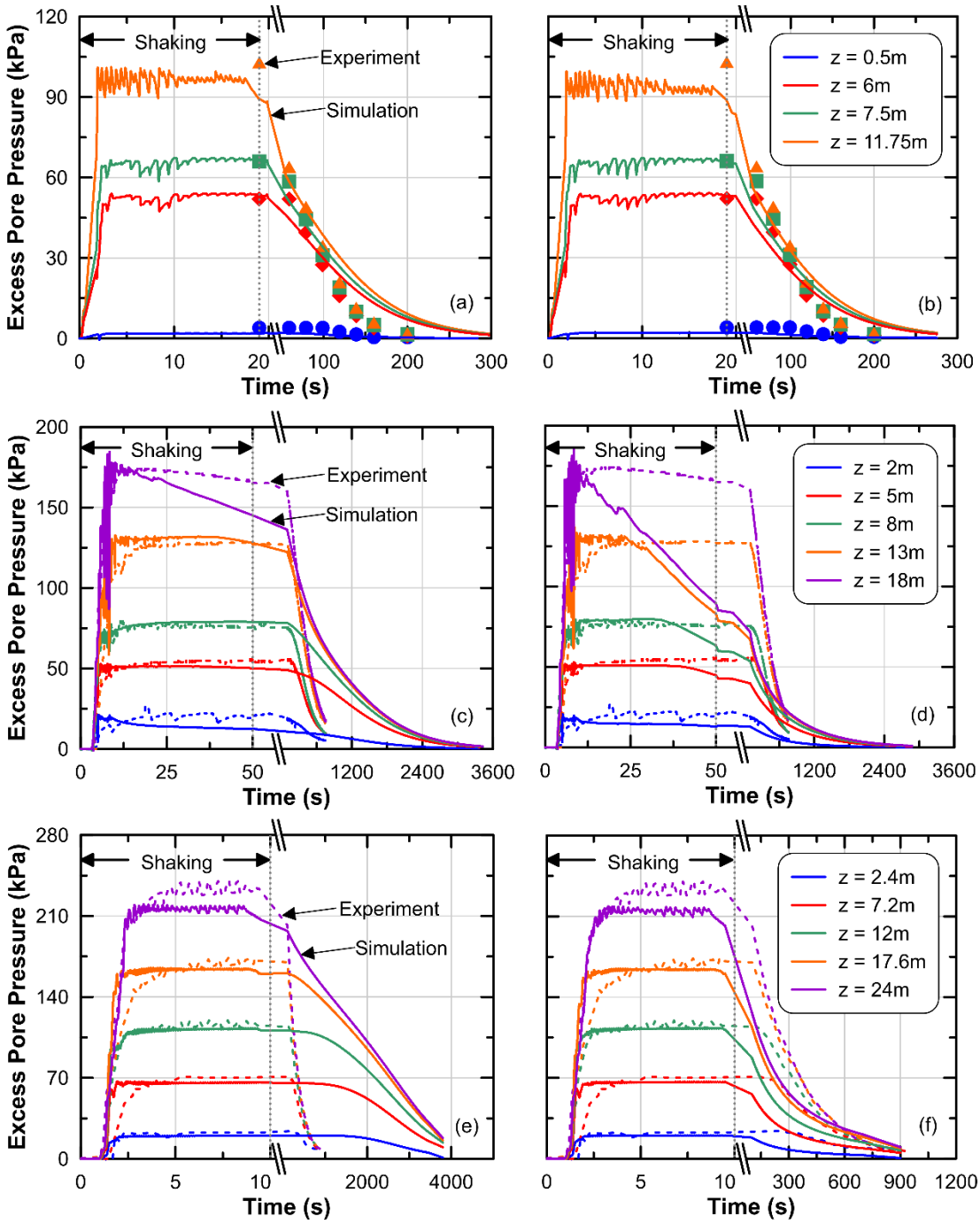

Figure 2-7: Excess pore pressure time histories for the centrifuge tests on (a) Hostun sand – CK model (b) Hostun sand – VK model (c) Ottawa F-65 sand – CK model (d) Ottawa F-65 sand – VK model (e) No. 306 sand – CK model (f) No. 306 sand – VK model. Dashed lines represent the experiment and solid lines represent the simulations.

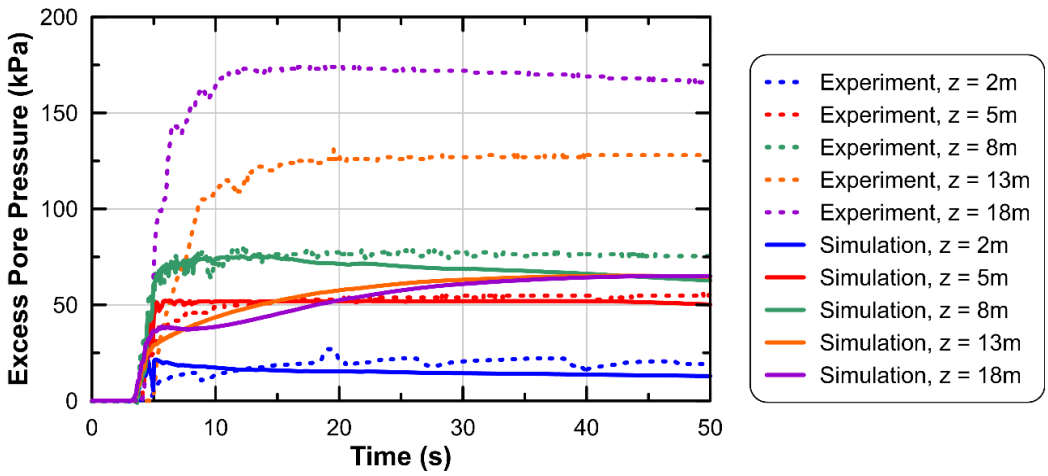

Figure 2-8: Dynamic phase excess pore pressure time histories compared between the numerical simulation and experiment considering a D_r of 90% for the dense Ottawa F-65 sand layer (as reported) and the CK model. Dashed lines represent the experiment and solid lines represent the simulations.

The simulated settlements are compared with the corresponding experimental values in Figure 2-9. For the test on Hostun sand, the default PM4Sand reconsolidation parameters overestimate the magnitude of total settlement (dynamic + reconsolidation) by a factor of approximately two (Figure 2-9a). However, using the soil-specific reconsolidation parameters (Figure 2-4), the total settlements from the simulations for both the hydraulic conductivity models agree with the experimental settlements (within 2%) as shown in Figure 2-9b. For the test on Ottawa F-65 sand, the CK simulation predicted the settlement fairly accurately (within 3%) whereas the VK simulation resulted in an underprediction of 21% (Figure 2-9c). Significant settlement (21.6 cm) occurred during shaking in the experiment, an observation that was not well-replicated in the numerical simulations, which produced settlements of 0.86 cm and 2.04 cm for the CK and VK models, respectively. The rate of settlement from the experiment was not captured by either simulation. For No. 306 sand, the total settlement was underpredicted by both the CK (36% underprediction) and VK (32% underprediction) simulations (Figure 2-9d). The small

dynamic settlement of 1.1 cm that was observed in the experiment was reasonably estimated by the VK simulation. The settlement rate generated by the VK simulation, however, agreed with the experimental settlement rate, whereas the CK model simulation did not.

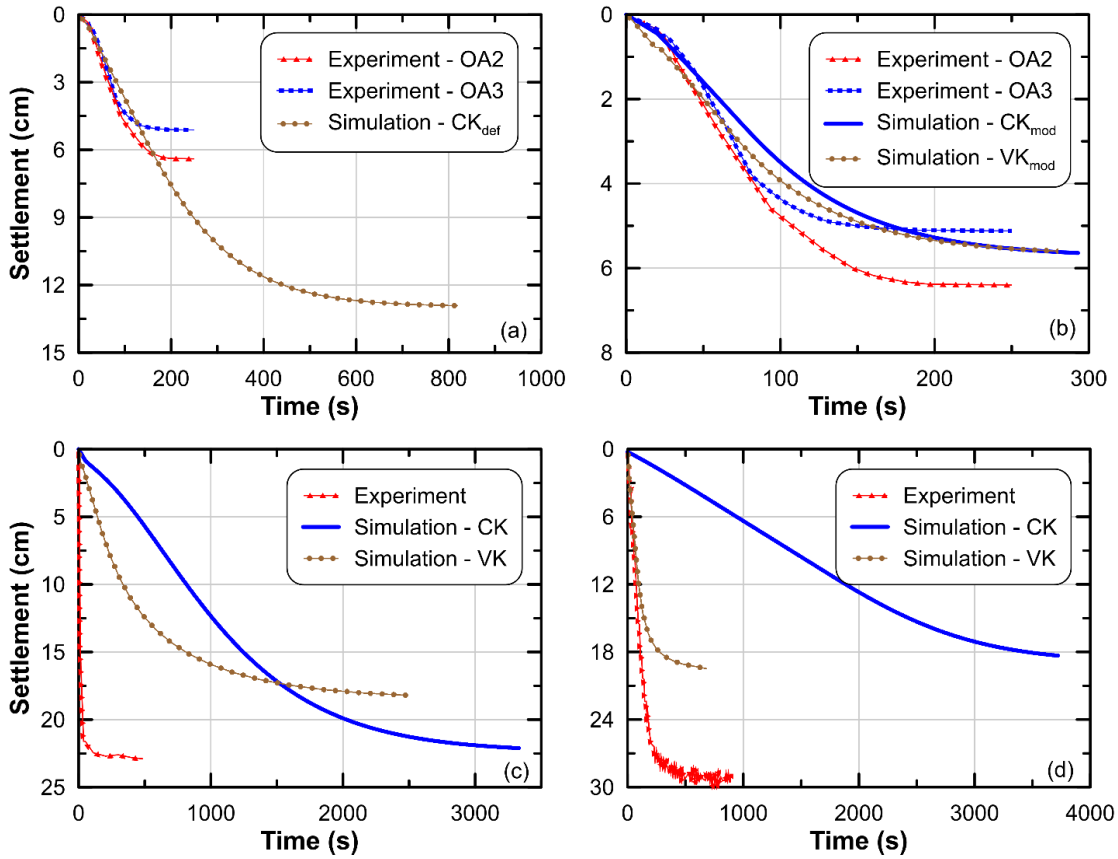

Figure 2-9: Settlement time histories for the centrifuge tests on (a) Hostun sand – default reconsolidation calibration (b) Hostun sand – modified reconsolidation calibration (c) Ottawa F-65 sand (d) No. 306 sand.

Simulations were repeated for the Hostun sand centrifuge model using half the default timestep, half the mesh size (0.25 m square elements instead of 0.5 m), and in 2D with the same dimensions as the centrifuge model (excluding the container). All of these simulations used the modified reconsolidation calibration (Figure 2-4). The settlement results from these simulations are compared with the baseline results (constant *k* with the modified reconsolidation parameters)

in Figure 2-10. The changes in time-step and mesh size have a negligible effect on the model response. Results from the 2D mesh are in close agreement with the settlement from the 1D model for points at the center of the container. This result is expected as the experiments selected for this study were attempting to approximate 1D conditions.

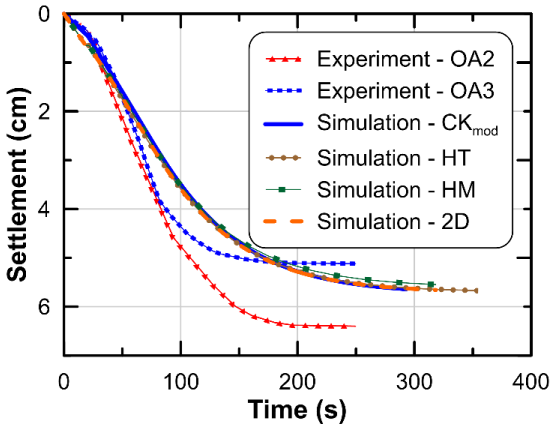

Figure 2-10: Time histories of total settlement for Adamidis and Madabhushi [2] centrifuge tests and numerical simulations from the sensitivity analysis study using half timestep (HT), half mesh size (HM) and 2D mesh.

2.5.2 SIMULATION OF SHAKE TABLE TESTS

The excess pore pressure and settlement responses from the shake table simulations and corresponding experimental observations are outlined in this section. Figure 2-11 compares the observed time histories of excess pore pressure to the results of the CK and VK model simulations. The end-of-shaking excess pore pressures were reasonably predicted for the two shaking table tests, although the excess pore pressures at greater depths in the M-1 sand simulations were slightly underpredicted (Figures 2-11a-b). Both simulations returned partial, in-shaking drainage which was not observed for the shaking table test on Ottawa F-55 sand (Figures 2-11c-d). The post-shaking excess pore pressure dissipation rate was underpredicted with the CK simulations,

requiring 6 times the duration of dissipation compared to the experimentally-observed excess pore pressures. The VK simulations resulted in an improved prediction of dissipation rate for the test on M-1 sand. However, other than the VK simulation on M-1 sand, the shape of the dissipation curves produced from the simulations were different from the corresponding experiments.

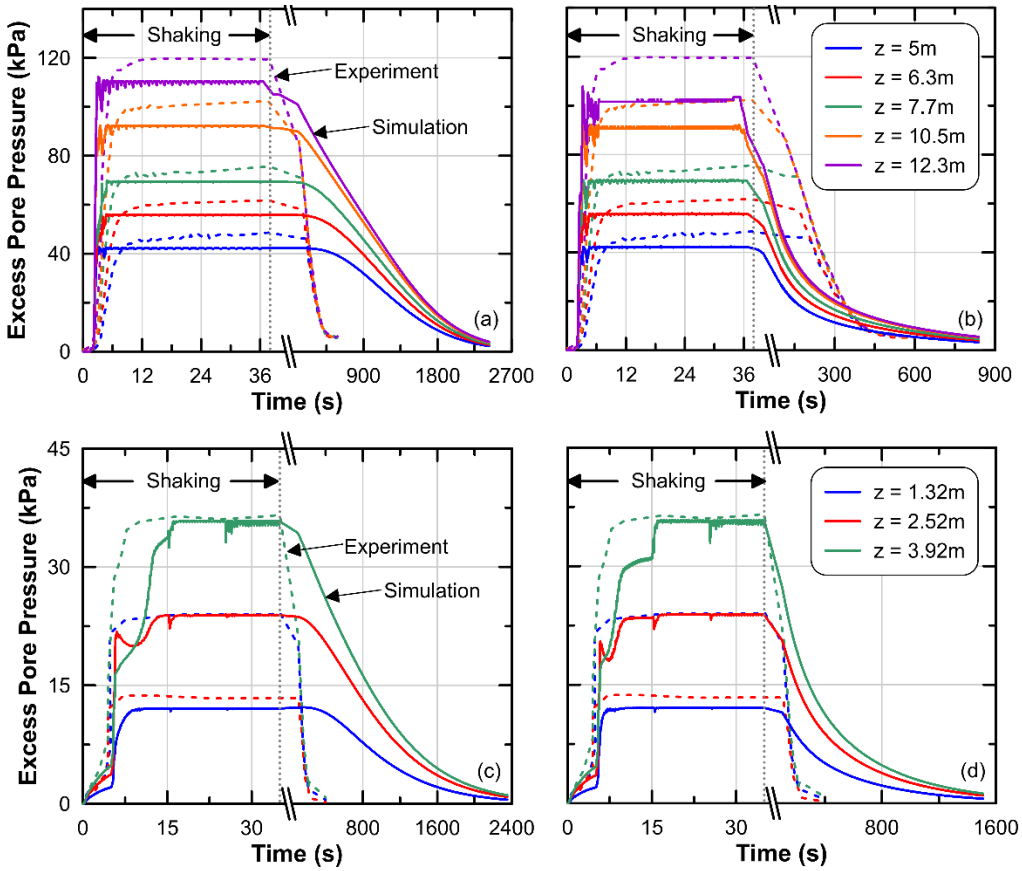

Figure 2-11: Excess pore pressure time histories for the shake table tests on (a) M-1 sand sand – CK model (b) M-1 sand – VK model (c) Ottawa F-55 sand – CK model (d) Ottawa F-55 sand – VK model. Dashed lines represent the experiment and solid lines represent the simulations.

The comparison between the experimental and simulated settlements is presented in Figure 2-12. The CK and VK models underpredicted the total settlement for the M-1 sand shaking table test by 23 and 10%, respectively, whereas total settlement was under predicted by 12 and 20%, respectively for the Ottawa F-55 sand shaking table test. Dynamic settlements were observed in the experiments and calculated in the VK simulations, and although underpredicted, produced

slightly improved agreement compared to the CK model simulations. In contrast to the CK model, the VK model simulations were able to predict the settlement rate better, especially for the M-1 sand.

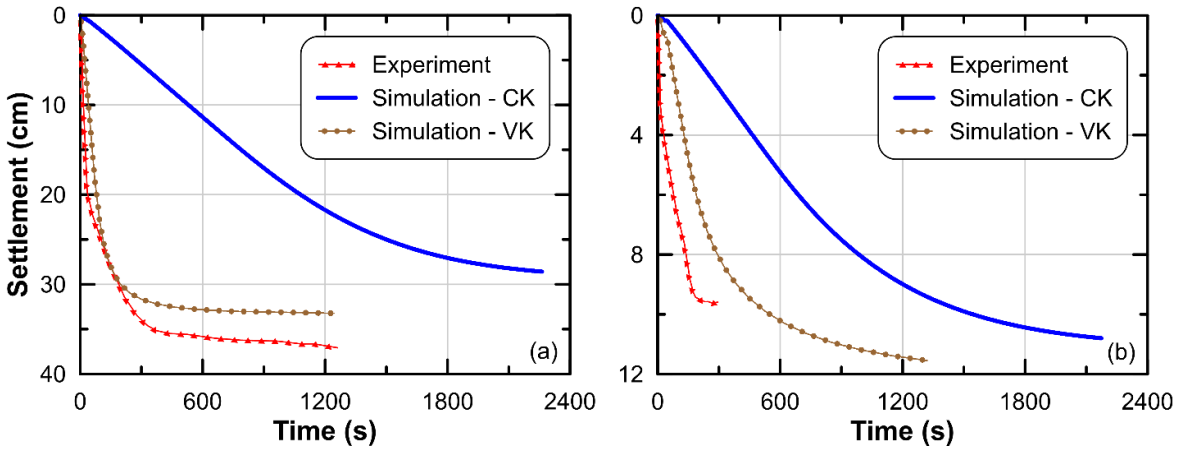

Figure 2-12: Settlement time histories for the shake table tests on (a) M-1 sand (b) Ottawa F-55 sand.

2.6 DISCUSSION

The total settlements from the constant and variable hydraulic conductivity simulations are compared with the experimentally-derived settlements in Figure 2-13. For ease of comparison, the total settlement (including dynamic and reconsolidation settlements) from the experiments and simulations were normalized by the total height of the liquefiable layer. The numerically-derived settlement from all of the tests was observed to lie within 60 to 125% of the corresponding experimental settlement, with settlements underpredicted on average. Part of this underprediction of settlements could be due to experimental conditions that were not replicated in the simulations, such as compression of non-liquefiable layers, displacement of sensors in liquefied soil, or multi-directional shaking. This level of uncertainty is slightly smaller than the magnitudes that have been observed for other liquefaction problems (commonly 50% - 200%), such as lateral

displacements observed in post-earthquake reconnaissance [49], as well as in centrifuge tests [26], and free-field settlements observed in numerical study [50], as well as in the field such as in Christchurch [51]. Simulations based on the Hostun and Ottawa F-65 sand models exhibited the best agreement in settlement for both sets of simulations. While soil-specific reconsolidation calibration was performed for Hostun sand, Vargas et al. [24] found that the Ishihara and Yoshimine [12] framework (and, therefore, the default PM4Sand reconsolidation calibration) were a reasonable match to the volumetric strains observed during reconsolidation of Ottawa F-65 sand. This indicates that a soil specific calibration may be necessary for both excess pore pressure generation (as is commonly recognized) and dissipation.

The use of the r_u-dependent k improved settlement predictions for the No. 306 sand and M-1 sand, while overpredicting settlement for Ottawa F-55 sand. Goodness of fit statistics summarizing the accuracy of simulations using the r_u-dependent k (Table 2-5) indicate that the VK simulations exhibited improved coefficients of determination, R^2, lower mean squared errors (MSE), and prediction bias (defined as the ratio of observed and simulated normalized settlement). Prediction uncertainty, quantified by the coefficient of variation, defined as ratio of the standard deviation in bias and the mean bias, equaled 24 and 22% for the CK and VK models, respectively. These results demonstrate that the VK simulations were more accurate and exhibited less variability in prediction accuracy than the CK model simulations in predicting total settlements, but the magnitude of the improvement was not large.

The variation in bias in predicted settlement with effective grain diameters, D_{50} and $D_{10,}$ is shown in Figure 2-14 for each of the simulations. The simulations with the default calibration tend to overpredict settlements for those tests with finer soils, and underpredict settlements for tests with coarser soils. Settlement was accurately predicted for Hostun sand (as discussed earlier) using

the soil-specific $f_{sed,min}$ calibration, as is indicated by a bias of 0.98 in Figure 2-14. These data suggest that the post-liquefaction stiffness (and therefore the settlements) may be correlated with the grain size of the soil, but all of the soils tested were relatively uniform clean sands characterized by a limited range in D_r. Additional study of nonplastic soils of smaller and larger grain size should be performed to verify the observed trend and possibly establish correlations between the grain size distribution of the soil and their reconsolidation behavior.

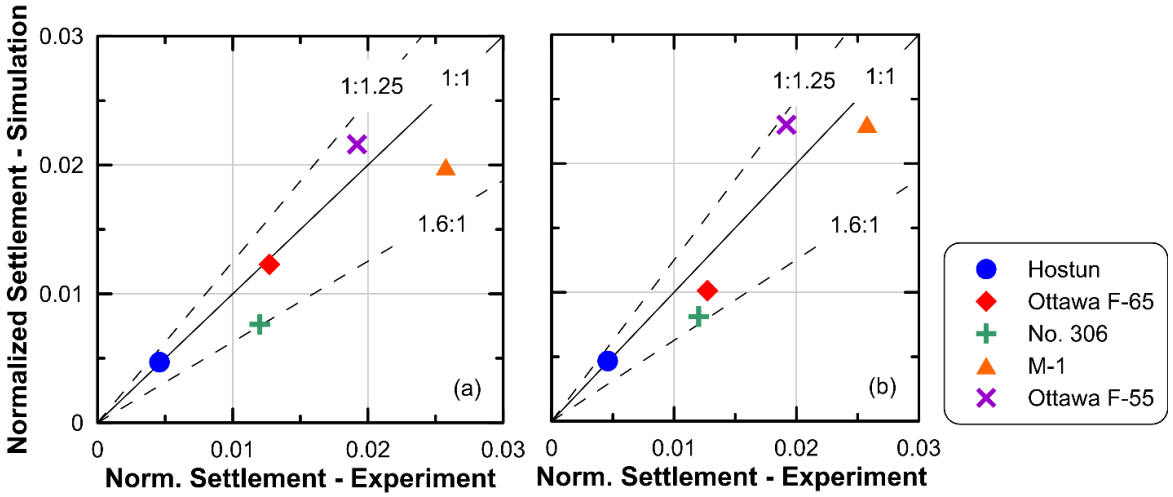

Figure 2-13: Normalized settlements from simulations using the (a) CK model and the (b) VK model compared to the normalized experimental settlements.

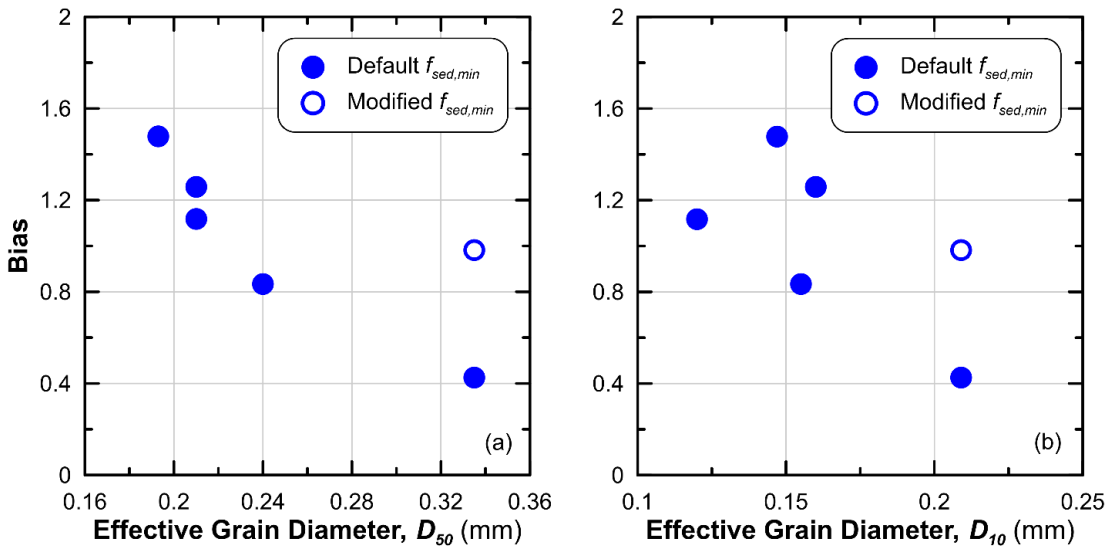

Figure 2-14: Correlation between observed bias and (a) D_{50} (b) D_{10} for each test considered in this study.

Table 2-5: Statistical parameters corresponding to the numerical fit of centrifuge settlements based on the tests considered in this study.

Parameter	CK model	VK model
R^2	0.818	0.873
MSE	1.394	1.335
Mean bias	1.154	1.134
COV(bias)	0.24	0.22

Table 2-6 lists both the dynamic and total settlements for the five experiments considered in this study. The VK model was more successful than CK model in reasonably predicting the dynamic and total settlement simultaneously, when dynamic settlement was a small fraction of the total settlement, as observed for No. 306 sand. Since reconsolidation effects (set through the PM4Sand flag variable *PostShake*) in PM4Sand are not activated during shaking, PM4Sand is incapable of predicting large dynamic reconsolidation settlements. Therefore, when dynamic settlement was a large fraction of the total settlement, the VK model underpredicted this

component of settlement, as observed for the M-1, Ottawa F-55 and Ottawa F-65 sand model, a limitation of the phenomenological approach used with the PM4Sand model.

Table 2-6: Experimental and numerical settlements observed for the five different tests considered in the current study.

No.	Sand	Settlement - Experiment (cm)		Settlement - Simulation (cm)			
				CK model		VK model	
		Dynamic	Total	Dynamic	Total	Dynamic	Total
1	Hostun	0	5.5	0.46	5.64	0.78	5.6
2	Ottawa F-65	21.6	22.9	0.86	22.1	2.04	18.2
3	No. 306	1.1	28.82	0.29	18.33	1.08	19.5
4	M-1	19.5	37.1	0.5	28.6	9	33.2
5	Ottawa F-55	4.15	9.59	0.18	10.8	0.72	11.5

The current study has focused on reconsolidation settlements for free-field sites with level ground. The simulations and experiments examined herein did not address many other important influences on settlement, such as ejecta (not observed in these experiments), soil-structure interaction, stratigraphy, sloping ground, soil fabric or aging, fines content, and spatial variability. The uncertainty in agreement between the simulations and the experiments was within a reasonable range for geotechnical systems (COV in bias of 22 to 24%). While factors such as ejecta and stratigraphy are commonly recognized as important influences on reconsolidation settlements, the effect of the post-liquefaction compressibility of the soil deposit has not been commonly recognized as being important. The current study demonstrated that different soils may require different calibrations for both the magnitude of volumetric strains and changes in hydraulic conductivity due to excess pore pressures, where the latter effect appears related to measures of grain size. A preliminary correlation between the magnitude of hydraulic conductivity increase due to liquefaction has been developed in this study and may allow a tentative adjustment to

hydraulic conductivity to be made until this effect is further investigated and the correlation validated for other soils, including natural soils.

2.7 CONCLUSIONS

This chapter highlighted some of the key aspects on numerical modeling of liquefaction and post-liquefaction responses. Three centrifuge experiments and two shake table tests were numerically modeled in FLAC using the constitutive model PM4Sand. PM4Sand was calibrated to match the cyclic strength of the soils at the target relative density (D_r) using either laboratory test results or by matching the excess pore pressure generation during shaking. An excess pore pressure ratio (r_u)-dependent hydraulic conductivity (k) model was implemented to examine the effect of k on the responses. PM4Sand was able to reasonably reproduce the excess pore pressure generation from the experiments, but the prediction accuracy of the observed rates of dissipation varied. Similarly, the magnitude of settlement from the simulations was within 60 to 125% of the observed settlements for all of the experiments. On average, settlements were underpredicted by approximately 15%. This may be partially attributed to settlement mechanisms that were not present in the simulations, such as compression of non-liquefiable layers, ratcheting of displacement sensors into liquefied soil, or possible multi-directional shaking in the centrifuge.

Some of the other key findings and observations from this study are outlined:

- A new, tentative relationship was developed between the increase in hydraulic conductivity due to liquefaction and the effective grain diameter of the soil (D_{10}). This relationship considered the five experiments from this study along with data from eight other studies. While the dataset exhibits scatter, the magnitude of the increase in hydraulic conductivity is observed to decrease with increasing D_{10}. This observation helps to reconcile some of

the conflicting observations previously reported in the literature and provides a means to estimate the hydraulic conductivity of liquefied clean sands when laboratory data is not available.

- The results of this study highlight the importance of soil-specific reconsolidation parameters in numerical simulations examining liquefaction. The dynamic calibration of a numerical model is often soil-specific but standard empirical relationships like Ishihara and Yoshimine [6] are commonly used to calibrate reconsolidation parameters. The experiments in this study show that this can result in considerable overestimation or underestimation of reconsolidation settlements. Soil-specific reconsolidation calibration may be needed to improve agreement of simulations and observations. The centrifuge test on Hostun sand demonstrated that calibrating the model to laboratory data for the compressibility of soils at low effective stresses can greatly improve the prediction settlement. Additional work is needed to measure the compressibility of other liquefied soils, including natural soils to confirm this finding.
- The bias in settlement predictions was observed to correlate to measures of grain size for the sands examined in this study. Additional tests on other soils with a wider range of grain sizes are needed to determine if correlations can be developed between reconsolidation parameters and the grain size of the soil.
- Reconsolidation behavior in the PM4Sand model is activated after shaking has ended and therefore large dynamic settlements cannot be predicted with this approach without losing substantial excess pore pressures. For example, the experiment on Ottawa F-65 sand showed most of the settlement to occur during dynamic phase which is not replicated in the simulations even though the total settlement was accurately estimated. However, small

dynamic settlements like those observed for the tests on No. 306 sand can be predicted using a variable *k* model while also preserving the excess pore pressures during shaking. The variable *k* model incorporated in the present study was found to be useful in accurate prediction of both small dynamic settlements as well as settlement rates but requires soil-specific calibration.

The current study considered the relatively simple problem of 1D reconsolidation settlement but highlighted some of the significant sources of uncertainty that exist when attempting to model this problem numerically. Other authors have pointed out other sources of uncertainty that exist when moving to field conditions [51-54]. An important area for future study, numerical examination of these factors is needed using well-characterized field sites where liquefaction-induced settlements have been recorded.

CHAPTER 3: INVESTIGATION OF THE KEY ISSUES IN SIMULATING CENTRIFUGE EXPERIMENTS ON A SHEET-PILE WALL EMBEDDED IN A LIQUEFIABLE SAND

This chapter is based on a paper about to be submitted by Devdeep Basu, Jack Montgomery, Renmin Pretell and Katerina Ziotopoulou to the journal *Soil Dynamics and Earthquake Engineering.*

Basu, D., R. Pretell, J. Mongomery, and K. Ziotopoulou. 2021. "Investigation of the key issues in simulating centrifuge experiments on a sheet-pile wall embedded in a liquefiable sand." Soil Dynamics and Earthquake Engineering (Elsevier). Manuscript Ready.

This chapter was altered from the version that will be submitted to *Soil Dynamics and Earthquake Engineering* for the purpose of avoiding redundancy and maintaining better flow in this dissertation. My primary contributions to the paper included: (i) evaluating the ability of the chosen set of numerical tools and protocols to reasonably capture the responses observed in centrifuge tests (ii) investigating the importance of accurate estimation of relative density in simulating centrifuge tests, (iii) gathering and reviewing literature, (iv) development and design of numerical approach, (v) processing, analyzing, and interpretation of the results, (vi) most of the writing.

3.1 ABSTRACT

This chapter presents results from numerical simulations of a series of centrifuge model tests performed as part of the LEAP 2020 simulation exercise. The prescribed centrifuge experiments featured a sheet pile retaining wall supporting a liquefiable deposit of Ottawa F-65 sand. A description of the selected constitutive model PM4Sand v3.1 and the numerical platform FLAC v8.0 are presented. The constitutive model parameters are obtained through calibration to available

laboratory data on Ottawa F-65 sand. The simulations use the achieved soil density, base excitation, and structural properties of the wall. This chapter presents a description of the numerical modelling approach and a comparison of the simulation results with the experimental results. Accurate estimation of relative density is observed to be important for reasonable prediction of responses. The influence of permeability variation due to liquefaction on the responses is evaluated. A sensitivity study is conducted to examine trends in the simulation response.

3.2 INTRODUCTION

The previous chapter discussed the ability of the selected numerical tools and protocols to capture post-liquefaction responses for free-field sand deposits. This chapter aims to extend the numerical framework discussed in the previous chapter to a geosystem that involves soil-structural interactions. Centrifuge experiments on a stratified sand deposit retained by a sheet pile wall are numerically modeled to evaluate the efficacy of the numerical approach in predicting the responses observed from the experiments.

Laboratory tests like centrifuge experiments present their own set of uncertainties in terms of achieving the target geotechnical properties and boundary conditions. The relative density (D_R) achieved across a soil layer often shows considerable variability due to physical constraints encountered during placement of sand into the centrifuge container or inaccuracies in measurements [1]. Hence, considering a single representative value of D_R for an entire layer might be an over-simplification. Moreover, there could also be a mismatch between the D_R estimated based on the mass and volume of sand placed and the D_R estimated using cone penetration test (CPT) measurements [1]. Permeability of a sand layer is also likely to increase by a factor with the onset of liquefaction as soil grains start losing contact with each other [2, 3]. Estimation of this

factor is often difficult and not commonly performed in the laboratory. Therefore, careful consideration of these uncertainties is essential while validating numerical results to laboratory observations.

The Liquefaction Experiments and Analysis Project (LEAP) is an international collaborative project undertaken with the goal of verification and validation of numerical liquefaction models utilizing high-quality data from element tests and centrifuge experiments. This chapter presents the results from a numerical study performed as part of the LEAP-2020 exercise that aims at simulating centrifuge tests modeling a soil-retaining wall system. The simulations described herein use the numerical platform FLAC 8.0 [4] and the constitutive model PM4Sand v3.1 [5]. The main objectives for the analyses are: (1) to establish the ability of the chosen set of numerical tools and protocols to reasonably capture the experimentally observed responses, (2) to investigate the importance of accurate estimation of relative density (D_R) for reliable numerical predictions of post-liquefaction responses; and (3) to study the influence of permeability on observed responses like excess pore pressure, lateral displacement and settlement. This study also provides a description of the simulation approach and features of the selected numerical platform and constitutive model. The constitutive model is calibrated using the results of laboratory experiments [6] conducted on Ottawa F-65 sand. The calibrated model is used to perform system level simulations of the centrifuge model tests, followed by comparisons between numerical and experimental responses. Effects of variations in D_R and permeability on the system response are evaluated in order to assess the overall efficacy and sensitivity of the selected numerical framework and constitutive model in predicting the centrifuge responses. Implications of this study for future simulations involving liquefaction and soil-structure interaction are discussed.

3.3 BRIEF DESCRIPTION OF CENTRIFUGE MODEL TESTS

Simulations are performed for the 11 centrifuge tests of the LEAP 2020 exercise [7] performed at different geotechnical facilities across the world. Five centrifuge tests were performed at Rensselaer Polytechnic Institute (RPI), two at Kyoto University (KyU), and one each at University of California Davis (UCD), Zhejiang University (ZJU), Ehime University (EU), and Korea Advanced Institute of Science and Technology (KAIST). The centrifuge experiments were conducted under an acceleration field that was several times larger (N_g) than the acceleration due to gravity (g). This enabled the use of a small-scale model to represent a full-scale prototype geotechnical system whose dimensions were scaled down as per relevant centrifuge scaling laws [8]. The specimen was built in a container having rigid walls. The soil was saturated using a viscous fluid having a viscosity N times higher than that of water to ensure consistency between dynamic and diffusion time scaling factors. The centrifuge model was spun up to the target acceleration field in stages. CPT tests were conducted prior to shaking for all the experiments except KyU-1 and KyU-3. Thereafter, the model was subjected to an input motion (earthquake shaking) applied at the base.

The geotechnical system modeled was a sheet pile wall retaining a deposit of liquefiable backfill. The prototype geometry (20 m width) along with the numerical mesh is shown in Figure 3-1. The model consisted of two soil layers and a sheet pile wall (Figure 3-1). Table 3-1 outlines the details of the acceleration field and wall properties utilized for each test. The soil units were comprised of a layer of dense Ottawa F-65 sand (D_R = 90%) at the bottom of the model overlain by a layer of loose Ottawa F-65 sand (mass and CPT - based D_R estimates for various tests outlined in Table 3-2), sub-divided into two units: ‘toefill’ (in front of the wall) and ‘backfill’ (behind the wall). Unless noted otherwise all units and analyses presented herein are in prototype scale. The

aluminum sheet pile wall was embedded 0.5 m into the dense sand layer, and it extended between 2.5 m to 4 m above the backfill surface for the various centrifuge tests. Pore pressure transducers and accelerometers were installed at various depths in the soil deposit both behind the wall as well as in front of it to record excess pore pressures and acceleration time histories, respectively. Linear variable differential transformers (LVDTs) were installed at the soil surface to record settlements and on the sheet pile wall to monitor its lateral movements during the test.

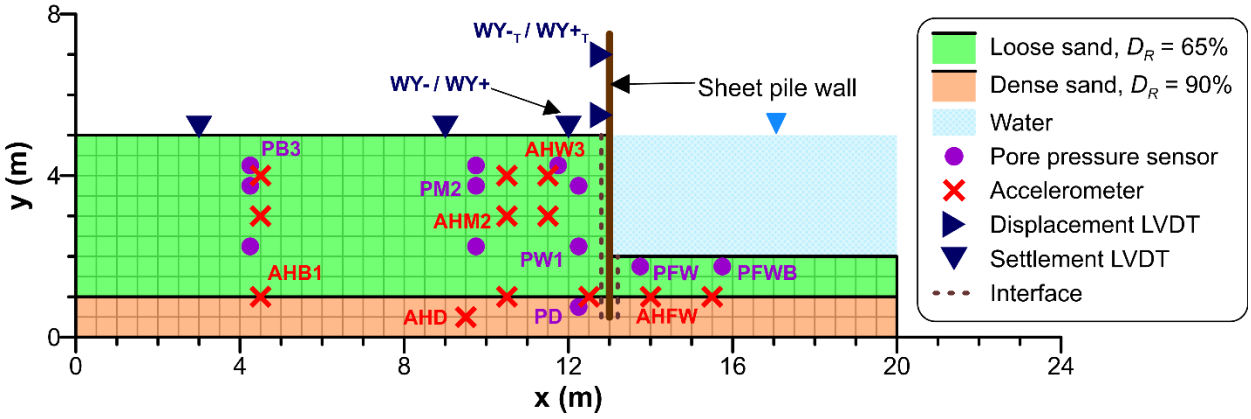

Figure 3-1: Geometry of the numerical setup in FLAC (prototype scale). The locations of the sensors correspond to RPI-9.

Table 3-1: Some of the main features of the centrifuge experiments.

Centrifuge Facility	Test No.	Acceleration (g)	Wall properties (E = 6.89 GPa, I = 0.0001 m^4)	
			Density (kg/m^3)	Cross-sectional area (m^2)
RPI	9	23	2740	0.11
RPI	10	23	2740	0.11
RPI	11	23	2740	0.11
RPI	12	23	2740	0.11
RPI	13	23	2740	0.11
EU	2	40	2680	0.12
KyU	1	40	2710	0.12
KyU	3	40	2710	0.12
KAIST	2	40	2720	0.112
UCD	1	27	2740	0.11
ZJU	1	26	2800	0.12

3.4 NUMERICAL MODEL

In this study, the geotechnical model described in section 3.3 is numerically simulated using the numerical platform FLAC 8.0 [4] and the nonlinear constitutive model PM4Sand v3.1 [5]. Time histories of excess pore pressure, shear strain, horizontal and vertical displacements were recorded during the simulations at locations corresponding to the sensors (as shown in Figure 3-1) in the centrifuge experiments.

3.4.1 CALIBRATION

The model calibration is performed through single-element simulations of undrained cyclic stress-controlled direct simple shear (herein denoted as DSS) tests with a goal to reasonably capture the behavior observed for undrained cyclic stress-controlled DSS tests on Ottawa F-65 sand performed in the laboratory. The best-fit triggering curve to the laboratory test data on Ottawa F-65 sand is used as the target for the calibration procedure. The primary PM4Sand model parameters that are calibrated are D_R (selected value as reported or calculated from CPT measurements), the contraction rate parameter h_{po}, and shear modulus coefficient G_o. Additionally, the n_b parameter, maximum void ratio e_{max}, minimum void ratio e_{min} and critical state friction angle Φ'_{cv} are also calibrated based on the relevant data available on Ottawa F-65 sand. Default values reported in Boulanger and Ziotopoulou [5] are used for all other PM4Sand parameters. h_{po} and n_b control the bounding ratio and therefore the dilatancy and peak effective friction angles while G_o relates to the shear wave velocity of the sand. The values of h_{po} are adjusted according to D_R (Table 3-2) to reach a double amplitude shear strain of 6% in 15 loading cycles at the cyclic stress ratio established by the triggering curve (Figure 3-2). The triggering curve is developed by fitting the available cyclic strength data on Ottawa F-65 sand [9-15] using a functional form similar to the one developed by Idriss and Boulanger [16]. It must be noted that this curve does not pass exactly through all of the

data points but attempts to provide the best fit to the combined data set. The n_b parameter is assigned a value of 0.6 to match the rate of strain accumulation for Ottawa F-65 sand as suggested by Tasiopoulou et al. [17]. The values for G_o are selected by using the same functional form as PM4Sand manual [5] but modified slightly to better match the shear wave velocity (and therefore maximum shear modulus G_{max}) data for Ottawa F-65 sand [6]. Equation 1 shows the G_o relationship used for this study.

$$G_o = 10.606\ (D_R) - 229 \tag{1}$$

where D_R is in %. The critical state friction angle Φ'_{cv} is reduced to 30° from the PM4Sand default value of 33°, to better match the slope of the frictional envelopes (bounding line) of the stress path plots from the cyclic DSS tests. A friction angle of 30° for Ottawa F-65 sand is also consistent with the results reported by Parra Bastidas [18] based on work by others [12, 19-25]. Some of the other properties of Ottawa F-65 sand that are used in the simulations are outlined in Table 3-3.

Table 3-2: Relative density estimates from mass-based and CPT-based measurements in the centrifuge tests and corresponding h_{po} values selected for the numerical simulations.

Test	PM4Sand model calibration parameters (liquefiable layer)			
	Mass-based		CPT-based	
	D_R (%)	h_{po}	D_R (%)	h_{po}
RPI-9	63	0.072	60-65	0.095-0.065
RPI-10	65	0.065	59-64	0.105-0.068
RPI-11	65	0.065	59-64	0.105-0.068
RPI-12	55	0.138	52-58	0.168-0.11
RPI-13	75	0.038	65-70	0.065-0.048
EU-2	65	0.065	57-66	0.122-0.06
KyU-1	55	0.138	-	-
KyU-3	65	0.065	-	-
KAIST-2	65	0.065	63-76	0.072-0.038
UCD-1	70	0.052	74-88	0.038-0.161
ZJU-1	75	0.038	58-81	0.11-0.045

Table 3-3: Properties of Ottawa F-65 sand utilized in the numerical simulations.

Maximum void ratio, e_{max}	0.78[1]
Minimum void ratio, e_{min}	0.51[1]
Specific gravity, G_s	2.65[2]
Permeability, k (cm/s)	0.012[3]

1. e_{max} and e_{min} are based on Carey et al. [26].
2. G_s is based on Vasko et al. [27].
3. k is based on El Ghoraiby et al. [11].

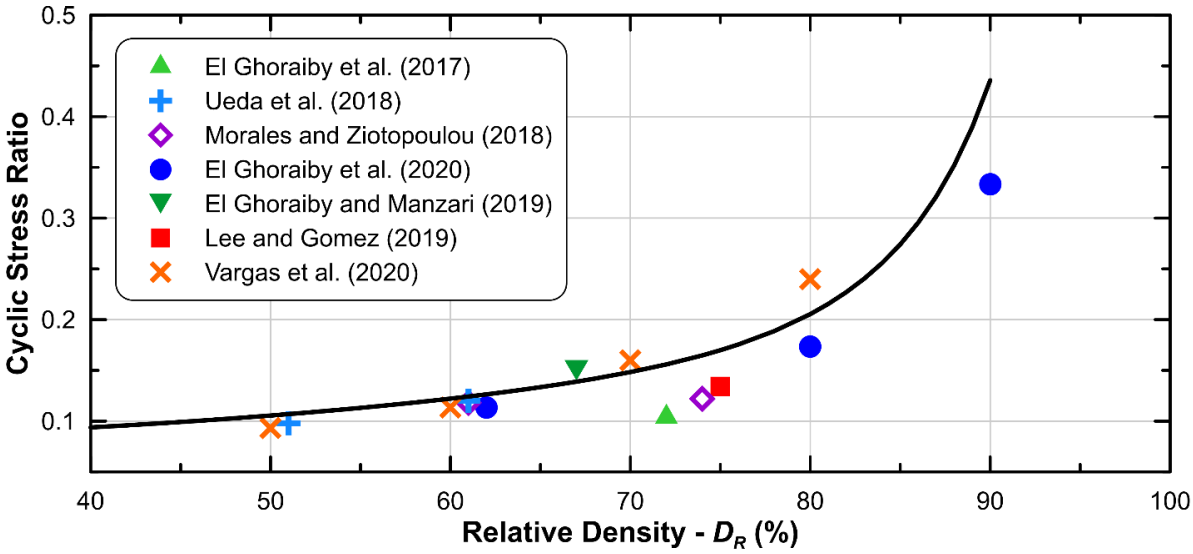

Figure 3-2: Triggering relationship for Ottawa F-65 sand used for calibrating PM4Sand parameters.

3.4.2 INPUT MOTIONS

The centrifuge models are subjected to a horizontal ramped sinusoidal input motion applied at the base of the model that has a peak acceleration of approximately 0.16g. At some of the centrifuge facilities an additional recorded vertical motion component having a peak amplitude about 10 times smaller than the horizontal component is applied at the base. For the numerical simulations the same recorded input motions are applied. Figure 3-3 shows the response spectra and acceleration time histories of the horizontal input motion components used for the centrifuge tests

performed at RPI. The RPI motions have similar peak accelerations and a predominant frequency of 1 Hz except for the RPI-11 motion which has an additional high frequency component of 3 Hz.

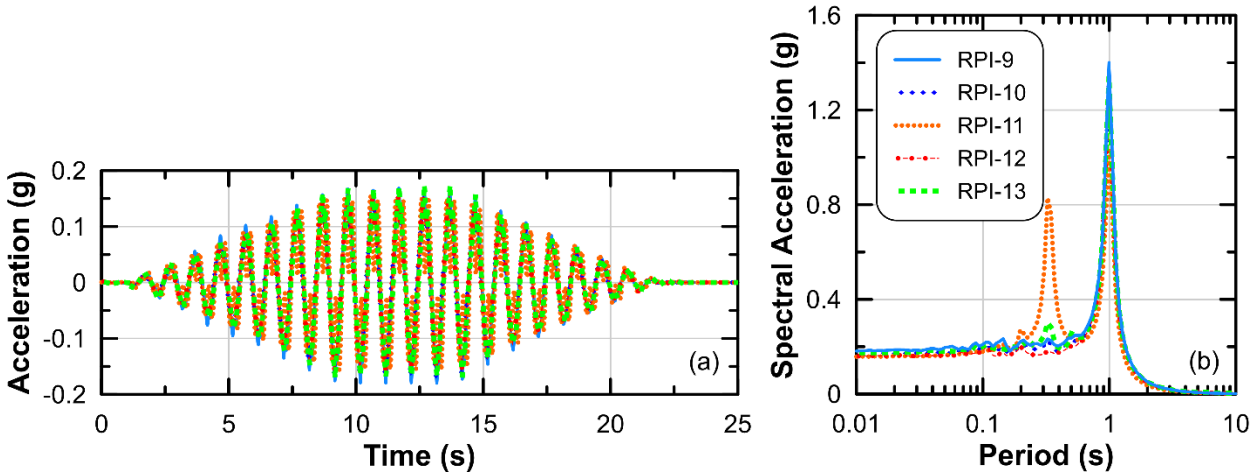

Figure 3-3: Acceleration-time histories and response spectra (5% damped) for horizontal components of the RPI motions.

3.4.3 SIMULATION PROCEDURE AND BOUNDARY CONDITIONS

The numerical simulations performed in this study use square zones having a dimension of 0.5 m. A time-step of 1.0E-5 seconds is used for the analyses presented in this chapter. Analyses repeated with a smaller (one half of the original) mesh size and a smaller time-step (one half of the original) to check the solution stability showed no notable effect on the numerical responses. Large deformations are enabled for all simulations, which allow the mesh nodes to update their coordinates as the model geometry progressively changes. The sheet pile wall is modeled in FLAC using elastic beam elements with nodes at every 0.5 m to match the soil discretization. The properties of the wall had been provided by each centrifuge facility (Table 3-1). The sheet pile is connected to the soil using unbonded interfaces at both sides to simulate the friction between these two materials. The simulations use a soil-wall interface friction of 30° which is equal to the critical

state friction angle of the soil. This value of interface friction is utilized as smaller values results in instabilities within the model. Since the experimental facilities did not provide any data or recommendations on the normal and shear stiffness for the interface, these are selected based on the recommendations provided in the FLAC manual [4].

For each centrifuge test, three simulations are performed at three different relative densities: one corresponding to the D_R measured based on the mass of sand used during pluviation, and two simulations corresponding to the lower and upper bound values of D_R estimated through correlations to CPT measurements in the centrifuges (outlined in Table 3-2). The CPT tests were performed in the centrifuge models prior to shaking and the measured tip resistances between depths of 1 m – 3 m were correlated to D_R using the Bolton and Gui [28] relationship. The correlated values were provided by Prof. Mourad Zeghal from RPI as part of a LEAP workshop. Most of the centrifuge tests showed a non-uniform tip resistance and thus the upper and lower bounds were taken (Table 3-2). The difference between these upper and lower bounds was 5-6% for the RPI tests and as high as 23% as observed for ZJU-1 (Table 3-2). As discussed earlier, due to the uncertainties associated with centrifuge experiments, it is not clear which of these D_R estimates is the most accurate and so all three are used in the simulations.

The mechanical boundary conditions in the simulations are intended to replicate the rigid container used in the centrifuge tests. However, the analyses do not explicitly simulate the rigid box that surrounds the soil. Instead, the constraints it imposes on the geosystem are applied as boundary conditions. All nodes at the bottom of the model are fixed in both the x and y directions while all the side nodes are fixed only in the x direction. The geosystem modeled doesn't allow for rocking of the container to be replicated. Although some of the experiments apply a vertical motion component along with the horizontal motion, significant rocking is not expected to be

produced as the vertical motion amplitudes are 10 times less than the horizontal motion amplitudes for all the tests. Therefore, the inability to numerically model rocking is not expected to have a notable effect in the predictive capability of the simulations.

The reported centrifugal accelerations from each facility are used for the simulations to establish the pre-shaking conditions (static stress initialization phase). To achieve the pre-shaking conditions, the entire soil deposit is constructed in layers followed by excavation of the soil in front of the sheet pile wall. During this static stress initialization phase, a gravity of $1/N_g$ is used to simulate the prototype conditions and the Mohr-Coulomb model with the critical state friction angle and a cohesion of 4 kPa is used for all soil units. This cohesion is necessary to ensure stability at the toe of the wall during initialization but is removed before the dynamic stage. Once the static stresses are established, the water table is applied considering a water elevation of 5 m (backfill surface) based on the centrifuge setup. The presence of water is modeled by applying pressure on the nodes below the water surface. This approach cannot consider the hydrodynamic response of the water, which is a limitation of this study. The appropriate pressure on the top boundary of the toefill area and on the front side of the sheet pile wall is applied to establish submerged conditions. Saturation is set to 100% across the model and equilibrium of pore pressures is established. Porewater flow is allowed along the top surface of the model, whereas flow across the container boundaries is restricted. To allow for free drainage of porewater from the top surface, pore pressures and saturation are fixed at the top nodes. These boundary conditions allowed porewater drainage out of the top boundary of the model, but not along the sides or bottom. Thereafter, gravity is sequentially increased in increments of $1/N_g$ in order to approximate the centrifuge spin-up process, allowing the prototype stresses to establish without arching or other boundary effects. After initial conditions have been established, the nonlinear PM4Sand model is assigned to all soil

units.

Following the static stress initialization, the input earthquake motion is applied to the model. The recorded horizontal acceleration time histories and vertical acceleration time histories (when available) provided by each centrifuge facility are applied at the base of the model. To simulate the effects of the rigid box container the recorded horizontal acceleration time histories are applied to the sides of the model. Rayleigh damping is set to 0.5% at a center frequency of 1 Hz (frequency of input motion). A local damping of 5% is assigned to the wall. This value is slightly higher than the 2-4% range suggested for metal structures by Adams and Askenazi [29]. An additional simulation using a lower value of damping of 1% was performed as a sensitivity and it resulted in a 5% increase in wall displacement from the baseline case. The shaking is continued for the duration of the recorded event for each test (approximately 22 seconds). After the end of shaking, the base of the model is brought to a zero-velocity condition by applying both a horizontal and vertical deceleration to the bottom boundary of the model. These decelerations are opposite in direction to the average velocities along this boundary and the magnitude is calculated to reduce the average velocity to zero in 0.2 seconds. This procedure is meant to approximate the stopping of the centrifuge container and the ramping procedure described herein is used to avoid sudden changes in velocity within the model. After the base of the model is brought to a zero-velocity condition, the model is allowed to reconsolidate under its own weight.

3.5 SIMULATION RESULTS

This section presents the simulated soil and wall responses compared to those from the centrifuge experiments. Response parameters like excess pore pressures, spectral accelerations, surface settlements, and wall displacements are examined. A detailed discussion is presented for the RPI-

9 simulation results. Additionally, the effects of permeability, D_R, and input motion on the responses are investigated. Finally, an overview of the numerical prediction of wall displacements for all 11 centrifuge experiments is presented. The overall range of uncertainty associated with the predictions is examined.

3.5.1 DETAILED RESULTS FOR RPI-9

This section presents the responses of the soil and sheet pile wall obtained from the numerical simulations corresponding to RPI-9. The reported mass-based D_R is used in all the simulations described in this section. Figure 3-4 illustrates the excess pore pressure time histories at different sensor locations within the model. The figure also highlights the excess pore pressure ratio, r_u, which is the ratio of the excess pore pressure to initial vertical effective stress. The simulations capture the general trend of excess pore pressure generation and residual excess pore pressure at sensor PB3 and PM2 (far away from wall) in the backfill reasonably well (Figures 3-4a-b). However, the dilation spikes observed in the experiment at PB3 is not captured in the simulations. This is due to the high frequency acceleration components in the experiment that are not present in the simulation (as shown later in Figure 3-5). The reason behind filtering of high frequency components in the simulation is likely due to the zone size selected in FLAC. However, zones having half the width as those used in the baseline case does not improve the prediction. Simulations using an even smaller zone size may help capture the spikes, but they are not reasonable to perform from the standpoint of computational time. The excess pore pressure build-up at sensor PW1 (close to the wall) in the backfill is not accurately predicted for the tests (Figure 3-4c). This is likely due to the soil-structure interaction effects [30] observed in the centrifuge experiments close to the wall that is not captured adequately in the simulations. Dilation is observed in the dense sand close to the toe of the wall (sensor PD) and in the toefill (sensor PFWB)

in case of simulation (Figures 3-4d-e) unlike the experiment, which shows a contractive response at the same locations. A zone of suction around the toe of the wall has also been observed for the other simulations [31].

The spectral accelerations from the simulation show reasonable agreement with those from the experiment at periods close to the predominant period (1Hz) of the input motion (Figures 3-5a-e). At lower periods, a discrepancy in spectral accelerations between the simulation and experiment is observed. This is due to the high frequency dilation spikes observed in the experiment as opposed to the simulation. The general trends in excess pore pressure build-up and spectral acceleration observed for the RPI-9 simulation is consistent with those from the other simulations [31].

The simulated wall displacement marginally overpredicts the experimental wall displacement (Figure 3-6a) by about 8 cm (10% overprediction). The simulation overpredicts the surface settlement behind the wall by approximately a factor of 2 (Figure 3-6b). The wall displacements for the simulations corresponding to other centrifuge tests both underpredict and overpredict experimental observations, as discussed in section 3.5.4. Both overprediction and underprediction of the surface settlements are also observed for the other tests (as shown in Figure 3-14 and discussed in Basu et al. [31]).

A sensitivity study is performed to account for the effect of mesh size and time step on the responses. The effect of mesh size and time step on excess pore pressure and acceleration responses are negligible. Figure 3-7 shows the wall displacement time histories at the top sensor ($WY-_T$/$WY+_T$) for the baseline simulation corresponding to RPI-9 (mesh size of 0.5 m and time-step of 1.0e-5 seconds), fine mesh (mesh size of 0.25 m) and half-timestep (mesh size of 0.5 m, same as baseline case). The final wall displacements are similar (varying less than 5%) among the three

cases. Considering that there is no basis or data to guide the selection of the wall-soil interface properties, namely the interface friction angle and the interface stiffness, a study is performed with three additional cases of 25% increased interface stiffness, 25% decreased interface stiffness and an increased interface friction angle of 36°. The variation of these interface properties results in a 10% variation in wall displacement at most for all 11 tests (discussed in Basu et al. [31]).

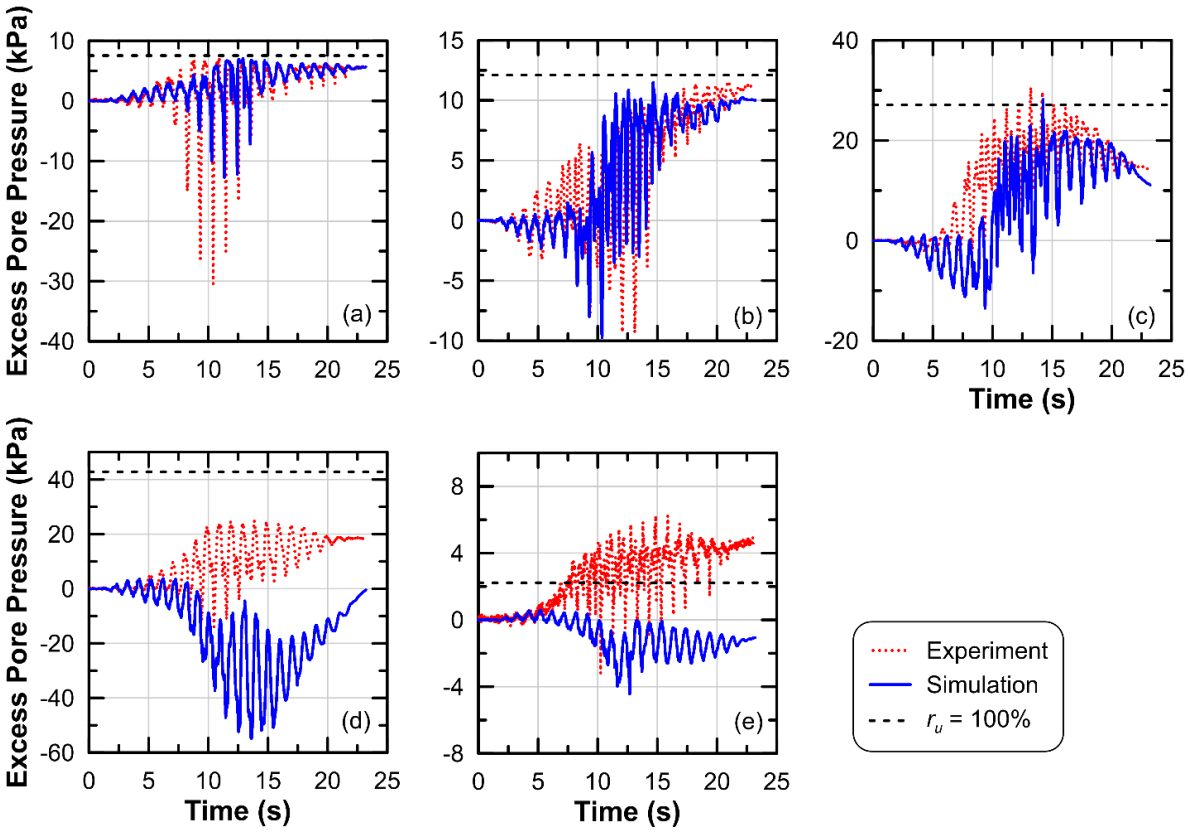

Figure 3-4: Excess pore pressure time histories at the end of dynamic phase for test RPI-9 at sensors: (a) PB3 (b) PM2 (c) PW1 (d) PD (e) PFWB. Dashed lines represent excess pore pressure corresponding to a r_u of 100%.

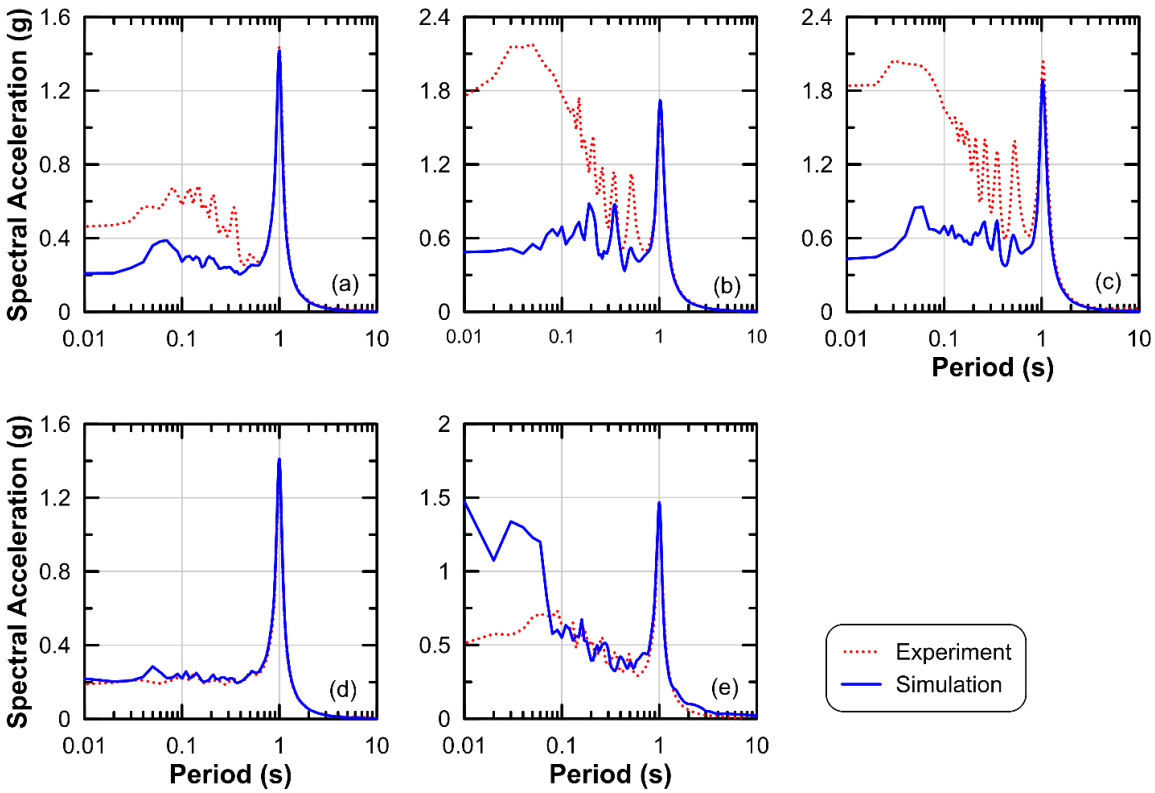

Figure 3-5: Response spectra (5% damped) at the end of dynamic phase for test RPI-9 at sensors: (a) AHB1 (b) AHM2 (c) AHW3 (d) AHD (e) AHFW.

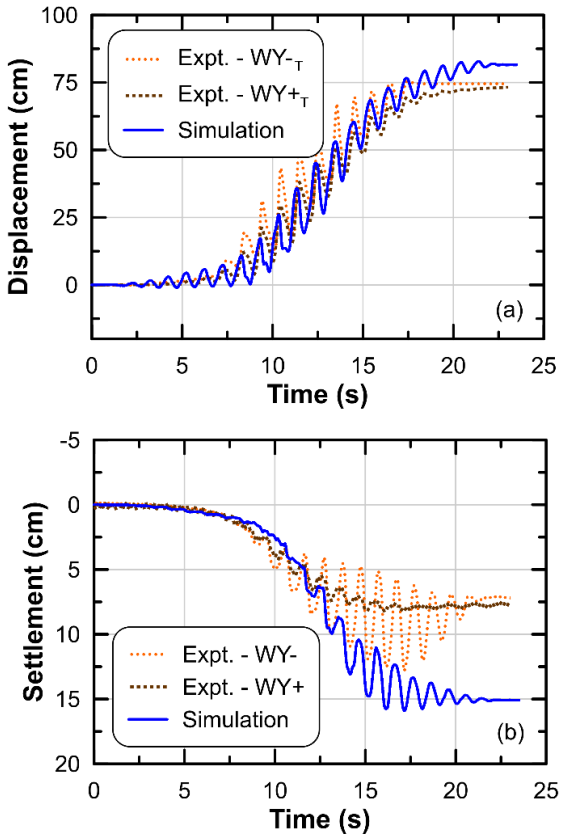

Figure 3-6: (a) Wall displacement and (b) surface settlement time histories at the end of dynamic shaking for RPI-9.

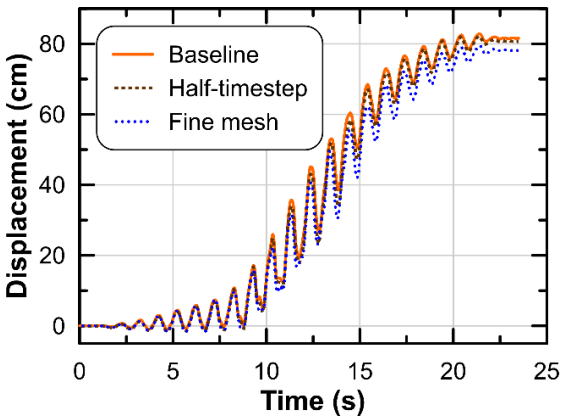

Figure 3-7: Wall displacement time histories at sensor WY-T/WY+T for RPI-9 from the sensitivity analysis using the baseline simulation, simulations with half the baseline timestep and half the baseline mesh size.

3.5.2 EFFECT OF PERMEABILITY

For the simulations discussed in the previous section, a constant permeability (referred to as baseline case in this section) defined for Ottawa F-65 sand [6] is used throughout the duration of the tests. However, in past studies permeability has been observed to increase during onset of liquefaction as soil grains start losing contact with one another and it starts decreasing post-liquefaction during the reconsolidation process [2, 32, 33] as the grain contacts are again re-established. Shahir et al. [33] had observed an increase in permeability by a factor of 20 during liquefaction of Nevada sand. Ueng et al. [34] and Bayoumi et al. [35] had observed a 5-fold and 1.5-fold increase in permeability during centrifuge tests on Vietnam and Ottawa C-109 sands, respectively. Other experimental and numerical studies have also reported an increase in permeability during liquefaction [3, 36, 37]. Contrarily, Adamidis and Madabhushi [38], through centrifuge experiments on Hostun sand, suggested that permeability increases by a factor of 1.2 at the most and such an increase occurs only at effective stresses less than 0.1 kPa. In this study, the excess pore pressure ratio (r_u) dependent permeability relationship (Equation 2) by Shahir et al. [33] is used to simulate the test RPI-9 to investigate the effects of increased permeability during liquefaction.

$$\begin{aligned} k_m/k_i &= 1 && r_u <= 0 \\ &= 1 + (\alpha - 1) \times r_u^{\beta} && r_u <= 1 \\ &= \alpha && r_u > 1 \end{aligned} \tag{2}$$

where k_m is the modified permeability, k_i is the initial permeability at r_u=0, α is the factor by which permeability increases at r_u=1 and β controls the rate at which permeability increases with r_u.

Maximum permeabilities of 5 times and 20 times (at r_u=1) the original baseline value are used in the simulations. The factor of 5 is selected based on findings from simulation of centrifuge experiment on the same sand as discussed in Chapter 2 whereas the factor of 20 is based on the recommendation from the original authors [33]. These two cases will be referred to as HP_1 (maximum permeability 5 times higher than baseline) and HP_2 (maximum permeability 20 times higher than baseline) hereafter. A β value of 1, which has been shown to produce reasonable results by Shahir et al. [33], is used in this study. During shaking, some amount of drainage (therefore, excess pore pressure dissipation) occurs simultaneously along with generation of excess pore pressure [39]. Usually, in the early stages of earthquake loading, when the shaking amplitude is high, the rate of excess pore pressure generation is much higher than dissipation. Therefore, an increase in excess pore pressures is observed. However, this dissipation rate could be much higher as the permeability goes up by an order of magnitude or more. This is observed in case of the simulations using higher permeabilities (Figures 3-8a-b), especially HP_2. Considerable dissipation is observed to occur at the sensor PB3 (far away from the wall) around the end of shaking for HP_2. The overall excess pore pressure generation at sensor PW1 (close to the wall) is lower than the baseline case for HP_1. For HP_2, large dissipation occurs around the end of shaking and the end-of-shaking excess pore pressure is considerably lower than the baseline case. The wall displacements are observed to be less sensitive to variation in permeability. For the permeability case HP_1 the wall displacement is almost the same as the baseline case (4% higher), whereas it decreases by about 15% for HP_2 (Figure 3-9a). The differences in surface settlement behind the wall is negligible among the three cases (Figure 3-9b). The above-mentioned simulation cases highlight that the simulated responses show the best agreement to corresponding experimental observations when increase in permeability is less than 5-fold.

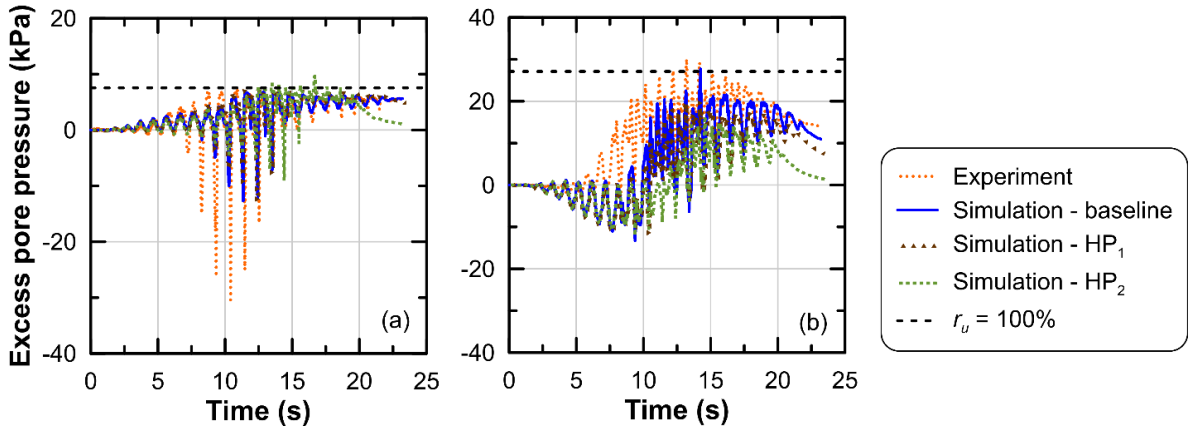

Figure 3-8: Excess pore pressure time histories for different cases of permeability (simulations use mass-based D_R) at sensors (a) PB3 (b) PW1. Dashed lines represent excess pore pressure corresponding to a r_u = 100%.

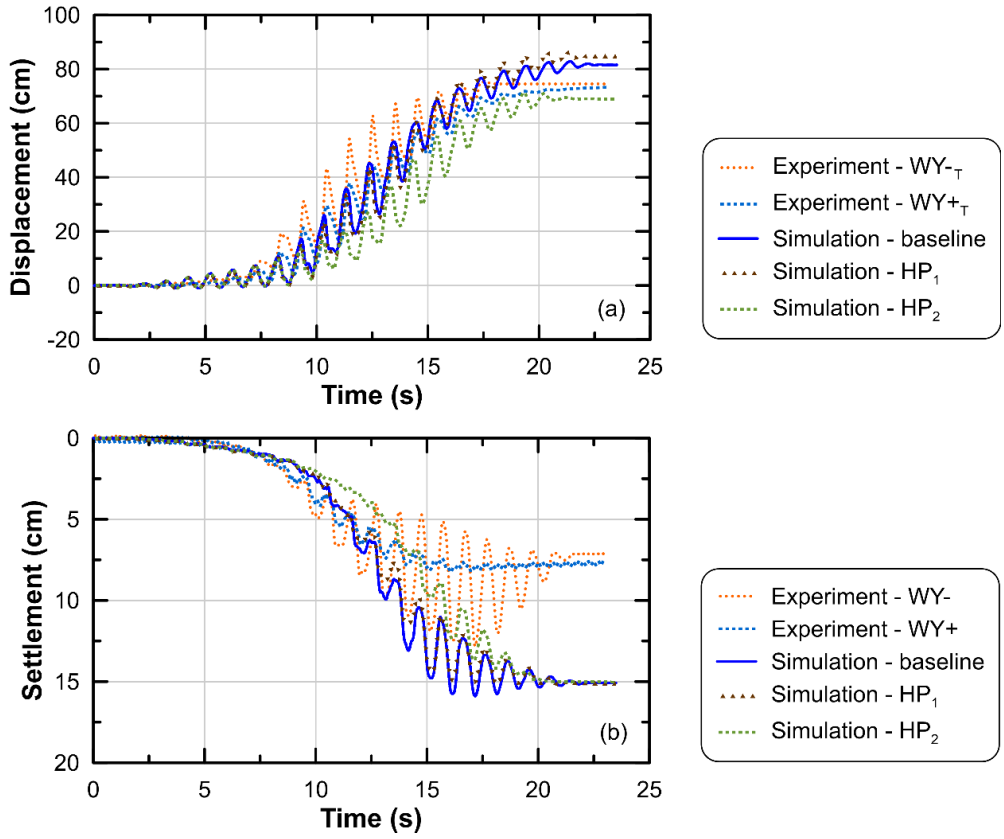

Figure 3-9: (a) Wall displacement and (b) surface settlement time histories for different cases of permeability (simulations use mass-based D_R).

3.5.3 EFFECT OF D_R

The D_R (mass-based or CPT-based) selected for the sand layer is observed to have a major effect on the simulated liquefaction responses for the soil as well as the retaining wall. This is consistent and expected with the overall configuration of the experiment as well as with the constitutive model used, for which D_R is a primary parameter. This section presents a detailed comparison of soil and wall responses between the numerical simulations and centrifuge experiments. The parameters like excess pore pressure, spectral acceleration, surface settlement and wall displacement are examined. Specifically, the RPI tests are selected for the discussion, owing to the similarity in centrifuge set-up and quality control among the different tests.

The excess pore pressure generation is not considerably affected by the relatively small changes in D_R (around 5%) observed in these tests (Figure 3-10) except for RPI-13. For RPI-13, the mass-based D_R value of 75% is considerably higher than the CPT-based D_R range (65-70%). It is observed that the excess pore pressure generation drops considerably as the D_R changes from 70% to 75%, indicating that the simulation is very sensitive to this change. The spectral accelerations are less sensitive to changes in D_R and no clear trend is observed (Figure 3-11).

The variation in wall displacements (Figure 3-12) and surface settlements (Figure 3-13) is much more prominent with changes in D_R. Both wall displacement and surface settlement are inversely proportional to D_R. Typically, the higher the D_R of the liquefiable sand layer is, the lower the wall displacements and surface settlements are. The input motions used for the tests are similar among the RPI tests except for RPI-11, which uses a motion with an additional high frequency component. The displacement prediction for RPI-11 is considerably higher than the experimental value which could likely be due to the high frequency component whose effect is not captured by the simulations.

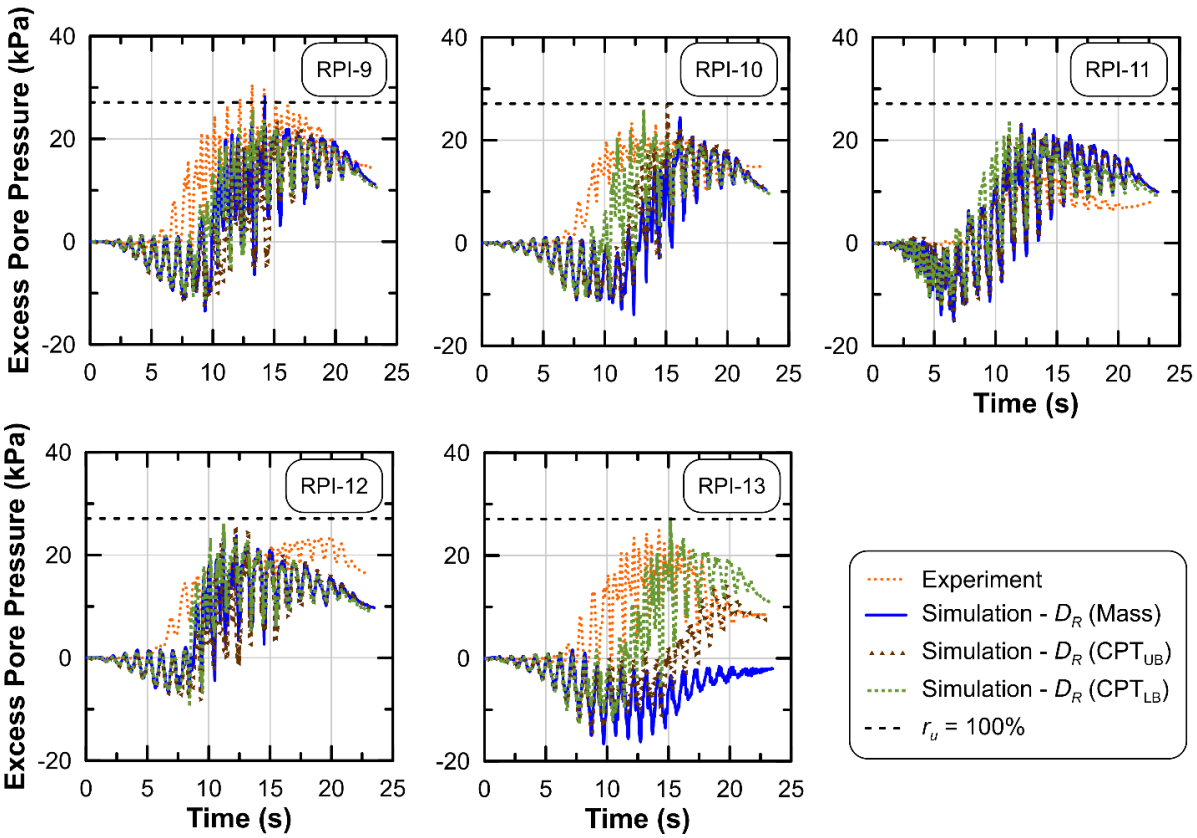

Figure 3-10: Excess pore pressure time histories at sensor PW1 for the five RPI tests. Dashed lines represent excess pore pressure corresponding to a r_u = 1.

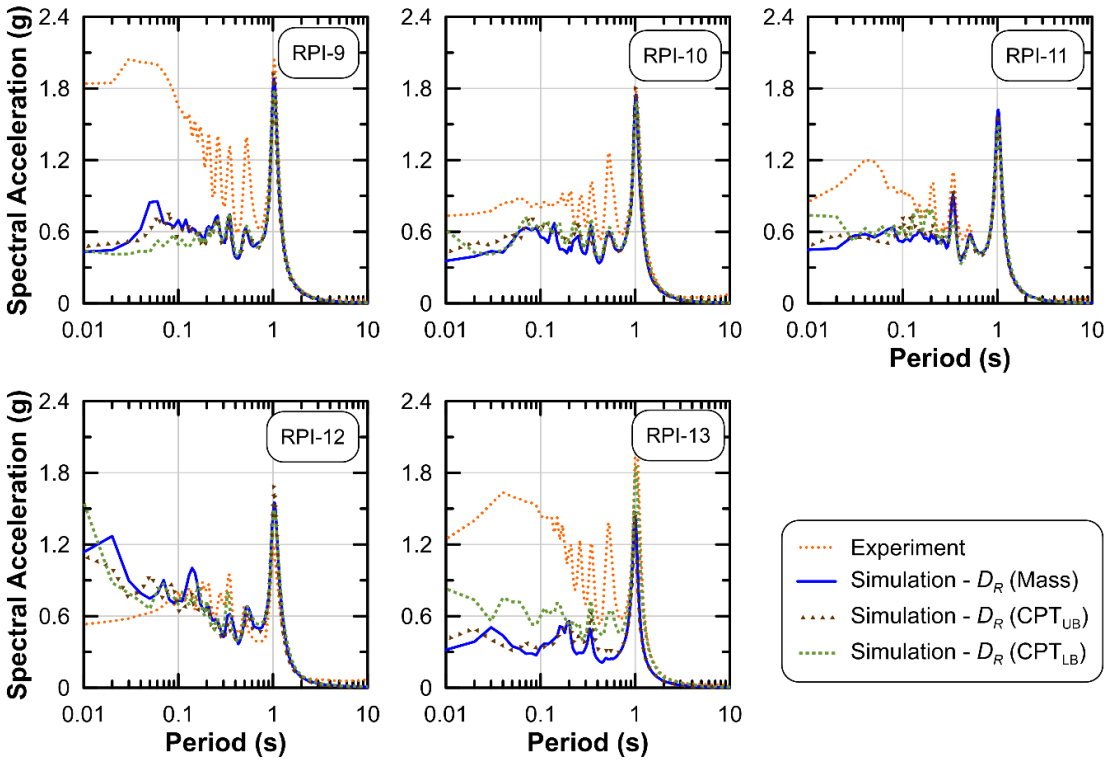

Figure 3-11: Response spectra (5% damped) at sensor AHW3 for the five RPI tests.

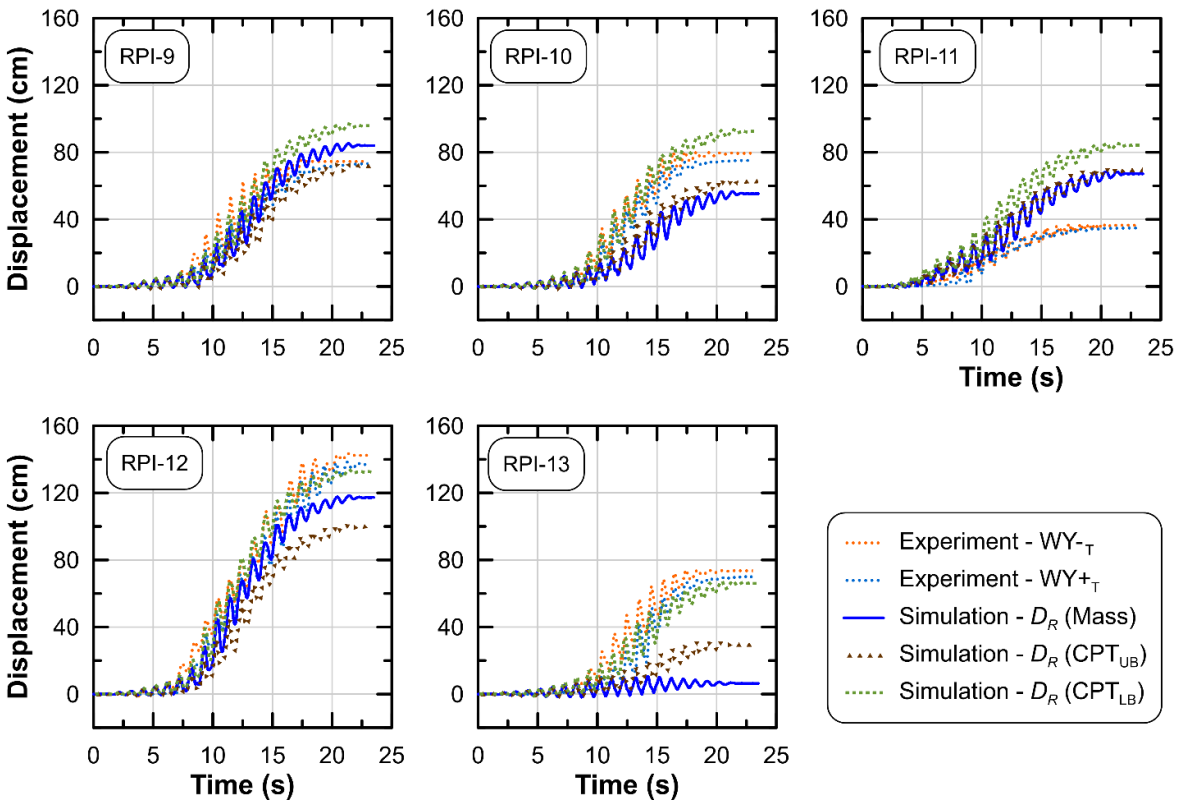

Figure 3-12: Wall displacement time histories at sensor WY_{-T}/WY_{+T} for the five RPI tests.

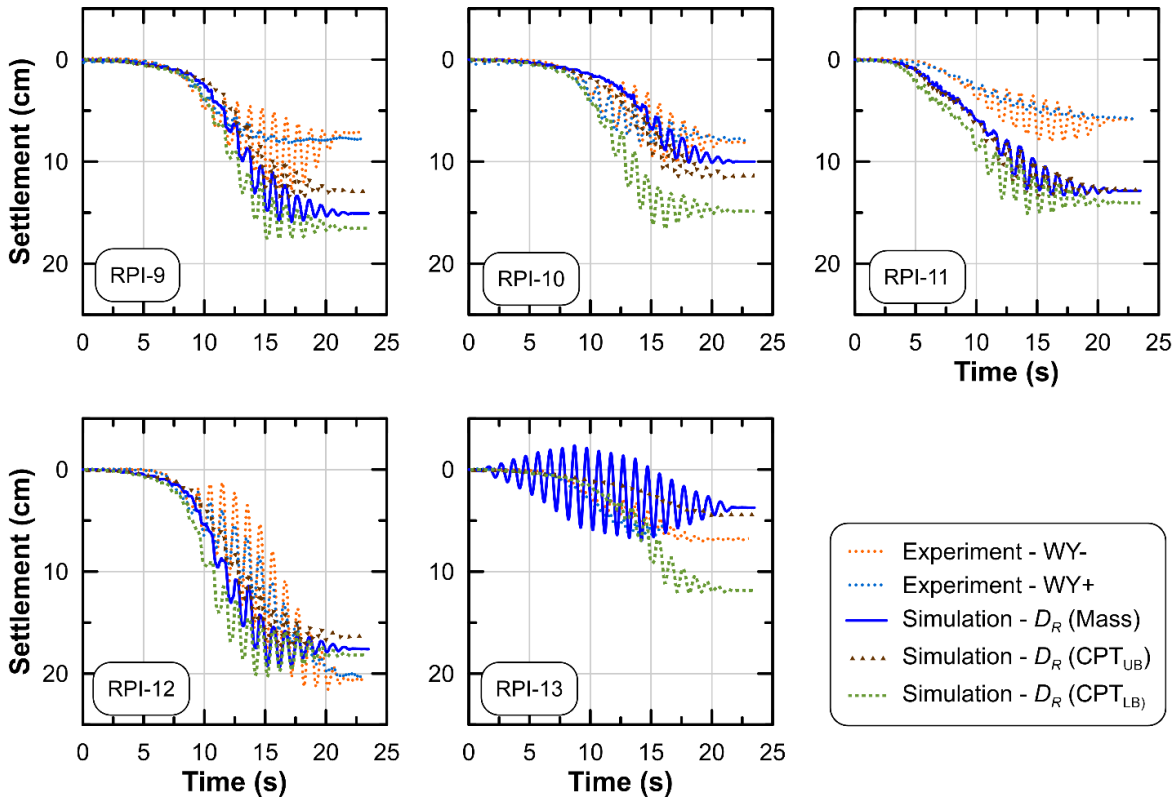

Figure 3-13: Settlement time histories at sensor WY-/WY+ for the five RPI tests.

3.5.4 DISCUSSION ON WALL DISPLACEMENT: NUMERICAL AND CENTRIFUGE COMPARISON

This section presents a detailed comparison between simulated wall displacements and the corresponding values from the 11 centrifuge experiments. Figure 3-14 shows the normalized wall displacements (wall displacement normalized with respect to wall height) from the simulations compared to those from the experiments. The wall displacements are predicted reasonably accurately when using the mass-based D_R for tests RPI-9, ZJU-1, and KyU-1. While considering the CPT-based D_R range in the case of simulations, the predictions of wall displacements improve considerably for tests RPI-10, RPI-12, RPI-13 and EU-2, all of which show marginal to considerable underprediction when using the mass-based D_R. For example, in case of RPI-12 and

RPI-13, the D_R values corresponding to the lower bound of cone tip resistance result in a reasonable estimation of wall displacement. In case of RPI-10 and EU-2, it is observed that a mean CPT-based D_R value from the range prescribed for each test results in a reasonable prediction of wall displacement. In case of RPI-11, the wall displacement is considerably overpredicted at all D_R values possibly due to the high frequency component present in the input motion, which causes a discrepancy between experimental and numerical response. It must be noted that the experimental wall displacement observed in case of RPI-11 is almost half of those observed for tests RPI-9 and RPI-10 even though the relative densities (mass-based D_R and CPT-based D_R range) are similar among the three of them. For tests UCD-1 and KAIST-2, the CPT-based D_R do not improve the prediction of wall displacement. Overall, it is observed that the numerical predictions of wall displacements for all 11 tests are within 50% - 200% of the corresponding experimental displacements, utilizing either the mass-based D_R or a D_R value falling within the range estimated from the CPT correlation. This level of uncertainty is similar to the magnitudes that have been observed for liquefaction-induced free-field settlements in numerical study [40] and in the field such as in Christchurch [41]. Table 3-4 presents several goodness of fit statistics that are estimated. The simulations using the D_R corresponding to the lower bound of CPT show a slightly better R^2 value than the other two simulation cases. These simulations also show a lower mean squared error (MSE) and bias (calculated as the ratio of observed to simulated normalized wall displacement) than the other simulations that use the mass-based D_R or the D_R corresponding to the upper bound of CPT. It must also be taken into consideration that the hydrodynamic pressure of water acting on the wall from its front side in the experiment is not replicated in the numerical simulations. The water sloshing on the face of the wall and the wall movement during shaking could occur both in-

phase and out-of-phase [42] and this could have affected the amount of wall displacement in the experiments.

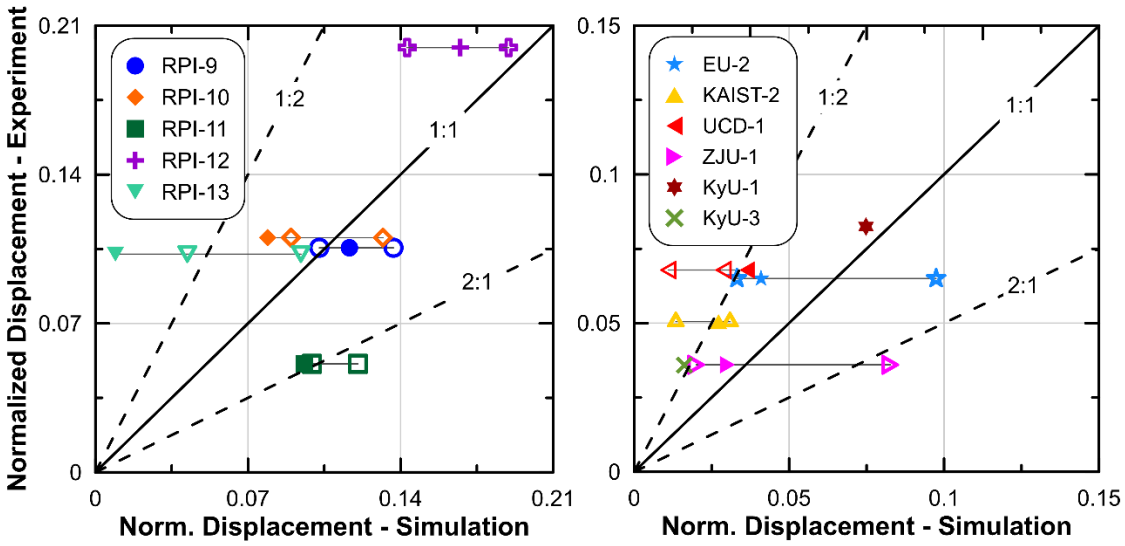

Figure 3-14: Normalized wall displacements at sensor WY_{-T}/WY_{+T} for each of the 11 centrifuge tests (KyU-1 and KyU-3 do not have CPT data). Solid symbols correspond to the mass-based D_R values while hollow symbols correspond to lower and upper bounds of CPT-based D_R.

Table 3-4: Statistical parameters corresponding to the numerical fit of centrifuge-observed wall displacements based on the 11 tests considered in this study.

Parameter	D_R (Mass)	D_R (CPT_{LB})	D_R (CPT_{UB})
R^2	0.569	0.577	0.568
Mean bias	2.278	1.029	2.253
MSE	13.39	1.40	7.77
COV (bias)	1.32	0.60	0.77

For the RPI tests, the dependance between D_R of sand and normalized wall displacement is shown in Figure 3-15. For the numerical simulations, a fairly linear trend between D_R and normalized wall displacement is observed (Figure 3-15a), given that the other model and input motion parameters are similar. It must be noted that the input motions used for the RPI tests have similar peak accelerations and frequency content except for the RPI-11 motion, which has a higher

frequency component in addition to the predominant frequency of 1 Hz. No clear trend between D_R and normalized wall displacement is observed for the experiments (Figure 3-15b). It is interesting to note that RPI-11 and RPI-13 are significant outliers in terms of the observed experimental wall displacement. The deviation from the linear trend, as is observed from the simulations, for RPI-11 is attributed to the higher frequency component in the input motion. However, for RPI-13 the experiment shows a considerably larger displacement (91% larger) as compared to the simulation (utilizing the reported mass-based D_R). This further highlights the uncertainty in mass-based D_R estimation procedure as it is likely that the D_R achieved in this test was much lower than the target value, as was indicated by the CPT measurements for RPI-13. The simulation of RPI-13 test utilizing the D_R corresponding to the lower bound of CPT measurement improves the prediction considerably (8% underprediction) as has been indicated previously.

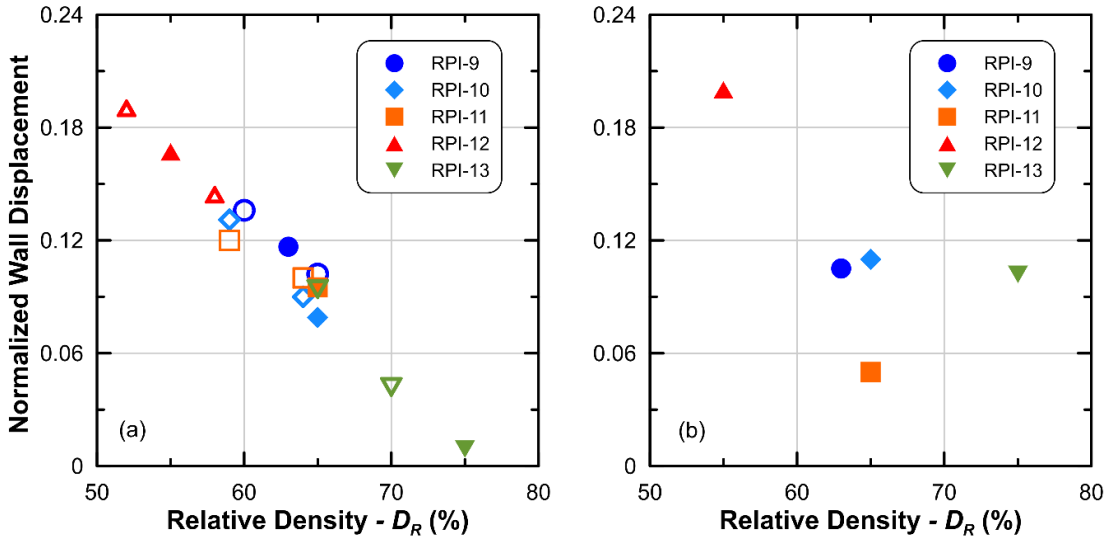

Figure 3-15: Normalized wall displacement vs relative density for (a) simulations and (b) experiments corresponding to RPI tests. Solid symbols correspond to the mass-based D_R values while hollow symbols correspond to lower and upper bounds of CPT-based D_R.

3.6 DISCUSSION AND CONCLUDING REMARKS

This chapter highlights some of the key parameters that affect the liquefaction prediction capability of a numerical model utilizing the numerical platform FLAC and the PM4Sand constitutive relationship. Herein, numerical modeling of centrifuge experiments involving a soil-sheet pile wall system subjected to seismic excitation is studied. A total of 11 centrifuge tests are simulated with the goal of identifying the key soil and wall properties which need to be provided from the experiments to improve the prediction of post-liquefaction responses numerically. The model geometry involves a two-layered stratified deposit having a top layer of loose liquefiable Ottawa F-65 sand overlying a dense Ottawa F-65 sand layer. The soil deposit is retained by a sheet-pile wall. A pseudo-harmonic excitation is applied at the model base. The patterns of simulated wall displacement are investigated, and the findings are compared to experimental observations. Additionally, soil responses such as excess pore pressures, accelerations and settlements are also evaluated. The primary goal of this task is to bridge some of the existing gaps between responses from centrifuge experiments and numerical models.

For centrifuge experiments, the differences in D_R estimates from direct mass-volume measurements and indirect correlations to CPT tests is often observed to be considerable [1]. Moreover, D_R is likely to vary with depth. Therefore, selecting a single representative value of D_R for numerical simulations remains a challenge. It is observed that an accurate estimation of D_R for the liquefiable layer is extremely important in the prediction of responses like wall displacement and ground surface settlement. Increase in wall displacement and ground settlement is observed with a decrease in D_R. Therefore, considering the uncertainty in D_R estimates is important and the prediction of numerical responses is often improved while using the entire range of CPT-based D_R instead of a single representative mass-based D_R value. The most significant improvement in

prediction of wall displacement utilizing a CPT-based D_R is observed for test RPI-13 where the reported mass-based D_R (75%) results in 91% underprediction, whereas the D_R corresponding to the lower bound of CPT measurement improves the prediction (8% underprediction).

Permeability is another key parameter that is observed to have a significant impact on numerical prediction of responses. It has been previously observed that permeability can increase by as much as an order of magnitude during liquefaction [32, 33]. Therefore, it is not often accurate to use a constant value of permeability during liquefaction occurrence in a numerical simulation. Thus, this study examines a r_u-dependent permeability model developed by Shahir et al. [33], capable of increasing permeability by a user-determined factor. The differences in responses, when using constant permeability throughout the test duration versus a r_u-dependent variable permeability relationship, is investigated. Excess pore pressure generation pattern is observed to change drastically when permeability increases by a factor of 20 (at r_u=1) as was suggested by Shahir et al. [33]. Considerable dissipation of excess pore pressure during seismic shaking is observed. Consequently, it also affects the magnitude of simulated wall displacement and ground settlement. However, the best agreement to experimental observations is obtained when permeability is increased at most by a factor of 5 which is consistent with findings on the same sand from Chapter 2. Some of the other important observations from this study are presented below:

- The input motion frequency affects the numerical prediction of responses. The numerical simulation fails to capture the experimental wall displacement accurately when there is an additional high frequency component in the input motion as is the case for RPI-11. The reasons for this are unclear.

- Significant dilation is observed around the base of the sheet pile wall and in front of it in the simulations, unlike the experiments which showed contractive response in the same region. It is possible that the suppressed dilation of the experiments is due to a suspected increased friction on the side walls of the centrifuge container and would likely not be present in a true plane strain problem as the one represented in the numerical simulations. It is also possible that flow conditions or hydrodynamic pressures influenced this response. Moreover, the dense sand layer that was simulated with the reported D_R of 90% might have had a looser configuration in the experiment. Inflow of water from radial direction and movement of sensors from their reported locations during shaking are other events that could have occurred in case of the experiments. These factors could be contributing to the discrepancies observed in the simulated excess pore pressures as some of these might not be possible to replicate in a 2D numerical model.
- A proportional relationship between normalized wall displacement and D_R is observed in the simulations, given that other parameters of the model and input motion are similar.
- The displacements from numerical simulations for all the tests (except RPI-13) fall within a factor of 2 of the experimental displacements.

Overall, from this simulation exercise, it can be concluded that the predictions generally show reasonable agreement for most of the tests when the important soil and wall properties from the experiments are reported. However, the nuances in excess pore pressure generations and wall displacements could be an area to focus on in the future. Some of these could be addressed through better characterization of soil D_R by taking into account the uncertainty associated with the mass-based D_R, considering the uncertainty in correlations utilized to estimate D_R from CPT measurements or by considering spatially variable soil properties for the deposit. Hydrodynamic

forces arising from the water in front of the wall are not considered in the simulations performed herein. This could also be a source of some of the discrepancies in the simulated responses. Additional studies also need to be conducted to verify the effect of high frequency motion components on responses.

CHAPTER 4: NUMERICAL MODELING OF RECONSOLIDATION SETTLEMENTS FOR A SPATIALLY VARIABLE SOIL DEPOSIT

This chapter is based on a paper in preparation by Devdeep Basu, Jack Montgomery and Armin Stuedlein for submission to *Journal of Geotechnical and Geoenvironmental Engineering.*

Basu, D., J. Montgomery, and A. Stuedlein. 2021. "Numerical modeling of reconsolidation settlements for a spatially variable soil deposit." Journal of Geotechnical and Geoenvironmental Engineering (ASCE). Manuscript Under Preparation.

This chapter was altered from the version that will be submitted to *Journal of Geotechnical and Geoenvironmental Engineering* for the purpose of avoiding redundancy and maintaining better flow in this dissertation. My primary contributions to the paper included: (i) evaluating the liquefaction responses with a focus on reconsolidation settlements for a soil deposit with spatially variable properties, (ii) gathering and reviewing literature, (iii) development and design of numerical approach, (iv) processing, analyzing, and interpretation of the results, (v) most of the writing.

4.1 ABSTRACT

Assessment of earthquake-induced liquefaction is an important topic in geotechnical engineering due to the significant potential for damage to infrastructure. Assessments of post-liquefaction deformations is commonly done using empirical models, which often assume laterally homogeneous soil layers. Numerical models offer the potential to examine the effects of spatially variable properties on liquefaction-induced deformations, but this approach is not common in practice. This study explores the predictions of post-liquefaction reconsolidation settlement of a spatially variable site in Hollywood, South Carolina using the numerical platform FLAC and

constitutive model PM4Sand. The effects of motion parameters on reconsolidation settlements and differential settlements are investigated. The physical mechanisms associated with post-liquefaction responses such as excess pore pressures and shear strains are also examined. Correlations between input motion characteristics and reconsolidation settlement are investigated.

4.2 INTRODUCTION

The previous two studies outlined in Chapters 2 and 3 considered laterally uniform sand deposits for numerical assessment of liquefaction-induced responses. However, as discussed in Chapter 1 natural soil deposits are likely to be heterogeneous with the properties varying spatially in both vertical and lateral directions. The effects of spatial variability in soil properties can examined using numerical models [1-4], but this approach is not commonly used in practice due to both the difficulty in modeling liquefaction and measuring spatial variability.

In this chapter, the numerical framework described in the previous two chapters is used to simulate the response of two-dimensional (2D) cross-sections of a well-characterized site in Hollywood, South Carolina, USA. A number of CPT tests, downhole shear wave velocity tests, and mud-rotary borings had previously been performed at the site [5, 6]. This extensive characterization program provided good estimates of fines-corrected cone penetration resistances (q_{c1Ncs}) at the site, which was examined by Bong and Stuedlein [7] to estimate the magnitude of liquefaction-induced reconsolidation settlement that would be expected at the site using empirical models. This chapter will extend the work performed in this previous study by using numerical simulations with the constitutive model PM4Sand v3.1 [8]. The finite difference-based numerical platform FLAC v8.0 [9] is used. Numerical simulations used in this study incorporate spatially variable soil properties such as relative density (D_r) and shear modulus based on correlations to q_{c1Ncs}. Uniform soil profiles, using median and percentile values from the q_{c1Ncs} distribution for the

stochastic deposit, are also simulated to determine their ability in estimating reconsolidation settlements as compared to the stochastic model. This study uses ramped sinusoidal motions having different peak acceleration levels and a suite of recorded transient motions linearly scaled to acceleration intensities of 0.25g and 0.528g that correspond to the expected hazard at the Hollywood site. The effects of input motion parameters like peak acceleration, cumulative absolute velocity (CAV_5) and acceleration spectrum intensity (*ASI*) on the magnitude of simulated reconsolidation settlement and differential settlement are investigated. The necessity of soil-specific calibration of post-liquefaction stiffness to account for the possible bias present in predicted settlements is evaluated. The post-liquefaction responses such as excess pore pressures and shear strains are also examined. Excess pore pressures are observed to vary vertically but not in the lateral direction whereas shear strains mobilized at the end of shaking vary considerably in both directions. Finally, correlations between input motion characteristics and reconsolidation settlements are evaluated.

4.3 DESCRIPTION OF THE HOLLYWOOD TEST SITE

This study focuses on a geotechnical test site in Hollywood, SC. The Hollywood test site was previously used to evaluate liquefaction mitigation using driven displacement piles and controlled blasting techniques [5, 6], pile spacing and installation effects on driving and penetration resistance [10], time-dependent regain of small-strain stiffness [11, 12], spatial variability of silty fines [13], and liquefaction-induced settlements [7]. The site has been extensively characterized using static and seismic CPTs, downhole- and surface wave-based shear wave velocity tests, and mud-rotary borings with split-spoon samples. Figure 4-1 presents a plan view of the test site showing the locations of the CPTs and mud-rotary boreholes.

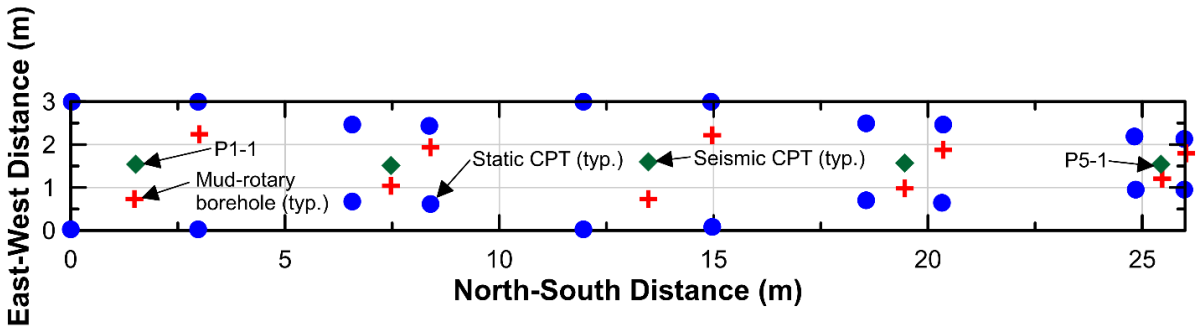

Figure 4-1: Plan view of the Hollywood test site showing the locations of the various explorations performed (modified from Bong and Stuedlein [7]).

The generalized stratigraphy at the Hollywood site is shown in Figure 4-2. The upper 2.5 m is a loose to medium dense silty or clayey sand fill, which overlies a potentially liquefiable layer comprised of loose to medium dense poorly graded sand with lenses of silty sand. This liquefiable layer is the focus of the current study. The liquefiable layer is underlain by a 1.5 m thick, soft to medium stiff clay layer which in turn is underlain by a dense sand layer. The thicknesses of the various layers are generally uniform across the site. The depth to groundwater exhibits seasonal variation and can be as shallow as 2 m below the ground surface.

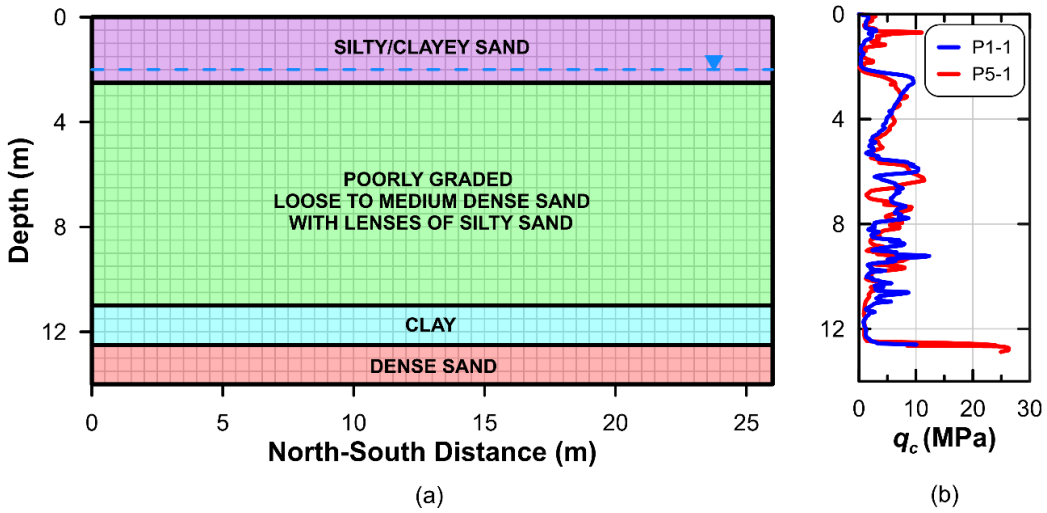

Figure 4-2: (a) Cross-section of the general soil profile at Hollywood site along with the FLAC mesh and (b) cone penetration resistance (q_c) measurements at two locations through CPT tests (based on Stuedlein and Bong [14]).

At the Hollywood test site, Bong and Stuedlein [13] used random field theory [15] to produce a three-dimensional (3D) geostatistical model of the cone penetration resistance (q_c) and fines content within the liquefiable layer at the test site. Subsequently, a 3D geostatistical distribution of q_{c1Ncs} was estimated for this layer [13]. The geostatistical model was discretized at intervals of 5 cm vertically with depth (from 2.5 m to 11 m) and 25 cm in horizontal directions (from 0 m to 3 m in E-W direction and 0 m to 26 m in N-S direction). It resulted in 13 cross-sections of q_{c1Ncs} separated by a distance of 25 cm along the E-W direction. The current study uses a 2D numerical approach, and for each cross-section the original fields were averaged to produce grids with a 50 cm spacing in the vertical direction and a 50 cm spacing in the N-S direction. This averaging was done in order to reduce the number of elements in the simulations and decrease the time required for each computation. Two cross-sections through the 3D model at 1.0 m (E-W direction) and 2.75 m (E-W direction) are shown in Figure 4-3 as an example of the spatial variability in penetration resistance at the site. Figure 4-4 shows the cumulative distribution

function (CDF) of q_{c1Ncs} for all 13 soil sections at Hollywood site. There are only negligible differences in the shape of the CDF among the sections and so the various lines are nearly indistinguishable in Figure 4-4. The CDFs for all 13 sections exhibited a median q_{c1Ncs} value of 80 and a standard deviation of 14.5.

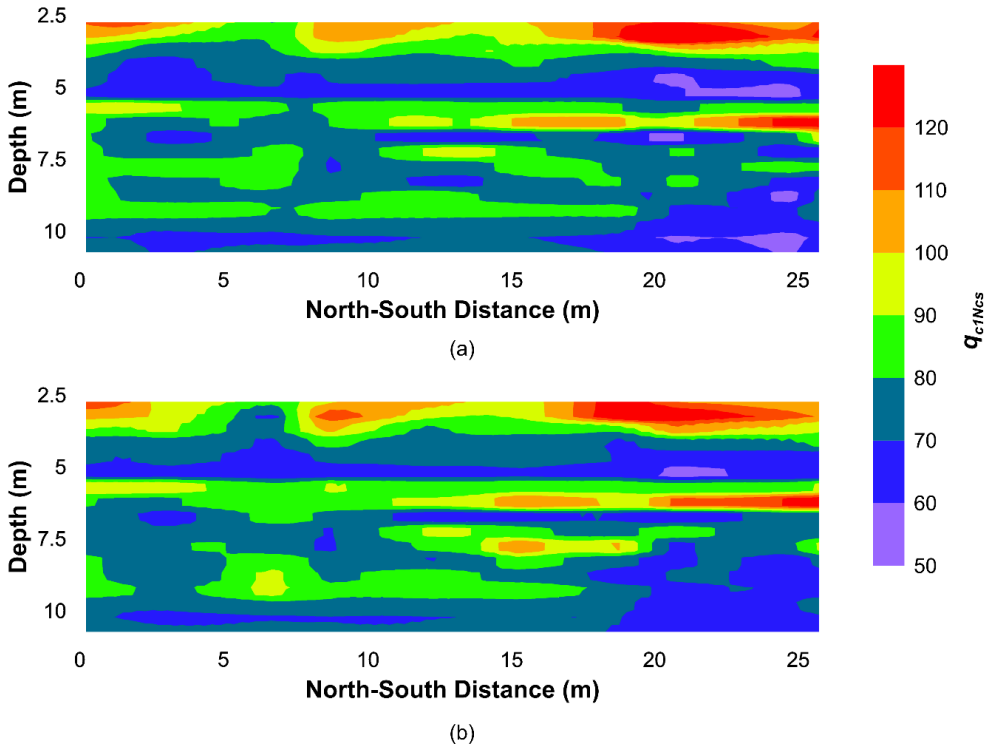

Figure 4-3: q_{c1Ncs} distribution at two sections at distances of 1 m (Section 5) and 2.75 m (Section 12) in the EW direction.

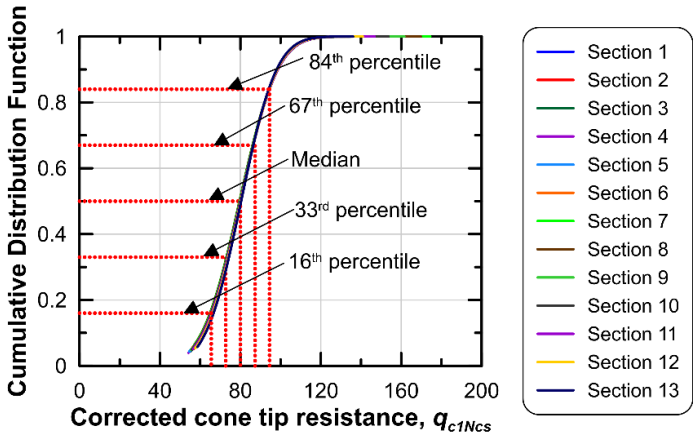

Figure 4-4: Cumulative distribution function of q_{c1Ncs} for each of the 13 sections at Hollywood.

4.4 NUMERICAL MODELING

In this study, numerical simulations were conducted for the 13 soil sections running along the N-S direction (Figure 4-2) and each section had a width of 26 m and a total depth of 14 m. The simulations used the numerical platform FLAC v8.0 [9] and the nonlinear constitutive model PM4Sand v3.1 [8].

The simulations in this study were performed using square elements each having a width of 50 cm. There were three stages in each simulation. In the first stage, the model geometry, soil properties and boundary conditions were defined, and the geostatic stress state (static equilibrium) was achieved. The base of the model was fixed against movement and only vertical movements along the sides of the model were allowed. Hydrostatic pore pressure conditions were established across the model to match the depth of the ground water table which was at a depth of 2 meters from the surface. In the second stage of the analysis, earthquake shaking was applied to the base of the model as a horizontal acceleration time history. During this dynamic stage, the base of the model was fixed against vertical movement and periodic boundary conditions were applied to the nodes on the sides of the model. Drainage could take place from the model top, but the sides of the model were considered no flow boundaries. To mitigate numerical noise, a Rayleigh damping of 0.5% centered at a frequency of 1 Hz was used. The time-step was selected by FLAC to ensure solution stability. Simulations were performed for one of the cross-sections using half of the default time step and mean settlements differed by only 3%. In the final stage, the model was allowed to reconsolidate until all the excess pore pressures generated during shaking had dissipated. This final stage used the same boundary conditions as the static equilibrium stage.

4.4.1 SOIL PROPERTIES AND PM4SAND CALIBRATION

The fill layer, liquefiable layer, and the dense sand layer at the model base were modeled using PM4Sand [8] while the clay layer was modeled using an elasto-plastic Mohr-Coulomb model. The cyclic response is modeled in PM4Sand using three primary parameters which are D_r, shear modulus coefficient (G_o), related to the maximum shear modulus (G_{max}) or shear wave velocity (V_s), and contraction rate parameter (h_{po}). While D_r and G_o are selected based on laboratory or field measurements, h_{po} must be calibrated using single element cyclic direct simple shear (DSS) simulations to obtain the desired cyclic strength. The post-shaking reconsolidation process is difficult to model numerically since stress ratio-based constitutive models exhibit inherent limitations in capturing the reconsolidation strains following liquefaction. This is due to their inability to capture sedimentation effects; thus, the reconsolidation process is typically elastic and produces small volumetric strains [16, 17]. Ziotopoulou and Boulanger [16] proposed an approach to compensate for this limitation by reducing the elastic moduli during the reconsolidation process to increase the volumetric strains. The reconsolidation process in PM4Sand is activated by the user using a flag variable, *PostShake*, which attempts to mimic the sedimentation effects using the elastic moduli reduction approach suggested by Ziotopoulou and Boulanger [16]. The magnitude of the post-shaking volumetric strains is controlled by two parameters, $f_{sed,min}$ and $p_{sed,o}$, which control the magnitude of modulus reduction and the range of mean effective stresses over which the reduction is active, respectively. A D_r-dependent relationship for $f_{sed,min}$ (Equation 1) was developed by Boulanger and Ziotopoulou [8] through calibration to the empirical relationship suggested by Ishihara and Yoshimine [18].

$$f_{sed,min} = A \,.\exp\,(B.D_r) \tag{1}$$

where A and B are constants, whose values were selected as 0.03 and 2.6, respectively, by Boulanger and Ziotopoulou [8]. Boulanger and Ziotopoulou [8] selected a value of 20 kPa for $p_{sed,o}$ noting that volumetric strains were relatively insensitive to increase in $p_{sed,o}$ above 20 kPa. However, as discussed previously in Chapter 2, reconsolidation parameters should be calibrated to specific soil types, whenever relevant soil-specific data are available, to estimate reconsolidation settlements accurately. Therefore, a sensitivity analysis study was conducted by adjusting the default $f_{sed,min}$ relationship suggested by Boulanger and Ziotopoulou [8] to account for the predicted bias in reconsolidation settlement based on the effective grain diameters, D_{10} and D_{50} (as discussed in Chapter 2).

In this study, stochastic properties were used for the liquefiable layer whereas all other layers in the model were assumed to have uniform properties in order to isolate the effects of spatial variability in the liquefiable layer. For the liquefiable layer, the primary parameters were correlated to the q_{c1Ncs} value at each zone. D_r was estimated based on q_{c1Ncs} using the Idriss and Boulanger [19] correlation (Equation 2). G_o was correlated to q_{c1Ncs} through the stress normalized shear wave velocity (V_{s1}) of the soil as shown in Equations 3 and 4. These relationships were developed by adjusting the default PM4Sand correlation between G_o and D_r to better match the average V_{s1} measured at the Hollywood site by Gianella [20] and Mahvelati et al. [11]. h_{po} was calibrated to match the CPT-based cyclic resistance ratio (proposed by Boulanger and Idriss [21]) to reach 3% single amplitude shear strain in 15 cycles ($CSR_{15\ cyc}$) in cyclic DSS test (Figure 4-5). This calibration process was repeated for 45 values of q_{c1Ncs} ranging from 30 to 250, which covers the range of q_{c1Ncs} values in the random fields. Values of h_{po} for intermediate q_{c1Ncs} values were obtained through linear interpolation. An upper limit of 0.8 was put on the triggering curve for very dense soils. The maximum void ratio (e_{max}), minimum void ratio (e_{min}), critical state friction

angle (Φ_{crit}) and hydraulic conductivity (k) were selected based on the recommendations by Gianella [20]. The properties for the other three non-liquefiable layers are outlined in Table 4-1. Most of these properties were provided by Gianella [20] except Φ_{crit}, which was assumed to be 33° for the fill and dense sand layers based on the recommendation by Boulanger and Ziotopoulou [8] for sands.

$$D_r = 0.465 \left(\frac{q_{c1Ncs}}{0.9}\right)^{0.264} - 1.063 \quad (2)$$

$$V_s = 37.895 \, (q_{c1Ncs})^{0.3244} \quad (3)$$

$$G_o = 33.192 \, (q_{c1Ncs})^{0.6487} \quad (4)$$

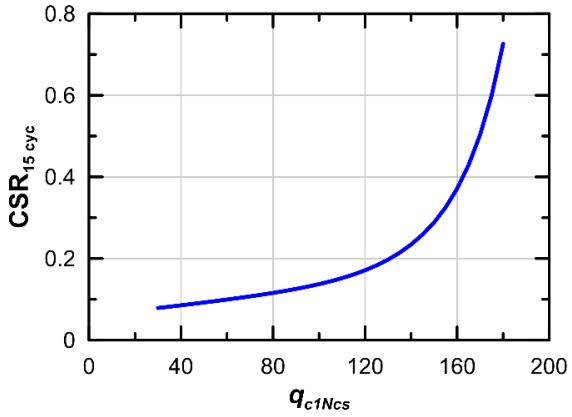

Figure 4-5: Boulanger and Idriss [21] liquefaction triggering curve used for h_{po} calibration. The cyclic stress ratio (CSR) corresponds to 15 cycles of sinusoidal loading in cyclic DSS test.

Table 4-1: Uniform soil properties for the non-liquefiable layers.

Layer	Input properties								
	D_r	Cohesion (kPa)	Φ_{crit} (°)	ρ_d (kg/m^3)	V_{s1} (m/s)	e_{max}	e_{min}	G_s	k (cm/s)
Fill	0.7	-	33	1481	188	1.1	0.65	2.65	0.01
Clay	-	38	0	1500	168	-	-	-	0.0001
Dense sand	0.9	-	33	1550	215	1.1	0.65	2.65	0.01

As discussed in Chapter 2, previous studies [22-24] have suggested that liquefaction causes hydraulic conductivity to increase due to loss of contact between soil grains in its liquefied state. As the liquefied soil reconsolidates, the contacts between grains are re-established and the hydraulic conductivity returns to some magnitude that may or may not reflect its initial fabric. In this study a sensitivity analysis was conducted using the excess pore pressure ratio (r_u) -dependent variable k model developed by Shahir et al. [24] to investigate the effect of variation in k on reconsolidation responses. r_u is defined as the ratio of excess pore pressure to initial vertical effective stress. The hydraulic conductivity relationship for dynamic phase is:

$$\begin{aligned} {k_m}/{k_i} &= 1 && r_u \le 0 \\ &= 1 + (\alpha - 1) \times r_u^{\beta_1} && r_u \le 1 \\ &= \alpha && r_u > 1 \end{aligned} \tag{5}$$

whereas the relationship for reconsolidation phase is given by:

$$\begin{aligned} {k_m}/{k_i} &= 1 && r_u \le 0 \\ &= 1 + (\alpha - 1) \times r_u^{\beta_2} && r_u \le 1 \\ &= \alpha && r_u > 1 \end{aligned} \tag{6}$$

where k_i is the initial hydraulic conductivity at $r_u = 0$, k_m is the modified hydraulic conductivity, α is the factor by which hydraulic conductivity increases at $r_u = 1.0$, and β_1 and β_2 control the rates at which hydraulic conductivity increases with r_u during, and decreases with r_u following, shaking, respectively. Exponents β_1 and β_2 were set to 1 and 2, respectively, whereas an α value of 12 was used for Hollywood sand based on the correlation developed in Chapter 2 to D_{10}.

4.4.2 INPUT MOTIONS

Ramped sinusoidal and transient input motions (Figure 4-6) were used for the simulations in this study. The ramped sinusoidal motions had peak accelerations of 0.05g, 0.13g, 0.25g, 0.32g, 0.4g, 0.6g and each of these pseudo-harmonic records had a duration of 15 s and a frequency of 1 Hz. Seven transient motions were chosen from the suite of motions recommended by Jayaram et al. [25] to approximate a strike-slip event with a moment magnitude (M_w) of 7 at distance of 10 km. This event is an approximate representation of the M_w and closest distance to rupture plane (r_{rup}) combination for the most probable earthquake events expected at the Hollywood site that correspond to return periods of 475 years and 975 years [26]. These return periods correspond to the maximum credible earthquake events at the site. Moreover, the most severe earthquake recorded in the vicinity of Hollywood area (the 1886 Charleston earthquake [27]) also corresponded to a M_w of 7 and it had an epicentral distance of 30 km from Hollywood. These seven motions that were selected were recorded at rock sites and have a range of spectral shapes as shown in Figure 4-7. Each of these motions were linearly scaled to produce two different peak accelerations of 0.25g and 0.528g that correspond to probability of exceedances of 5% (475 years return period) and 2% (975 years return period) in 50 years. Table 4-2 lists some of the important characteristics of the selected transient records.

Table 4-2: Characteristics of recorded earthquake motions considered in this study.

Earthquake Motion	**Recording Station**	**Year**	M_w	**Duration (s)**	**Predominant period (s)**	CAV_5 **(m/s)**[1]		ASI **(m-s)**[2]	
						Peak acc. = 0.25g	**Peak acc. = 0.528g**	**Peak acc. = 0.25g**	**Peak acc. = 0.528g**
M1 - Imperial Valley-06	Cerro Prieto	1979	6.53	63.7	0.3	25.52	53.91	2.71	5.73
M2 - Duzce, Turkey	Lamont 531	1999	7.14	41.5	0.26	9.41	19.89	2.48	5.25
M3 - Taiwan SMART1(45)	SMART1 E02	1986	7.30	32.9	0.2	10.19	21.54	2.56	5.42
M4 - Helena, Montana-01	Carroll College	1935	6.00	40.0	0.14	2.08	4.41	1.56	3.3
M5 - Victoria, Mexico	Cerro Prieto	1980	6.33	24.4	0.06	3.87	8.18	1.52	3.21
M6 - Duzce, Turkey	Mudurnu	1999	7.14	28.83	0.3	8.49	17.94	2.53	5.34
M7 - Sitka, Alaska	Sitka Observatory	1972	7.68	55.0	0.12	10.57	22.33	1.89	3.99

1. CAV_5 is the cumulative absolute velocity corresponding to input acceleration amplitudes greater than 5 cm/s^2 [28].
2. *ASI* corresponds to acceleration spectrum intensity.

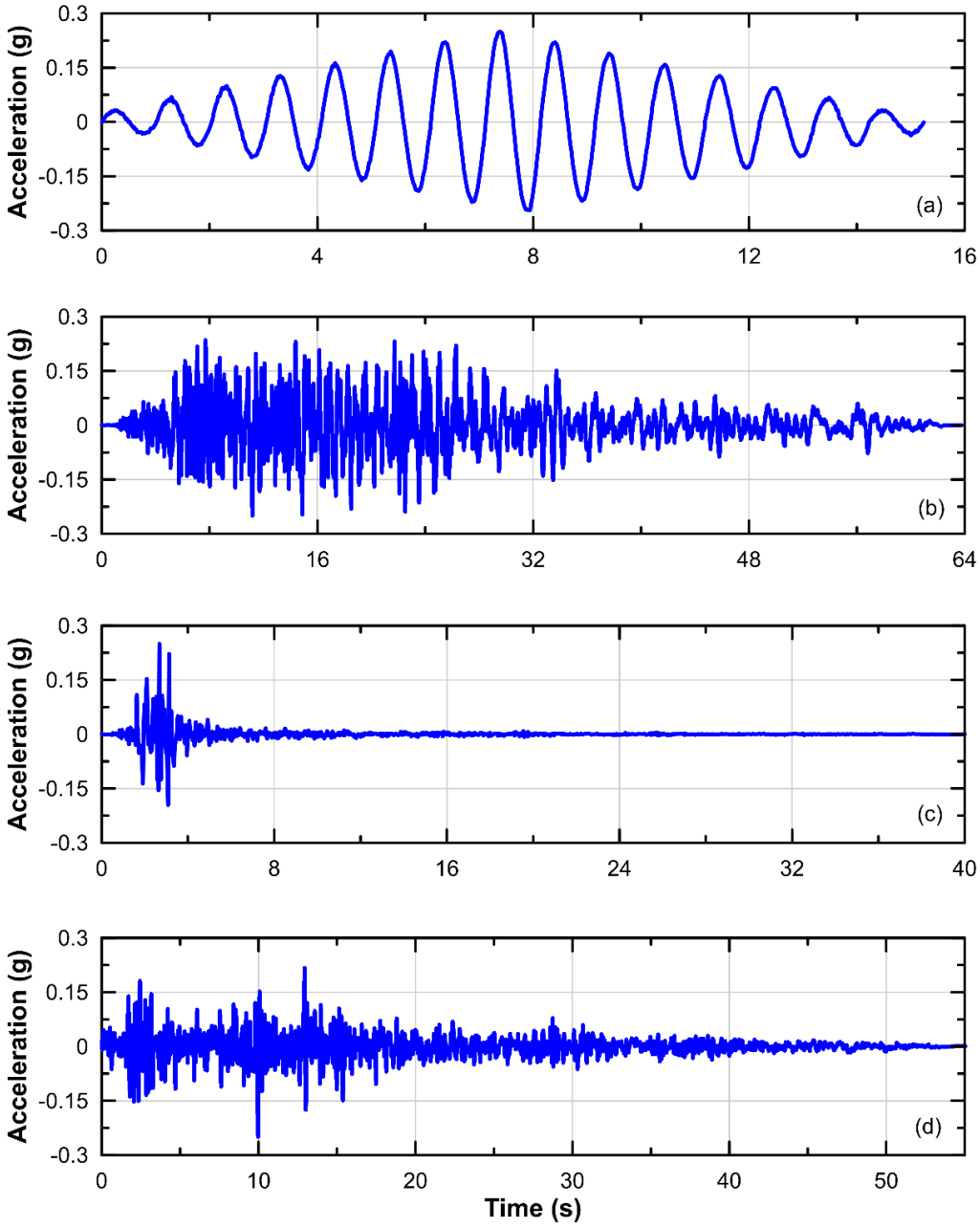

Figure 4-6: Some typical input motions used in this study: (a) a ramped sinusoidal input motion with a peak acceleration of 0.25g and three linearly-scaled transient motions: (b) M1 - Imperial Valley-06 (M1) (c) M4 - Helena, Montana-01(d) M7 – Sitka, Alaska.

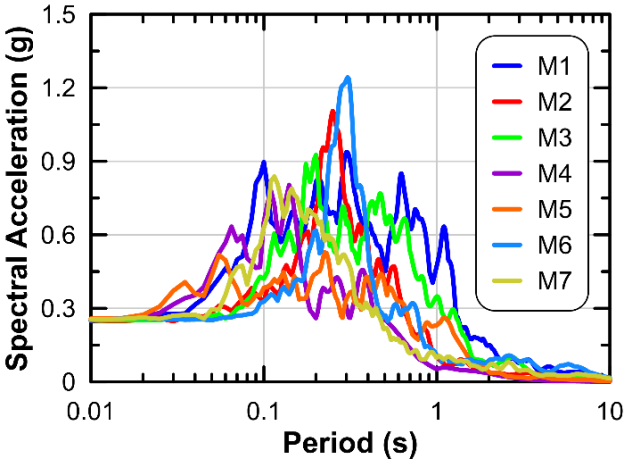

Figure 4-7: Response spectra for the transient motions used in this study scaled to a peak acceleration of 0.25g.

4.5 RESULTS

Numerical simulations were performed in FLAC for the 13 stochastic soil sections considered in this study using both ramped sinusoidal motions and transient motions. Additionally, simulations were performed for five representative uniform soil sections having q_{c1Ncs} values equal to the median (80), 16th percentile (65.5), 33rd percentile (72.7), 67th percentile (87.3) and 84th percentile (94.5) as obtained from the CDF for the stochastic sections. Ramped sinusoidal input motions were used for these uniform sections. Simulations of both stochastic and uniform models performed using half of the default time-step and a half mesh size (25 cm elements) resulted in differences of less than 3% for settlements. A sensitivity study was performed to assess the effect of using a r_u – dependent variable permeability function on reconsolidation settlement and to investigate the necessity of modifying the default PM4Sand reconsolidation parameters to remove any bias in settlement predictions. All the other simulations described in this study used a constant k and the default PM4Sand reconsolidation parameters.

4.5.1 EXCESS PORE PRESSURE RESPONSE

Figure 4-8 highlights the excess pore pressure time histories observed at different depths within the stochastic model using ramped sinusoidal motions. End of shaking excess pore pressures at any depth did not vary laterally even though q_{c1Ncs} varied in the lateral direction (Figure 4-9). This can be further verified through the overlapping excess pore pressure histories observed at four adjacent zones within the model where q_{c1Ncs} varied between 68 – 95 (Figure 4-10).

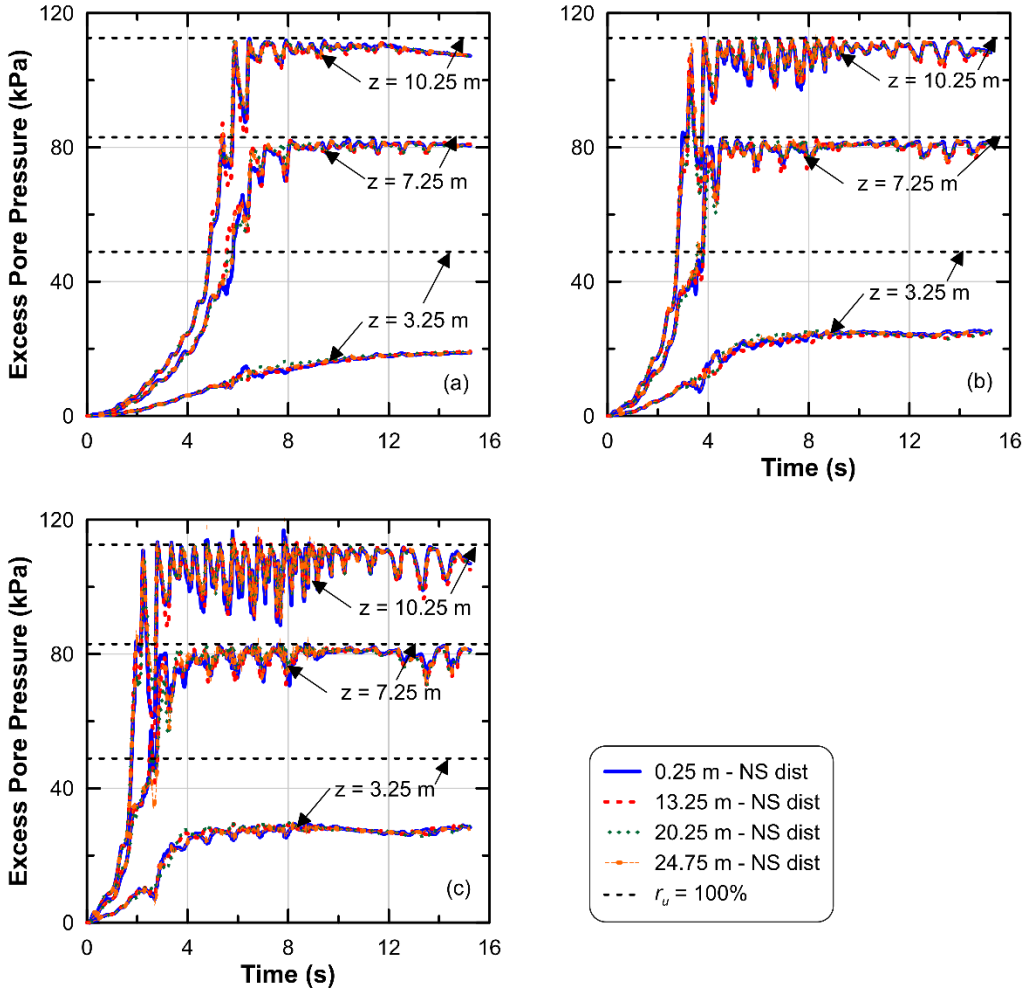

Figure 4-8: Excess pore pressure time histories for the stochastic section 12 (2.75 m in EW direction) under ramped sinusoidal motions at three different peak accelerations of (a) 0.13g (b) 0.25g (c) 0.4g. The dashed black lines correspond to a r_u of 1 at the three depths.

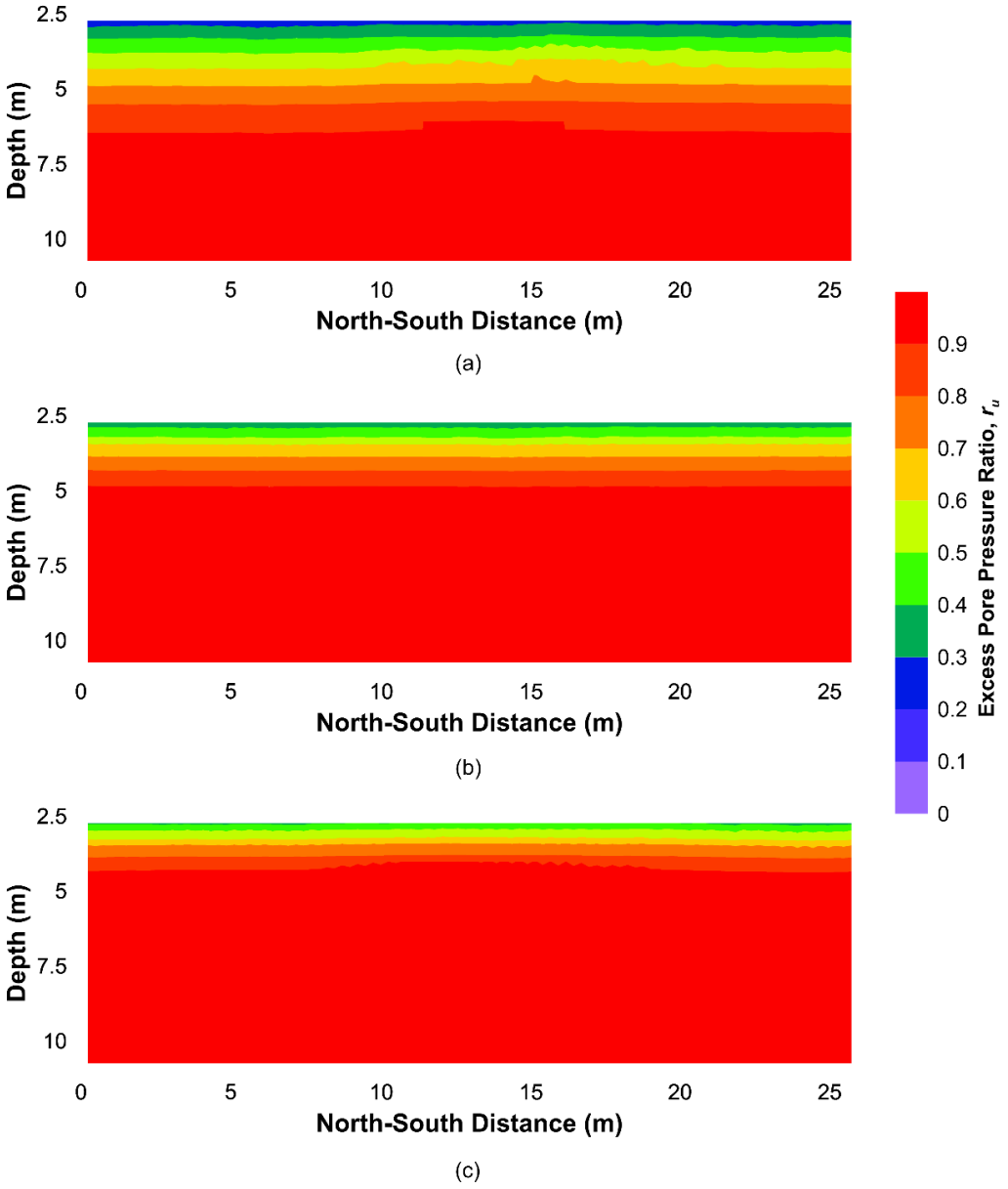

Figure 4-9: r_u distribution in stochastic section 12 at the end of shaking using the ramped sinusoidal motions at peak accelerations of (a) 0.13g (b) 0.25g and (c) 0.4g.

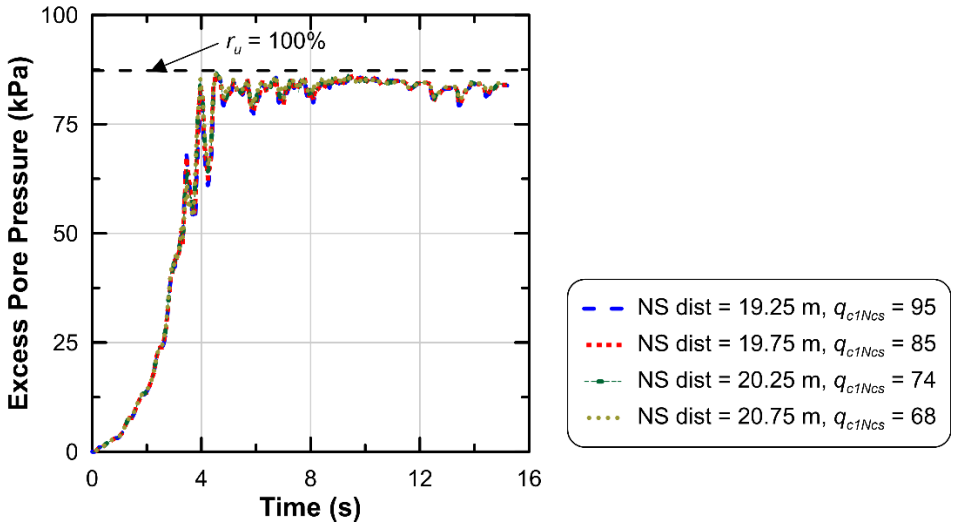

Figure 4-10: Excess pore pressure time histories at a depth of 7.75 m within the stochastic section 12 using ramped sinusoidal motion having a peak acceleration of 0.25g. The dashed black line corresponds to a r_u of 1.

In case of the simulations subjected to transient motions, the excess pore pressures also exhibited no lateral variation as observed from the r_u distribution in section 12 (Figures 4-11 and 4-12). Figures 4-13 and 4-14 outline the excess pore pressure time histories during shaking for the seven transient motions having peak acceleration levels of 0.25g and 0.528g, respectively. The excess pore pressures were recorded in a soil column at the center of the section (13.25 m NS distance) at depths of 3.25 m, 7.25 m and 10.75 m within the liquefiable layer. The r_u value of 1 corresponding to each depth is highlighted in the plots. A r_u of 100%, corresponding to a zero effective stress condition, commonly referred to as initial liquefaction, is often defined as the criterion that governs the onset of liquefaction [29]. However, it must be noted that as suggested by Ishihara [30], liquefaction can occur at r_u values less than 1, such as in silty sands or sandy silts where r_u values often level out at 0.9-0.95. Moreover, a r_u value of 1 is not achieved in various other situations such as in dense clean sands and/or for sloping ground conditions [31]. No liquefaction was observed in the upper half of the liquefiable layer using any of the transient

motions at the two selected acceleration intensities. For the acceleration level of 0.25g, the motions M1, M2, M3 and M6 resulted in close to initial liquefaction conditions within a depth of 7-11 m in the liquefiable layer (Figure 4-13). In case of the acceleration intensity of 0.528g, initial liquefaction was observed within 7-11 m depth in the liquefiable layer in case of all the transient motions except M4 (Figure 4-14). This is likely due to the fact that M4 had the smallest CAV_5 value among all the seven motions (Table 4-2).

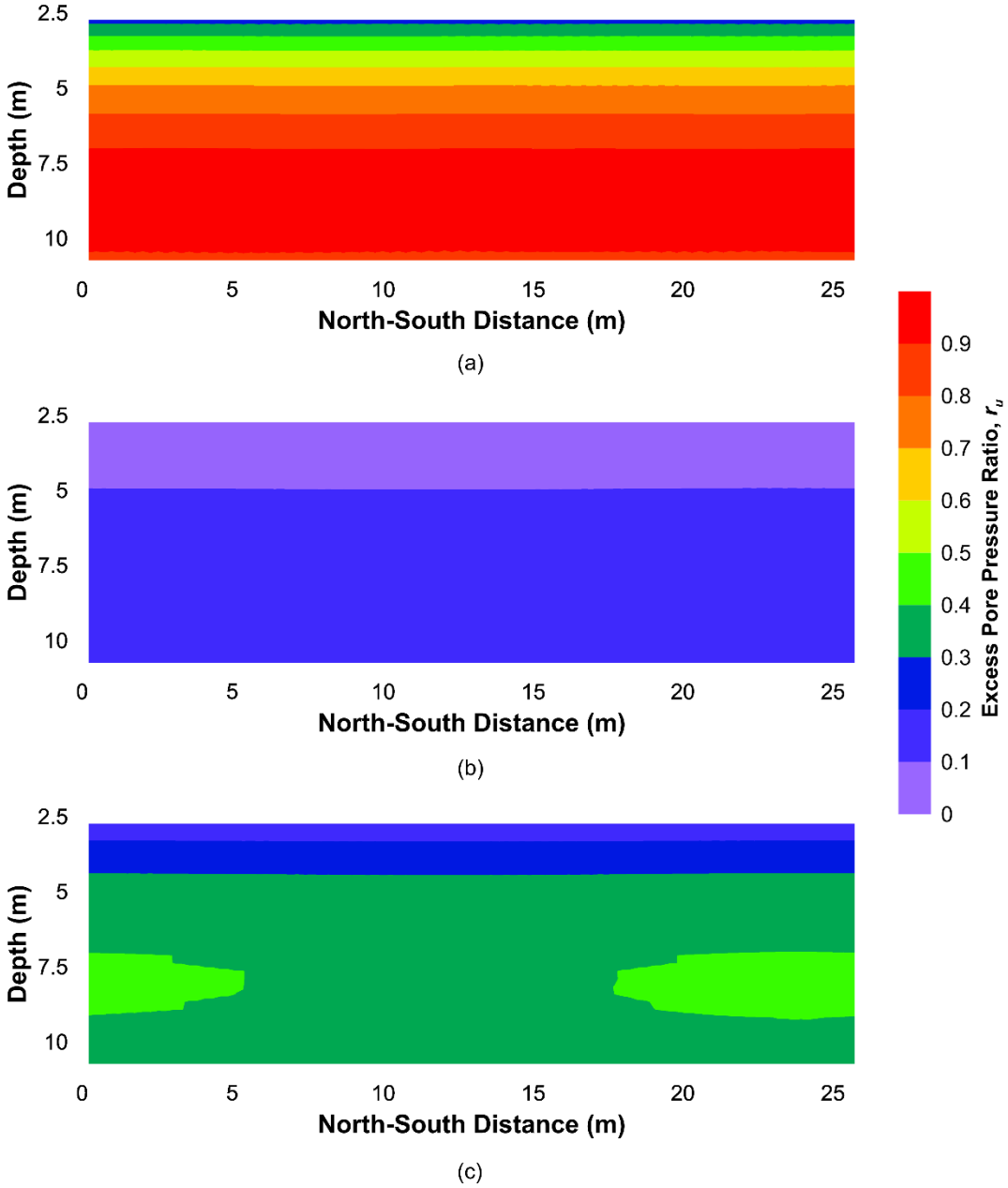

Figure 4-11: r_u distribution in stochastic section 12 at the end of shaking using the motions (a) M1 (b) M4 and (c) M7. All motions correspond to an acceleration level of 0.25g.

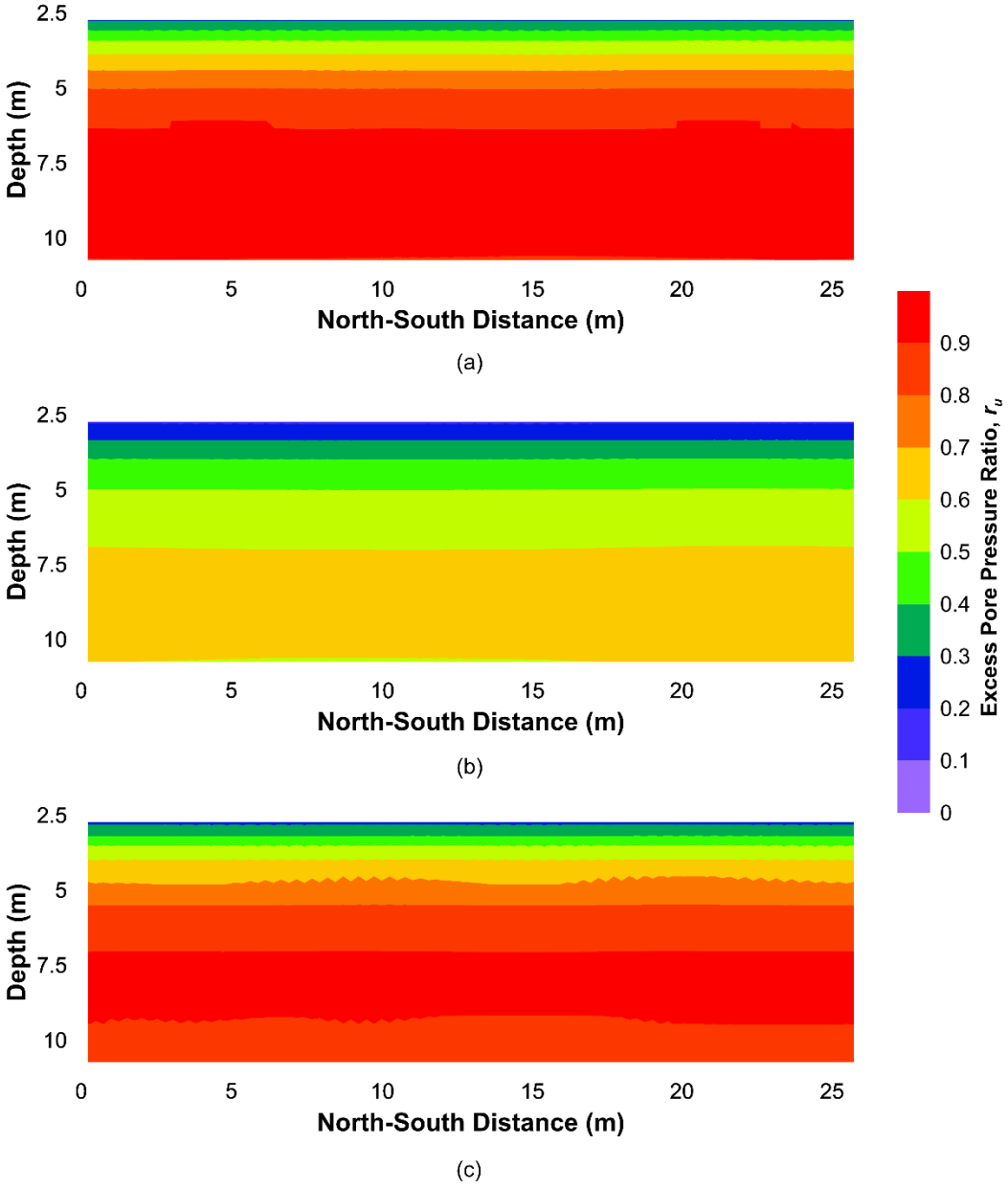

Figure 4-12: r_u distribution in stochastic section 12 at the end of shaking using the motions (a) M1 (b) M4 and (c) M7. All motions correspond to an acceleration level of 0.528g.

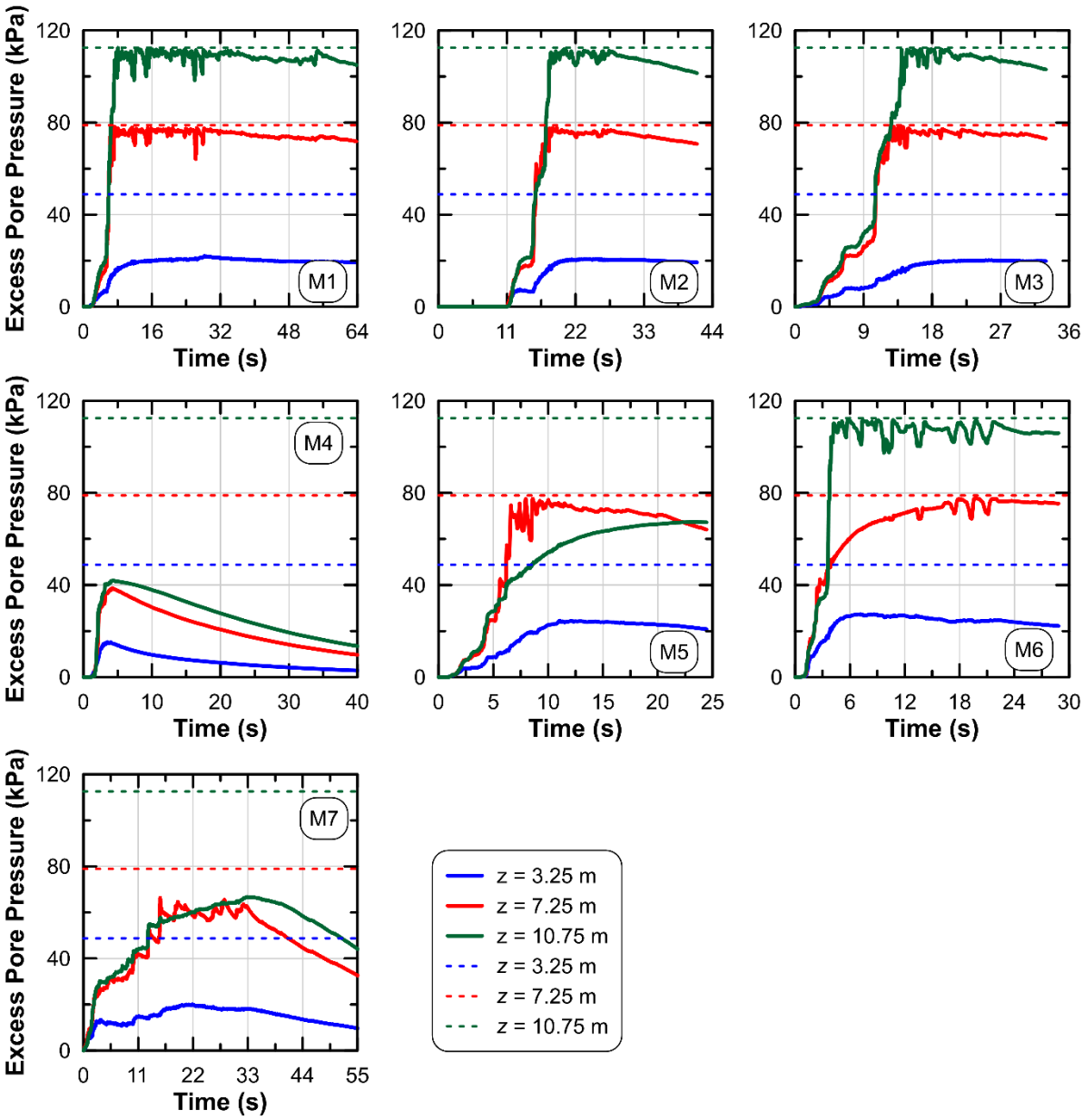

Figure 4-13: Simulated end-of-shaking excess pore pressure histories at different depths within the liquefiable layer in section 12 (at 2.75 m in E-W direction) of the stochastic model using the 0.25g peak acceleration transient motions. The solid lines correspond to the excess pore pressure histories and dashed lines correspond to a r_u of 1.

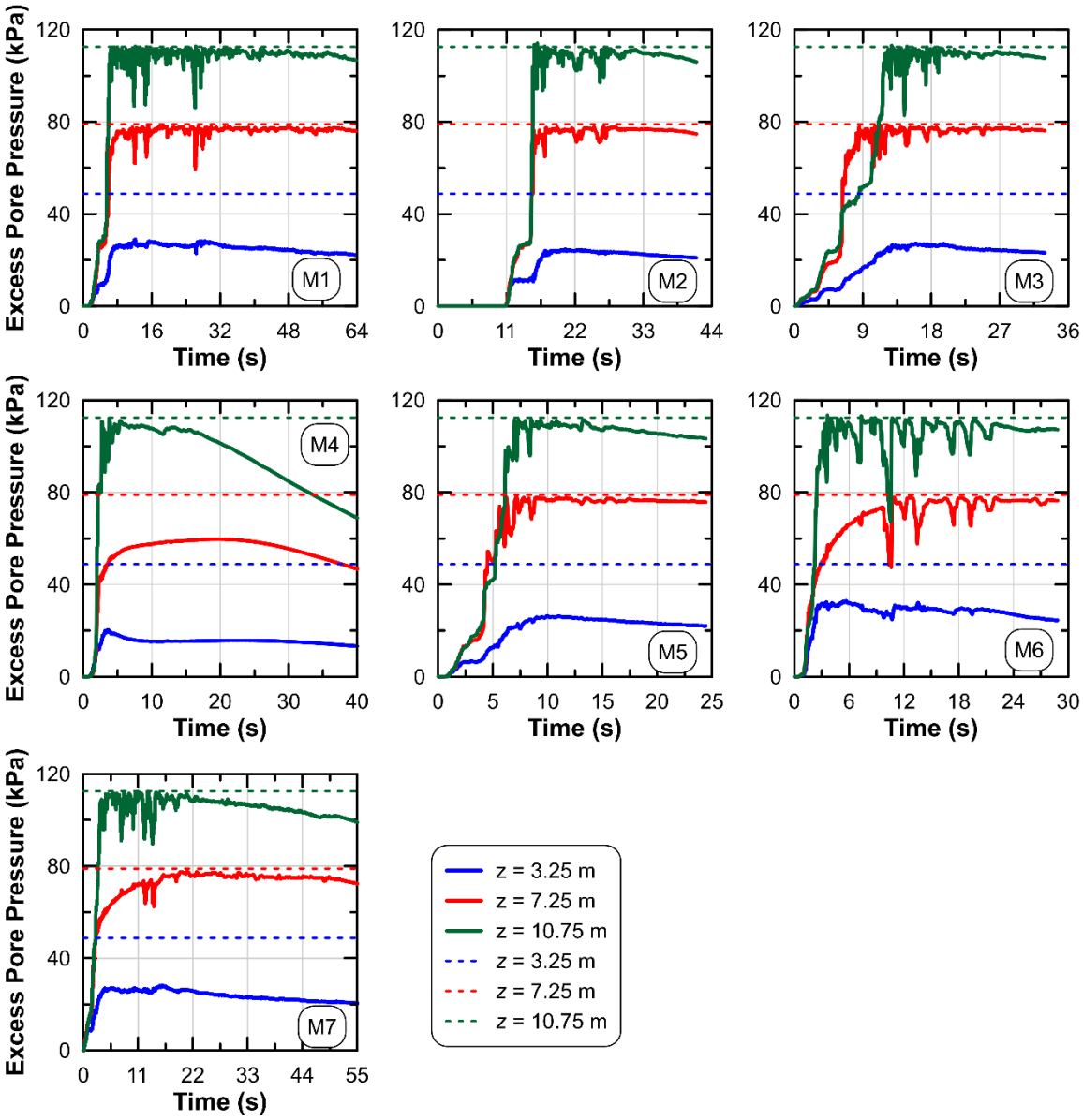

Figure 4-14: Simulated end-of-shaking excess pore pressure histories at different depths within the liquefiable layer in section 12 (at 2.75 m in E-W direction) of the stochastic model using the 0.528g peak acceleration transient motions. The solid lines correspond to the excess pore pressure histories and dashed lines correspond to a r_u of 1.

4.5.2 SHEAR STRAIN RESPONSE

The end-of-shaking shear strain distribution within the liquefiable layer of stochastic soil section 12 is shown in Figures 4-15, 4-16 and 4-17. In case of the ramped sinusoidal motions, shear strain

localization was observed in a narrow band at the bottom of the liquefiable layer at peak acceleration intensity of 0.25g and larger (Figure 4-15). The bottom of the model had a concentration of lower q_{c1Ncs} values (Figure 4-3b) and a r_u of approximately 100% after approximately three seconds of shaking for the most intense motions (Figure 4-8). Once this zone liquefied, the reduction in stiffness led to damping of the seismic energy and a reduction in the loading on the shallower zones. For the least intense motion (0.13 g), it takes several additional cycles to reach a r_u of approximately 100% and the shear strains are more evenly distributed across the various depths. This can also be seen in Figure 4-18, which shows the shear strain in various rows of zones plotted against the q_{c1Ncs} of that zone. For all three motions, there is a general trend of increasing shear strain with decreasing q_{c1Ncs}, but for the most intense motions the shear strain magnitude within the lower layers is considerably higher.

In case of the transient motions, shear strains were not limited to narrow bands but were generally distributed within a depth of 5-11 m in the liquefiable layer (Figures 4-16 and 4-17). At a peak acceleration of 0.25g, only M1 triggered considerable liquefaction (Figure 4-13) and for this motion shear strains can be seen concentrating within a few localized zones (Figure 4-16a). This pattern of shear strain is similar to that observed by Montgomery and Boulanger [2] for gently sloping ground where shear strains were observed to localize in a path of interconnected weaker zones when liquefaction was triggered. This can also be observed when comparing the shear strains with the q_{c1Ncs} for various depths (Figure 4-18a). For a depth of 7.75 m (within the localized deformation band in Figure 4-16a), the highest strains occur within the weaker zones. For other depths without these localizations, the strains are more evenly distributed across the various zones. This is also true for the other two motions (M4 and M7), which did not trigger high pore pressures.

This demonstrates that the deformation patterns are not only dependent on the distribution of q_{c1Ncs} values, but also on the intensity of the motion.

For the more intense transient motions, the results (Figures 4-17 and 4-20) fall somewhere between the weaker transient motions and the sinusoidal motions. For M4 at a peak acceleration of 0.528 g, high excess pore pressures are quickly triggered near the bottom of the layer and strains concentrate in this zone (Figures 4-17b and 4-20b). This leads to a reduction in the stresses transmitted to shallower layers. For the other two motions, high excess pore pressures are generated across multiple zones within the model and large strains tend to localize in weaker bands.

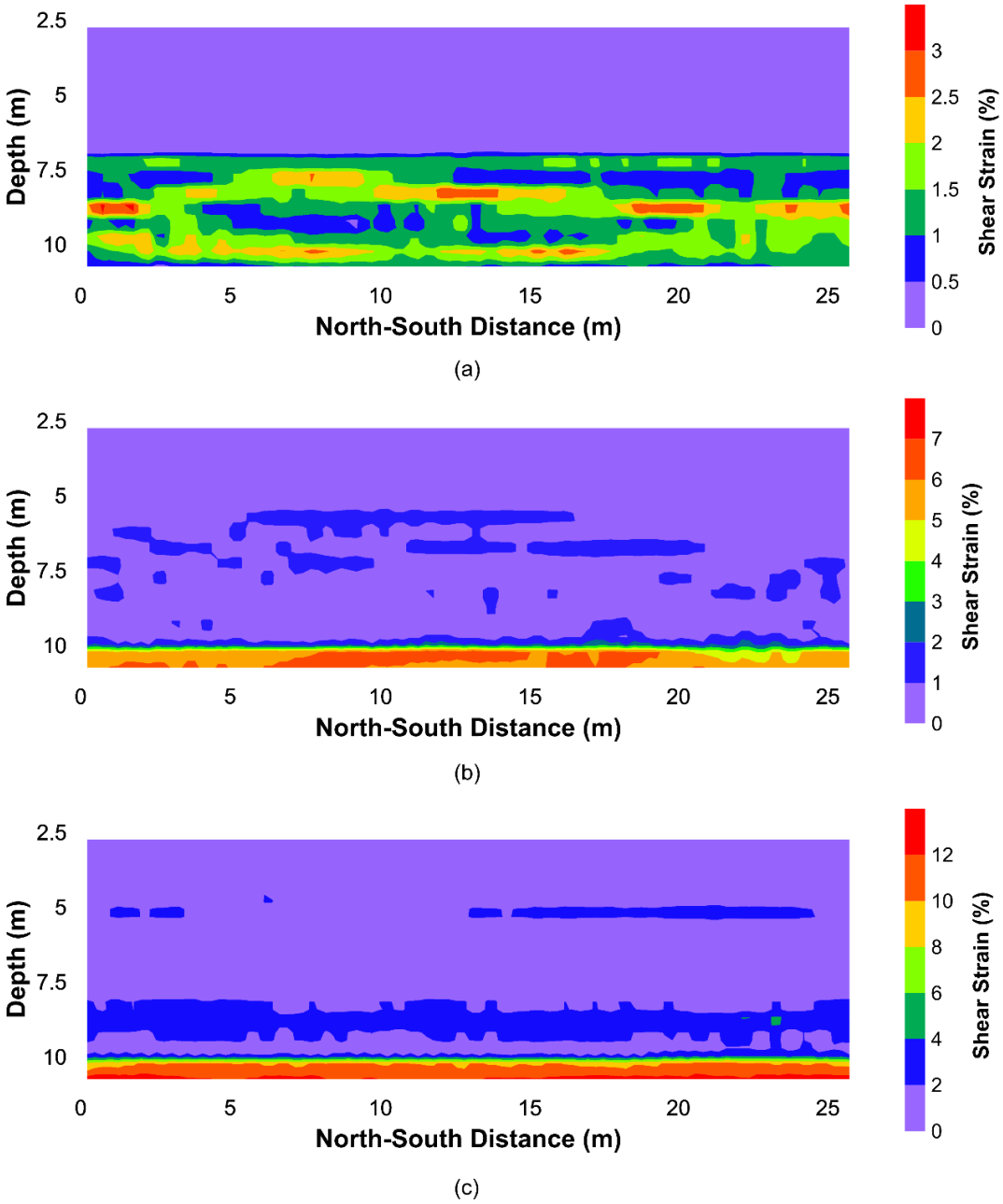

Figure 4-15: Shear strain distribution in section 12 using ramped sinusoidal motions at peak accelerations of (a) 0.13g (b) 0.25g (c) 0.4g.

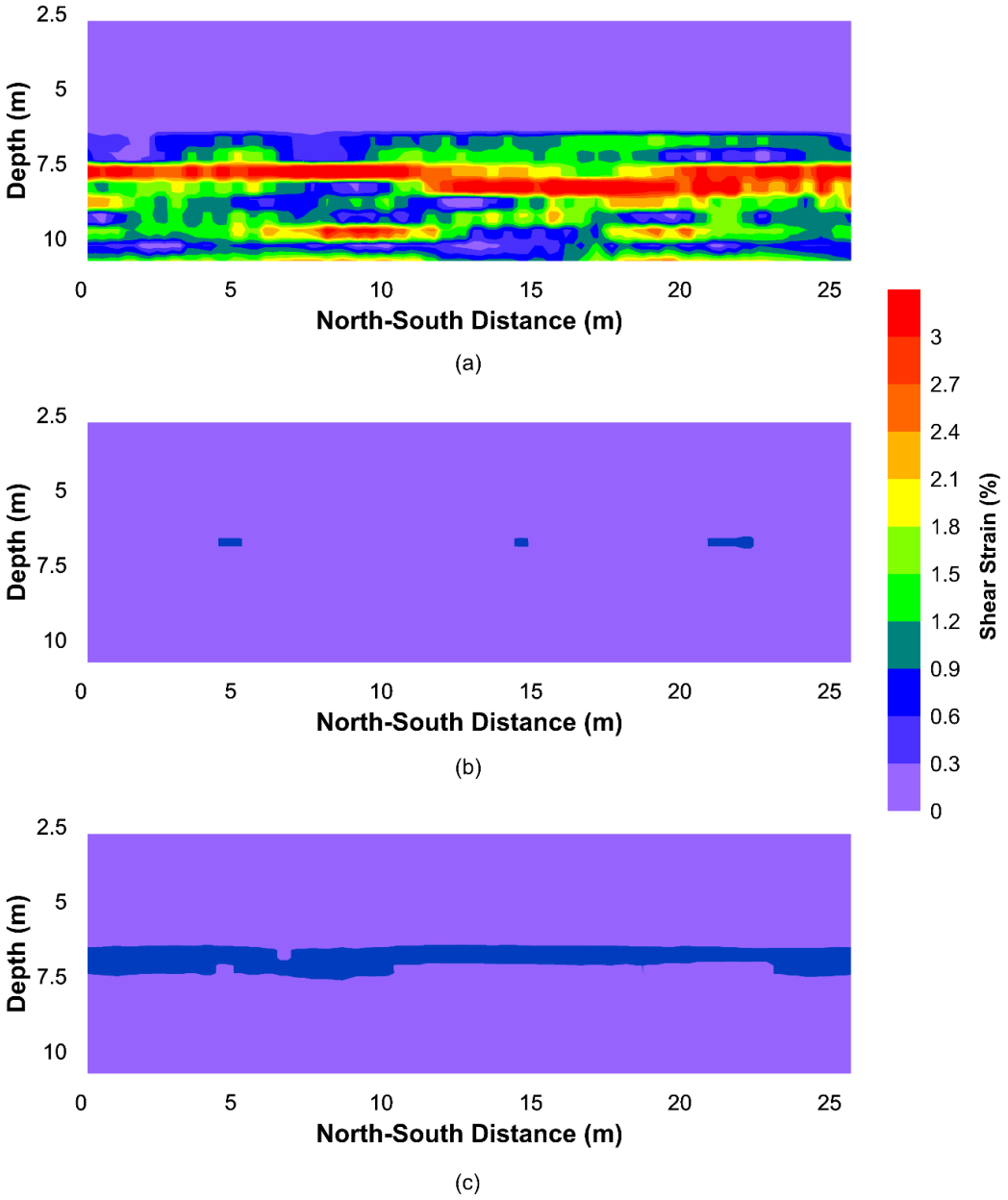

Figure 4-16: End-of-shaking shear strain distribution in section 12 corresponding to the transient motions (a) M1 (b) M4 (c) M7. Each motion corresponds to an acceleration level of 0.25g.

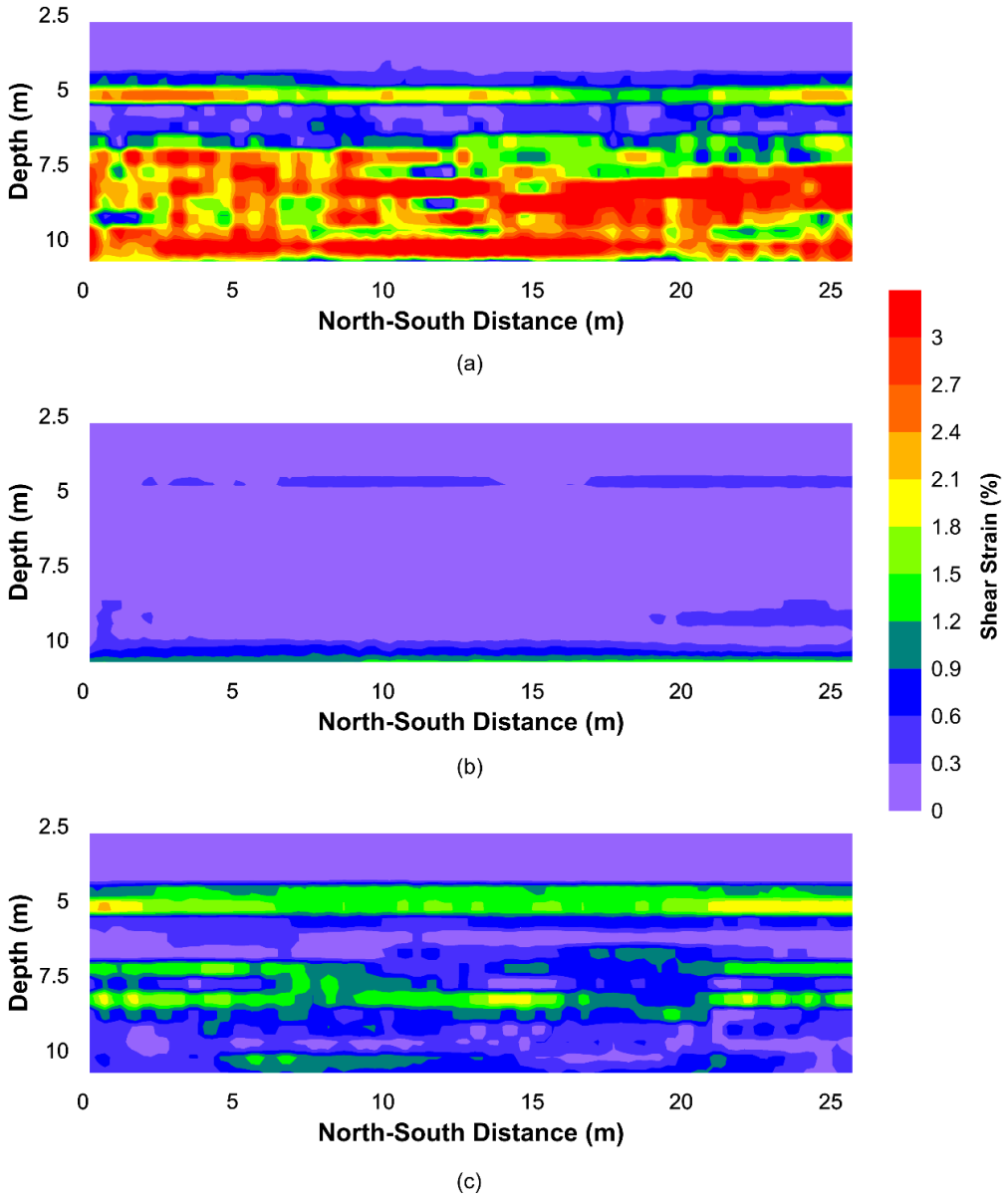

Figure 4-17: End-of-shaking shear strain distribution in section 12 corresponding to the transient motions (a) M1 (b) M4 (c) M7. Each motion corresponds to an acceleration level of 0.528g.

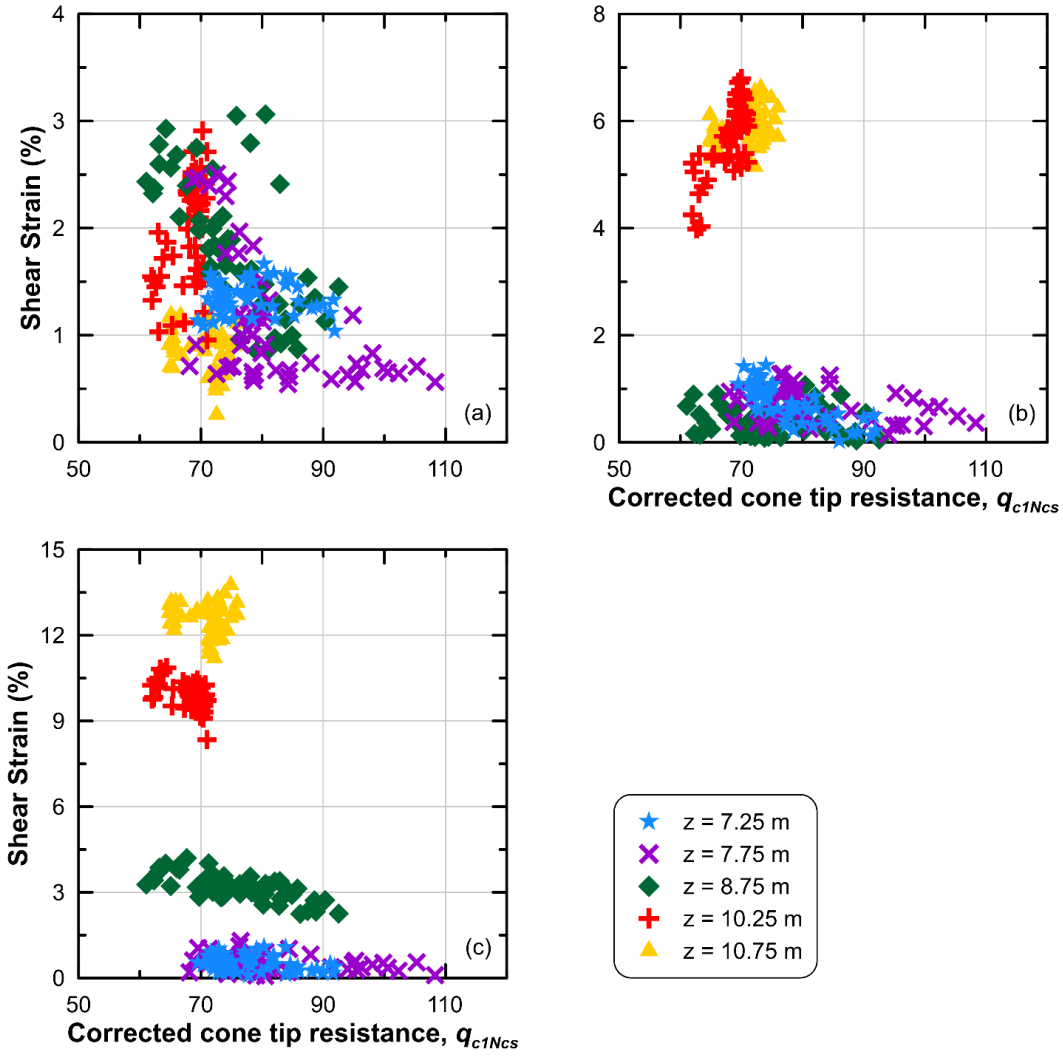

Figure 4-18: Lateral variation of shear strain with q_{c1Ncs} at various depths in section 12 using ramped sinusoidal motions with peak acceleration of (a) 0.13g (b) 0.25g (c) 0.4g.

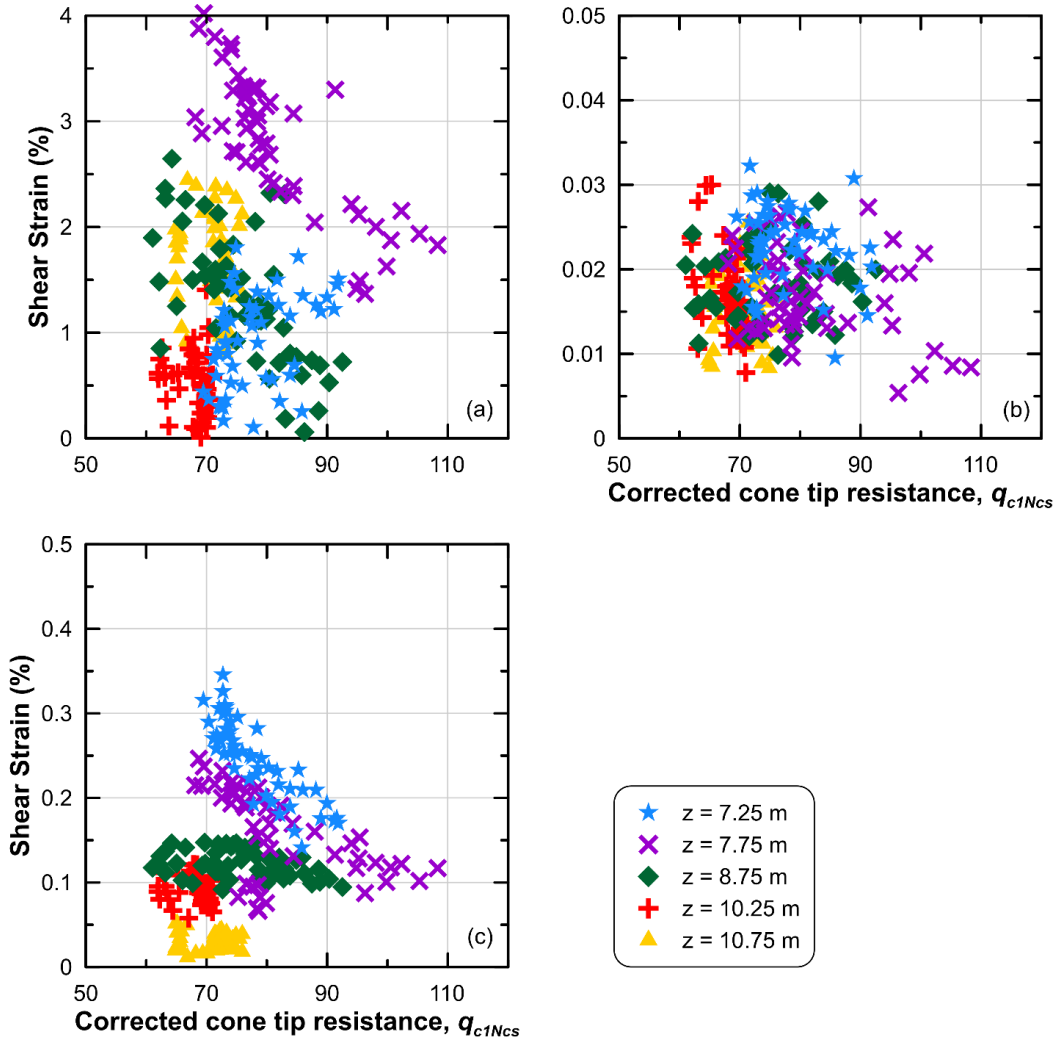

Figure 4-19: Lateral variation of shear strain with q_{c1Ncs} at various depths in section 12 using transient motions (a) M1 (b) M4 (c) M7. All motions correspond to a peak acceleration of 0.25g.

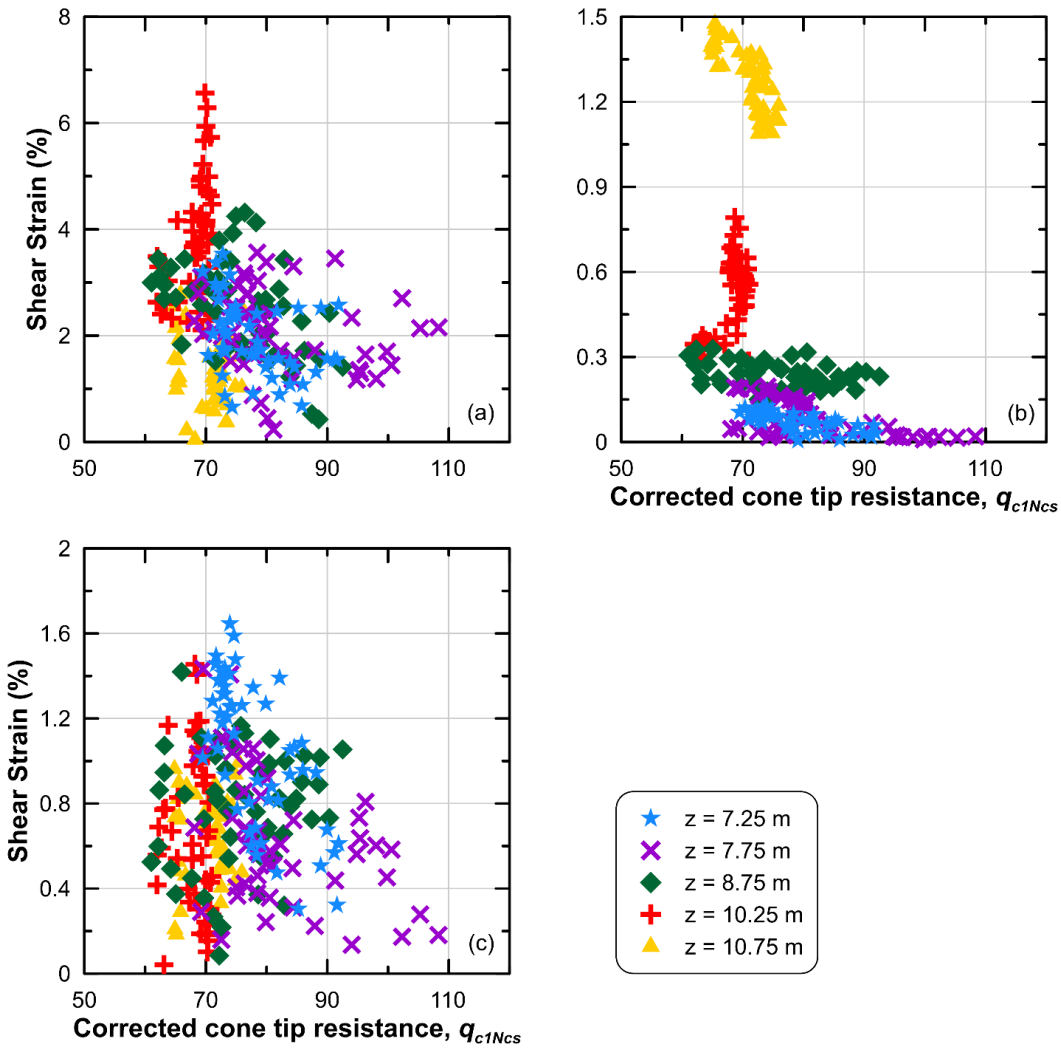

Figure 4-20: Lateral variation of shear strain with q_{c1Ncs} at various depths in section 12 using transient motions (a) M1 (b) M4 (c) M7. All motions correspond to a peak acceleration of 0.528g.

4.5.3 RECONSOLIDATION AND DIFFERENTIAL SETTLEMENT

This section describes the patterns of reconsolidation settlement and differential settlement observed for the simulations. Figure 4-21 shows the surface settlement distribution from 2D simulations of the stochastic sections at the Hollywood test site using ramped sinusoidal motions having different acceleration intensities (as discussed in section 4.4.2). Since the other motion

parameters remained the same, these simulations helped to isolate the effects of acceleration intensity on reconsolidation settlement as well as differential settlement. The reconsolidation settlements were negligible at a peak acceleration of 0.05g but they increased considerably as the peak accelerations were increased to 0.13g and higher. The maximum settlement across the site was approximately 14 cm, which is approximately 40% of the value obtained by Stuedlein and Bong [14] using the Yoshimine et al. [32] empirical procedure. This difference is larger than can be explained by calibration of the reconsolidation parameters alone [33], as is discussed in Section 4.5.5. The considerable difference is likely due to the correlation of volumetric strains with the shear strains in each zone. In the numerical model, strains tend to localize within one to two concentrated bands, while the empirical model considers each depth independently. Ignoring the interactions between the various zones seems to overpredict the strains and therefore the settlements. More work is needed to further explore this idea.

The maximum differential settlements observed for each of the 13 stochastic sections are shown in Figure 4-22. The differential settlements vary between 0.35 – 0.85 cm among the profiles with the maximum values observed for sections 8, 12 and 13. Although differential settlement increased with an increase in peak acceleration from 0.05g to 0.13g for all 13 sections, there was no prominent correlation between the differential settlements and the acceleration intensities higher than 0.13g (Figure 4-22). This is likely due to relatively consistent levels of triggering for each section at higher accelerations. The maximum differential settlement across the entire surface area of the site (based on all 13 sections) is outlined in Figure 4-23 and it increased with an increase in peak acceleration up to 0.25g. The magnitude of differential settlements across the entire surface area was observed to decrease at acceleration values larger than 0.25g (Figure 4-23), as most of the areas experienced considerable excess pore pressure generation at the higher intensities.

However, with a pseudo 3D analysis like the one performed in this study that doesn't consider the interaction effects between different 2D sections, the combined responses from multiple sections (for example, differential settlement over the entire surface area) should be used with caution.

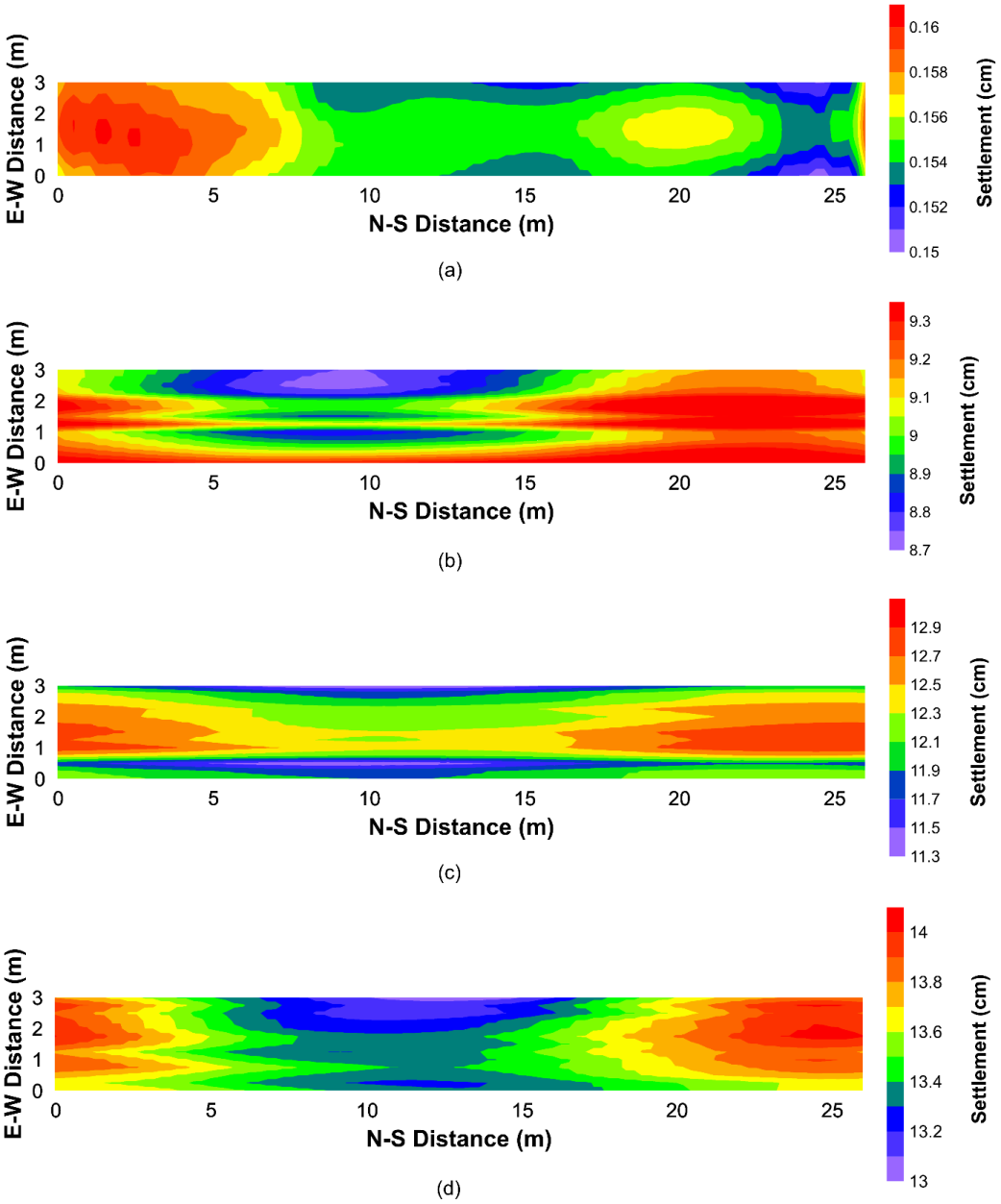

Figure 4-21: Contours of reconsolidation settlement at Hollywood test site using ramped sinusoidal motions having peak accelerations of: (a) 0.05g (b) 0.13g (c) 0.25g and (d) 0.4g.

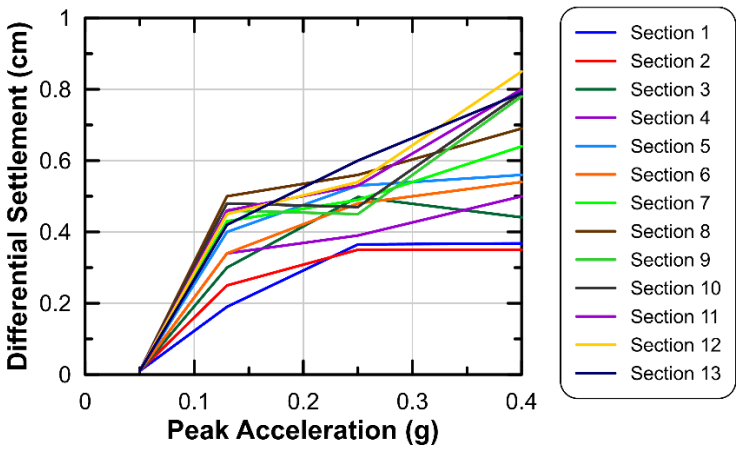

Figure 4-22: Maximum values of differential settlement for each stochastic section using ramped sinusoidal motions having different peak acceleration level.

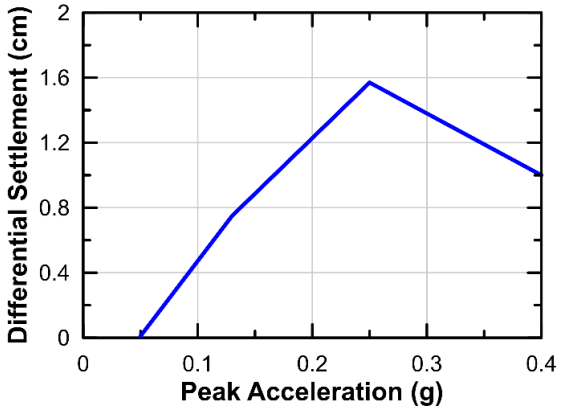

Figure 4-23: Maximum values of simulated differential settlement across the entire surface area at the Hollywood site using ramped sinusoidal motions having various peak acceleration levels.

The mean reconsolidation settlements were computed for each of the 13 stochastic sections. This value corresponds to the average settlement along the N-S direction for any section. The mean settlements simulated for the stochastic sections along with those from the uniform sections are outlined in Figure 4-24. The rate of increase of settlement with peak acceleration was observed to decrease with an increase in acceleration magnitude. The mean settlements from the stochastic sections were similar and they were predicted reasonably accurately by the uniform soil sections

that used a value of q_{c1Ncs} lying between the median and 33rd percentile values from the stochastic sections for peak accelerations higher than 0.15 g (Figure 4-24). At the lowest peak acceleration, the stochastic sections had mean settlement values that were similar to the uniform models with the 16th percentile properties. This is likely due to liquefaction only being triggered within the loosest zones at this low intensity. The difference in settlement between the uniform models using the 16th percentile and median q_{c1Ncs} is approximately 0.7 cm at this intensity and so the error in using a value between the median and 33rd percentile would be very small.

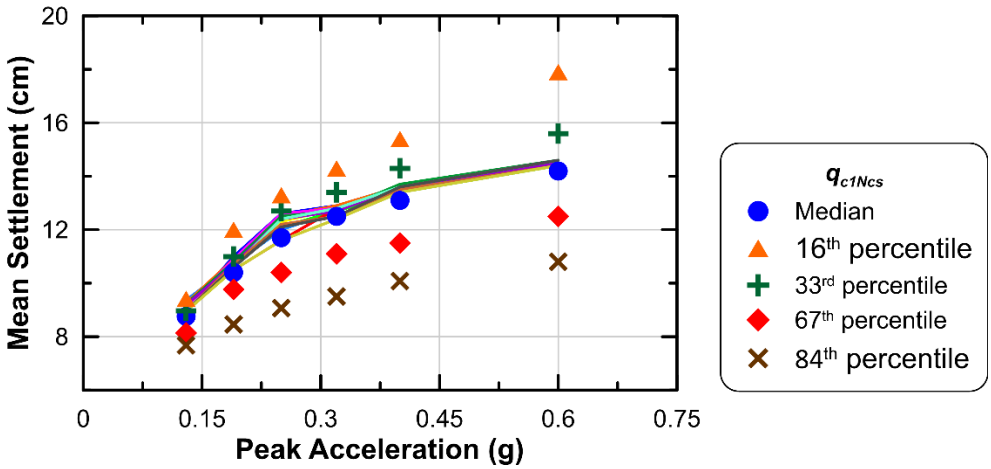

Figure 4-24: Comparison of simulated mean reconsolidation settlements from the stochastic and the uniform sections to peak accelerations of the ramped sinusoidal input motion. Solid lines represent the 13 stochastic sections whereas the symbols correspond to the uniform sections.

This study also investigated the effects of transient motion characteristics on reconsolidation settlement considering the stochastic soil section 12 and a uniform soil section using the median q_{c1Ncs} from the stochastic sections. Figure 4-25 highlights the reconsolidation settlement profiles obtained using the seven transient motions. For the acceleration intensity of 0.25g, the motions M1, M2, M3 and M6 produced the four largest values of reconsolidation settlement in the stochastic section (Figure 4-25a). For the acceleration intensity of 0.528g, the

motion M4 produced considerably lower reconsolidation settlements as compared to the other six motions (Figure 4-25b). This low reconsolidation settlement magnitude is consistent with the low excess pore pressure and shear strain patterns observed for the soil section using motion M4 and was attributed to the low CAV_5 for this motion. Additionally, the settlements simulated for the uniform section (median q_{c1Ncs}) are also plotted alongside the settlements from the stochastic section (Figure 4-25). The uniform section with median q_{c1Ncs} either predicted the settlements reasonably accurately or in general slightly underpredicted the settlements (Figure 4-26). The only exceptions were for M2 (acceleration level of 0.25g) and M4 (acceleration level of 0.528g) wherein the settlements were slightly overpredicted by the uniform section (Figure 4-26). The simulations using a uniform 33rd percentile q_{c1Ncs} value in general overpredicted the settlements (Figure 4-27).

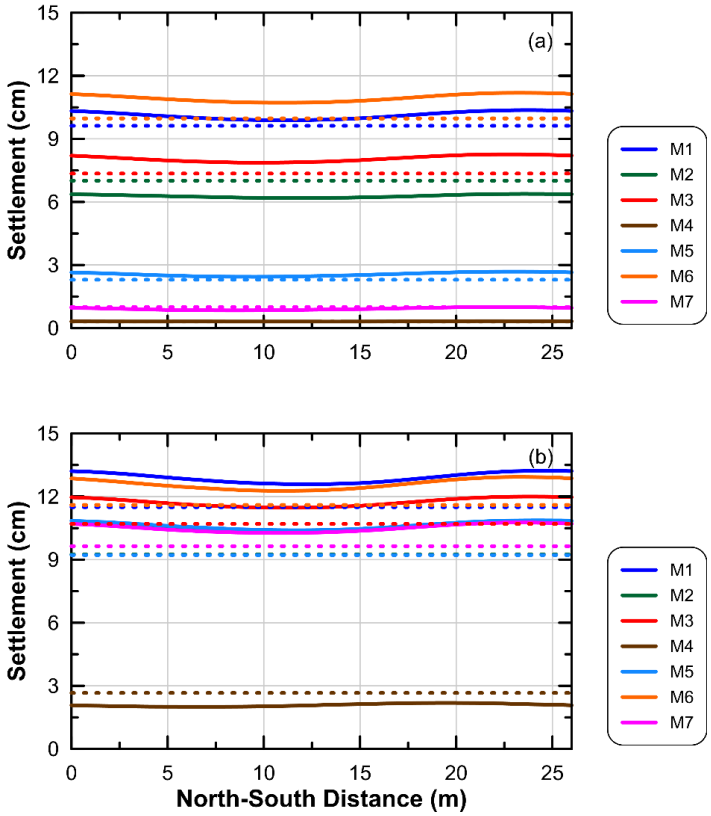

Figure 4-25: Simulated reconsolidation settlement profiles from the stochastic model (section 12) and uniform model (using a representative median q_{c1Ncs} value from the stochastic model) using the seven transient motions having peak accelerations of: (a) 0.25g and (b) 0.528g. The solid lines correspond to the stochastic model whereas the broken lines correspond to the uniform model.

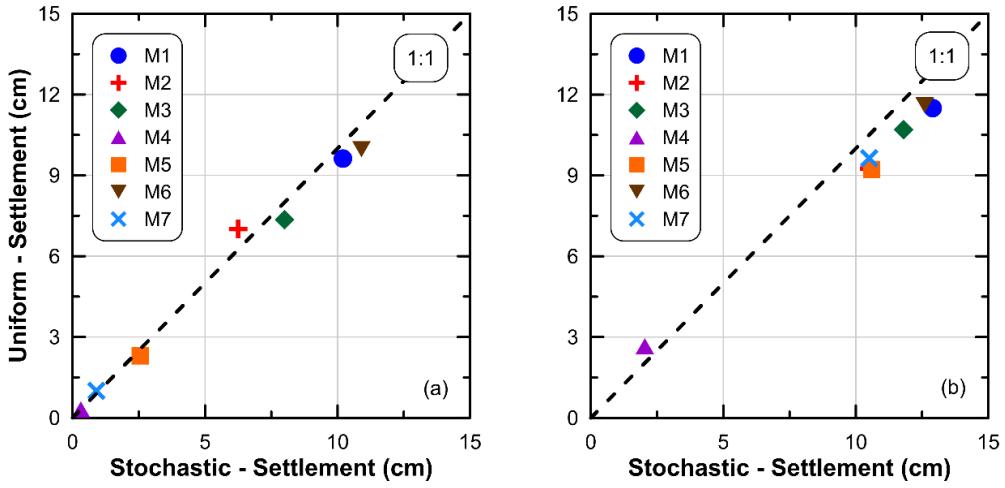

Figure 4-26: Comparison of simulated reconsolidation settlements from stochastic (section 12) and uniform section (using a representative median q_{c1Ncs} value from the stochastic model) at acceleration levels of (a) 0.25g and (b) 0.528g.

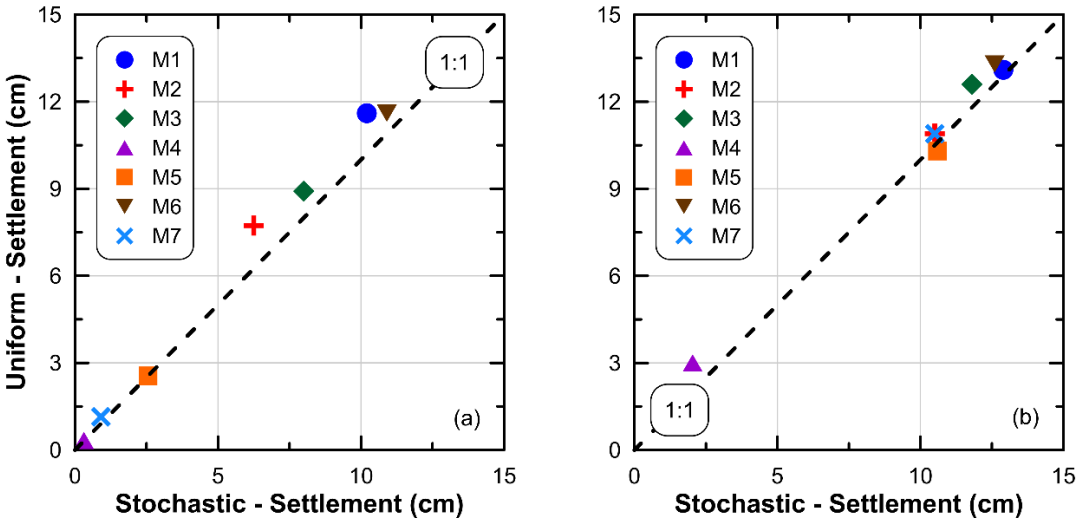

Figure 4-27: Comparison of simulated reconsolidation settlements from stochastic (section 12) and uniform section (using a representative 33rd percentile q_{c1Ncs} value from the stochastic model) at acceleration levels of (a) 0.25g and (b) 0.528g.

4.5.4 CORRELATION BETWEEN INPUT MOTION PARAMETERS CAV_5, ASI AND RECONSOLIDATION SETTLEMENT

The correlation between the mean reconsolidation settlements observed for section 12 subjected to the seven transient motions and the transient motion parameters like CAV_5 and *ASI* are shown in Figures 4-28 and 4-29, respectively. A logarithmic correlation was observed between reconsolidation settlements and the motion parameter CAV_5 and an exponential correlation was observed between settlements and *ASI*. However, the correlation to CAV_5 was observed to be considerably stronger as compared to *ASI*. This was because the correlation pattern between settlements and *ASI* was different among the ramped sinusoidal motions and the transient motions which resulted in a low degree of correlation overall (Figure 4-29).

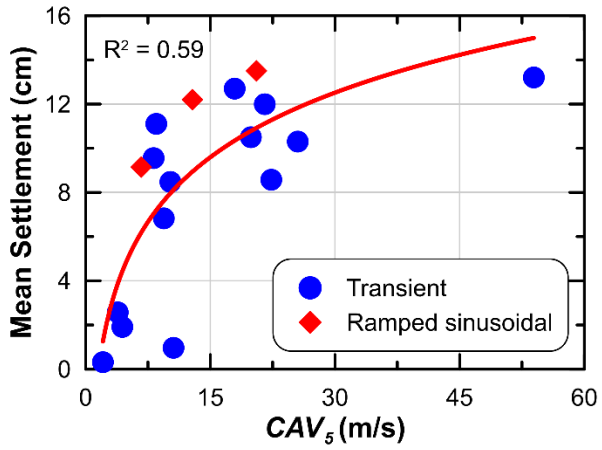

Figure 4-28: Correlation between the mean reconsolidation settlements observed for the stochastic model section and CAV_5.

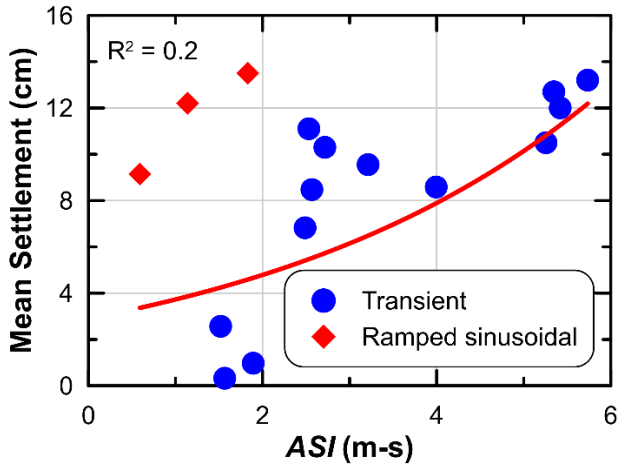

Figure 4-29: Correlation between the mean reconsolidation settlements observed for the stochastic model section and *ASI*.

The mean reconsolidation settlements obtained from the uniform sections using the median and 33rd percentile q_{c1Ncs} values showed a logarithmic correlation to CAV_5 (Figure 4-30). The correlation was slightly stronger in case of the models using the 33rd percentile value as is observed from the R^2 values. However, as observed earlier uniform models using the 33rd percentile q_{c1Ncs}

generally resulted in an overprediction of settlements from the stochastic sections (Figures 4-24 and 4-27).

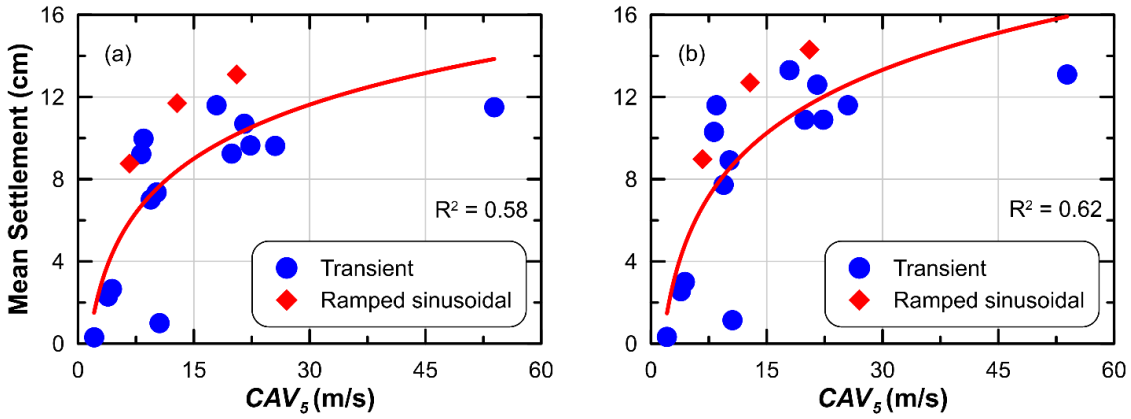

Figure 4-30: Correlation between the mean reconsolidation settlements observed for the uniform model and CAV_5 using (a) median and (b) 33rd percentile q_{c1Ncs} values.

4.5.5 SENSITIVITY ANALYSES

A sensitivity study was performed to evaluate the effects of using a r_u – dependent variable hydraulic conductivity function on reconsolidation settlement and to investigate the necessity of modifying the default PM4Sand reconsolidation parameters to remove any bias in settlement predictions. These simulations correspond to the stochastic section 12 using the ramped sinusoidal input motion having an acceleration intensity of 0.25g. Figure 4-31 shows the post-liquefaction excess pore pressure and settlement responses using the r_u – dependent variable hydraulic conductivity model by Shahir et al. [24]. A value of 12 was selected for the coefficient α based on the D_{10} value of 0.135 [20] for Hollywood sand using the correlation from Chapter 2. Unlike the constant k simulation, some migration of pore water from the bottom of the liquefiable layer (fully-liquefied) towards the top of the layer (partially-liquefied) occurred in case of the variable k

simulation (Figure 4-31a). This phenomenon of migration of pore-water from fully-liquefied sand pockets to partially-liquefied pockets had also been observed in centrifuge experiments on heterogeneous soils [34]. The settlement prediction for the variable *k* model was within 4% of the constant *k* simulation (Figure 4-31b).

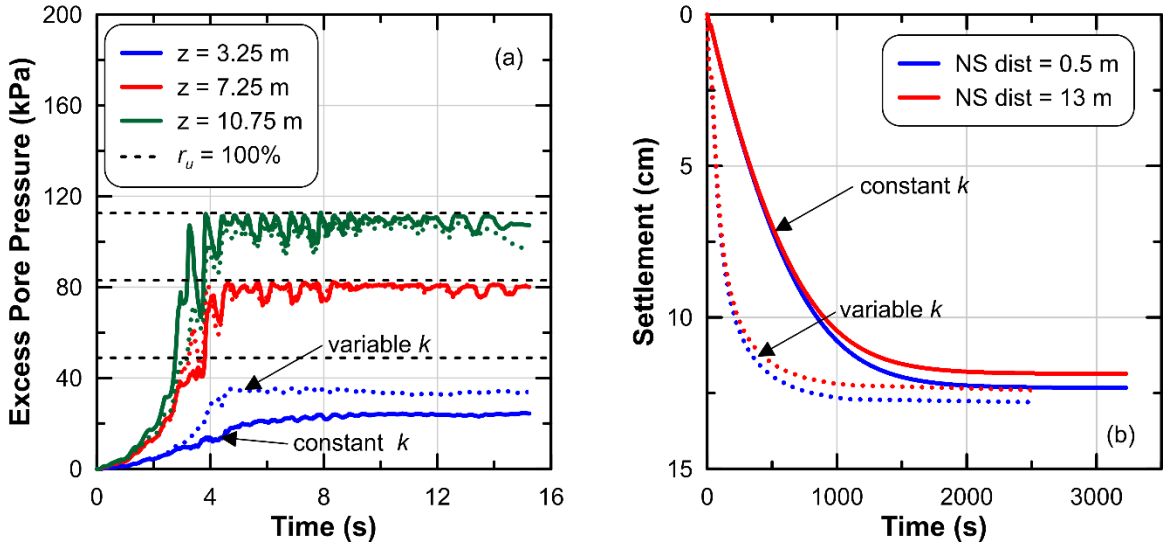

Figure 4-31: Comparison of time histories for (a) excess pore pressure generation and (b) reconsolidation settlement between the r_u – dependent variable hydraulic conductivity and the constant hydraulic conductivity simulations using ramped sinusoidal motion having a peak acceleration of 0.25g. The solid lines correspond to the constant *k* simulation whereas the dotted lines represent the variable *k* simulation.

A second sensitivity analysis was performed to determine the effects of modifying the PM4Sand reconsolidation parameter $f_{sed,min}$ on reconsolidation settlement. An approximate correlation between the D_{10} or D_{50} and the bias in numerical prediction of settlement using the default reconsolidation parameters for PM4Sand was observed in Chapter 2. For a D_{50} of 0.19 and a D_{10} of 0.135 corresponding to Hollywood sand [20], reconsolidation settlement is expected to be underpredicted by 20 – 50%. No laboratory data on Hollywood sand is available to confirm this,

so this value was considered as a sensitivity. The coefficient *A* in Equation 1 was modified to 0.02 from its default value of 0.03 to adjust $f_{sed,min}$. This modified function for $f_{sed,min}$ increased the settlement from 12.4 cm (default) to 17.3 cm (modified), which corresponds to an increase of 40% (Figure 4-32a). These settlements are still approximately 50% less the value of 35 cm estimated by Stuedlein and Bong [14] using empirical approaches. The differential settlement across the NS distance increases from 0.55 cm to 0.65 cm using the modified calibration (Figure 4-32b), which is also considerably less than estimated by Stuedlein and Bong [14]. This demonstrates that the differences between the empirical predictions and the numerical simulations cannot be explained by model calibration alone and are likely due to differences in the response, such as the distribution of shear strains within a profile.

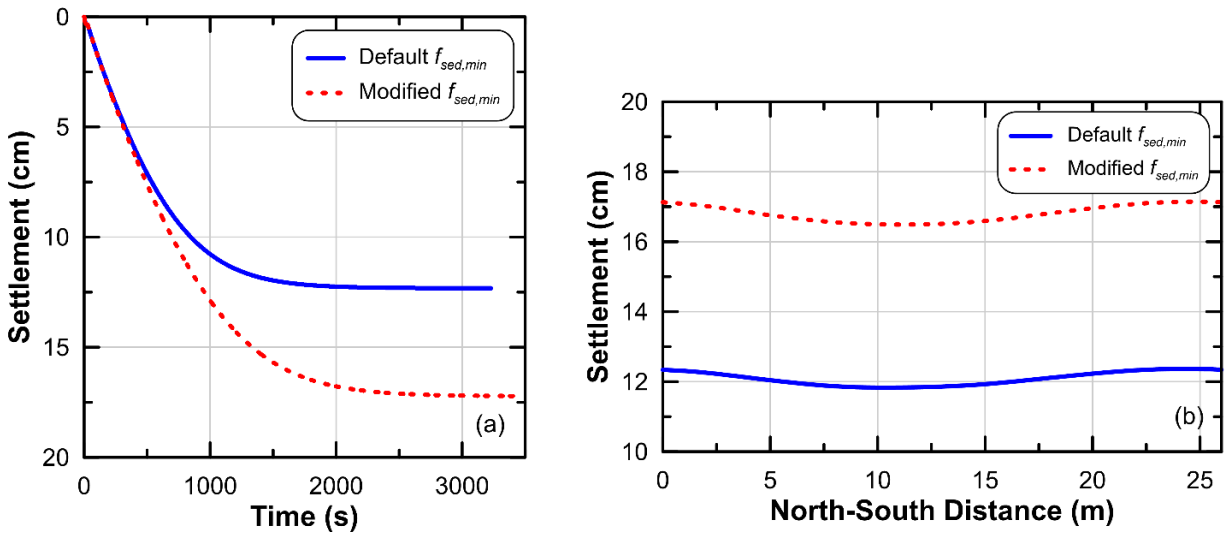

Figure 4-32: Comparison of observed reconsolidation settlements between the default and modified $f_{sed,min}$ simulations using ramped sinusoidal motion having a peak acceleration of 0.25g.

4.6 SUMMARY AND CONCLUDING REMARKS

This chapter highlighted some of the key aspects on numerical modeling of post-liquefaction responses with a focus on reconsolidation settlement for a spatially variable soil deposit. The study focused on a test site at Hollywood in South Carolina that had previously been extensively characterized using SPTs, CPTs, shear wave velocity tests and other field tests. Spatially variable stochastic distribution of fines-corrected cone penetration resistances (q_{c1Ncs}) was estimated for the soil deposit by Bong and Stuedlein [13] using random field theory. Numerical simulations were using the numerical platform FLAC v8.0 and the constitutive model PM4Sand v3.1. The effect of input motion was explored by using both ramped sinusoidal motions with peak accelerations ranging from 0.05g - 0.6g and a suite of recorded transient motions linearly scaled to acceleration intensities of 0.25g and 0.528g based on the expected hazard at the Hollywood site. A sensitivity study was conducted to evaluate the effects of using a variable k model and modified reconsolidation parameters on post-liquefaction responses. Some of the key findings from this study are outlined below:

- For the 13 stochastic soil sections subjected to ramped sinusoidal motions, the mean reconsolidation settlements for the different sections at any particular acceleration intensity were similar. Reconsolidation settlements were observed to be negligible at low shaking intensities of 0.05g and they increased at a sharp rate above this value initially, before producing a much slower rate of increase beyond a peak acceleration of 0.25g. The maximum differential settlements for the sections ranged from 0.35 – 0.85 cm.
- The mean reconsolidation settlements from the stochastic sections were reasonably predicted by using uniform models with the median q_{c1Ncs} from the stochastic distribution. For some sections and motions, the median q_{c1Ncs} underpredicted the settlements, while the

33rd percentile values tended to overpredict the settlements, except at very low intensities. This observation is consistent with Montgomery and Boulanger [2] who found that representative uniform properties varied between the 33rd and 50th percentiles for liquefaction deformations.

- Shear strains tended to localize in one to two narrow bands for the models that generated considerable excess pore pressures. For some of the motions this occurred at the bottom of the liquefiable layer where high excess pore pressures were triggered first leading to a reduction in loading within the upper layers. For other motions, strains tended to localize within interconnected weaker zones within the model.
- For the stochastic sections subjected to transient motions, settlement was observed to vary considerably depending upon the motion parameters like peak acceleration, CAV_5. The uniform section using the median q_{c1Ncs} generally predicted the reconsolidation settlements obtained from the stochastic section accurately, with some minor under/overpredictions observed for some of the motions. The 33rd percentile tended to overpredict the settlements.
- A relatively strong logarithmic correlation was observed between reconsolidation settlements and the motion parameter CAV_5 for both the ramped sine waves and transient motions.
- The magnitude of settlement and differential settlement from the numerical simulations is much lower than would be predicted using empirical models. This is likely due to differences in shear strain accumulation, which directly relate to the magnitude of settlement.
- Using a variable *k* model decreased the amount of time for reconsolidation to occur within the model by 50%, but did not have a significant effect on the magnitude of settlement.

- Changing the $f_{sed,min}$ parameter increased the magnitude of settlement, but did not affect the differential settlement considerably.

This chapter has highlighted some important effects of spatial variability on the reconsolidation behavior of liquefiable soils. Additional work is needed to expand this work to look at three-dimensional variability and to better understand differences between predictions from current empirical approaches and the numerical models. One important factor highlighted in this chapter may be the tendency of the strains within the numerical model to localize into bands, whereas the empirical models consider the response of each depth to be independent of all others. This would result in an overprediction of the shear strains (and therefore the volumetric strains) because the zones that reach a high excess pore pressure first will tend to damp out the energy from the earthquake, reducing the demands on the shallower zones.

CHAPTER 5: SUMMARY, CONCLUSIONS AND FUTURE RESEARCH

5.1 SUMMARY AND CONCLUSIONS

Soil liquefaction poses a major threat to human life and property. Settlement following liquefaction has been one of the major sources of liquefaction-induced damage in past earthquakes and creating resilient infrastructure requires methods to predict this settlement for various types of soil and site conditions. The primary motivation for this study was to improve the existing numerical protocols for liquefaction modeling in order to accurately predict observed liquefaction responses for a range of soil types and explore important factors that influence the magnitude and distribution of reconsolidation settlements. Previous studies in this area have primarily focused on a single site or a single type of soil. This precludes the ability to examine how soil type influences settlement patterns or to assess whether a numerical protocol can predict accurate settlements under various loading paths. This study fills this gap by applying a single numerical protocol (the numerical platform FLAC and constitutive model PM4Sand) to model both excess pore pressure generation and dissipation for three types of problems (uniform centrifuge and shake table tests, centrifuge tests with a retaining wall, and a spatially variable field site) with six different types of soil.

The main objectives of this study were:

- To evaluate the ability of the numerical platform FLAC and constitutive model PM4Sand in capturing the liquefaction-induced responses observed in free-field uniform soil deposits, geosystems involving soil-structure interaction effects and soil deposits with spatially variable properties.

- To examine the necessity of soil-specific calibration of reconsolidation parameters for a constitutive model whenever relevant data is available to ensure reasonable prediction of reconsolidation settlements.
- To investigate the effect of potential changes in hydraulic conductivity (k) due to liquefaction on excess pore pressure, lateral displacement and settlement responses of geosystems.
- To explore the influence of inherent spatial variability in soil properties on the post-liquefaction response of a level-ground site.

These four objectives were met by using FLAC and PM4Sand to numerically model the liquefaction-induced responses observed in free-field uniform soil deposits, a retaining wall with liquefiable backfill, and a site with spatially variable properties. A summary of the work carried out in this study and the conclusions drawn from them are outlined below:

- The main objectives of Chapter 2 were to examine the effects of the model calibrations and potential changes in hydraulic conductivity due to liquefaction on the settlements of different soils subjected to various shaking intensities. Three centrifuge experiments and two shake table tests on free-field uniform sand deposits were numerically modeled in FLAC using the constitutive model PM4Sand. PM4Sand was calibrated to match the cyclic strength of the soils at the target relative density (D_r) using either laboratory test results or by matching the excess pore pressure generation during shaking. In addition to soil-specific dynamic calibration, soil-specific calibration of PM4Sand reconsolidation parameters was performed whenever such data were available. An excess pore pressure ratio (r_u)-dependent hydraulic conductivity (k) model was implemented to examine the effect of k on the responses. PM4Sand was able to reasonably reproduce the excess pore pressure

generation from the experiments, but the accuracy of the predicted rates of dissipation varied. The magnitude of settlement from the simulations was within 60 to 125% of the observed settlements for all of the experiments. However, the settlement was accurately predicted in case of Hostun sand, for which reconsolidation parameters were calibrated to available laboratory data on the compressibility of the sand at low effective stresses. On average, settlements were underpredicted by approximately 15% in case of the other tests for which soil-specific reconsolidation data were unavailable. This mismatch may be partially attributed to settlement mechanisms that were not present in the simulations, such as compression of non-liquefiable layers, ratcheting of displacement sensors into liquefied soil, or possible multi-directional shaking in the centrifuge. A bias was also observed with respect to the grain size of the soil with finer soils having larger underpredictions. More data is needed to confirm this finding. A new, tentative relationship was developed between the increase in hydraulic conductivity due to liquefaction and the effective grain diameter of the soil (D_{10}). This relationship considered the five experiments from this study along with data from eight other studies. While the dataset exhibited scatter, the magnitude of the increase in hydraulic conductivity was observed to decrease with increasing D_{10}. This observation will help to reconcile some of the conflicting observations reported in the literature and provide a means to estimate the hydraulic conductivity of liquefied clean sands when laboratory data is not available.

- Chapter 3 examined the ability of the selected numerical tools and protocols to reasonably capture the experimentally observed responses for a geosystem that involved soil-structural interactions. Simulations were performed for the 11 centrifuge tests from the LEAP 2020 project performed at different geotechnical facilities across the world. The experiments

modeled a sheet-pile wall retaining a stratified sand deposit that consisted of a loose liquefiable layer of Ottawa F-65 sand underlain by a dense layer of the same sand. The D_r (mass-based or CPT-based) selected for the liquefiable sand layer was observed to have a major effect on the simulated liquefaction responses like wall displacement and ground surface settlement. Considering this uncertainty in D_r helped explain some of the significant differences in predicted and observed responses for some of the tests. Only a single CPT measurement was available for each test, but these measurements did show vertical variations in D_r and it is likely that lateral variations existed as well. This variability likely influenced the observations, but no data are available to evaluate this for these centrifuge tests. This served as the motivation for the study undertaken to evaluate the effects of spatial variability on post-liquefaction responses.

- Chapter 4 focused on numerical modeling of a spatially variable soil deposit from a test site at Hollywood, South Carolina that had previously been extensively characterized using SPTs, CPTs, shear wave velocity tests and other field tests. Spatially variable stochastic distribution of fines-corrected cone penetration resistances (q_{c1Ncs}) had been estimated for the soil deposit in a previous research study using random field theory. Numerical simulations were performed by incorporating the spatial variability through correlation of soil properties such as D_r and maximum shear modulus (G_{max}) to $q_{c1Ncs.}$ This study used ramped sinusoidal motions having peak accelerations ranging from 0.05g - 0.6g and a suite of recorded transient motions linearly-scaled to acceleration intensities of 0.25g and 0.528g (based on the expected hazard at the Hollywood site). The mean reconsolidation settlements from any stochastic soil section at any particular acceleration intensity were similar to each other. The mean settlement from the stochastic simulations was reasonably

predicted by using uniform models with the median q_{c1Ncs} from the stochastic distribution. Reconsolidation settlements were observed to be negligible at low shaking intensities of 0.05g and they increased at a sharp rate above this value initially, before leveling off beyond a peak acceleration of 0.25g. Shear strain localization in narrow bands was observed in many of the simulations that showed high excess pore pressure. A relatively strong logarithmic correlation was observed between reconsolidation settlements and the input motion parameter CAV_5.

In general, this study highlighted some of the key aspects on numerical modeling of liquefaction-induced settlements. It discussed the ability of the numerical platform FLAC and constitutive model PM4Sand in capturing the liquefaction-induced responses observed in free-field uniform soil deposits, geosystems involving soil-structure interaction effects and soil deposits with spatially variable properties. To ensure reasonable prediction of reconsolidation settlements, soil-specific calibration of reconsolidation parameters for a constitutive model was deemed as necessary whenever relevant data is available. A new relationship was developed between the increase in hydraulic conductivity due to liquefaction and D_{10}. The bias in settlement predictions was observed to correlate to measures of grain size for the sands examined in this study. The importance of accurate estimation of D_r for reliable numerical predictions of post-liquefaction responses was investigated. Consideration of the uncertainty in D_r estimates from laboratory experiments was observed to be important for accurate prediction of numerical responses. The physical mechanisms associated with liquefaction in a spatially variable soil deposit were investigated using the numerical framework considered in this study. One important factor for spatially variable deposits was the tendency of the strains within the numerical model to localize into bands, reducing the shear strains and therefore settlements in the rest of the layer.

5.2 FUTURE RESEARCH

As discussed above, soil-specific calibration of reconsolidation parameters of a constitutive model was crucial in predicting reconsolidation settlements accurately for Hostun sand. However, laboratory data on the compressibility of soils at low effective stresses are not commonly available. Additional work is needed to measure the compressibility of various liquefied soils, including natural soils to determine if calibration to these values can improve settlement predictions for other soils as well. Moreover, the bias in settlement predictions was observed to correlate to measures of grain size for the sands examined in this study. Additional tests on other soils with a wider range of grain sizes are needed to determine if correlations can be developed between post-liquefaction stiffness and the grain size of the soil for use when soil-specific data is not available.

The numerical approach described herein has been used to study the liquefaction-induced responses of a spatially variable soil subjected to different loading mechanisms. However, this approach needs to be further validated against well-characterized or instrumented case histories of liquefaction. Additional work is required to incorporate stratigraphic variability into the numerical modeling framework such as inclined strata, presence of static shear stress and fine-grained soil pockets within a liquefiable sand layer. The effects of these features on reconsolidation response need to be evaluated.

This study used a flag-based approach of reducing post-shaking moduli to capture sedimentation effects and reconsolidation strain. However, this approach cannot capture ejecta which is one of the most important indicators of liquefaction manifestation in the field. Moreover, ejecta can lead to large settlements and has the potential to alter the post-shaking characteristics of the liquefied/reconsolidating soil strata. Therefore, numerical modeling techniques beyond this

flag-based approach need to be developed that can capture the real physics of the problem. Until this is done, the approach used in this study has been demonstrated to provide reasonable results for the range of soils and loading conditions examined.

CHAPTER 6: REFERENCES

6.1 REFERENCES (CHAPTER 1)

[1] Mogami T, Kubu K. The behavior of soil during vibration. 3rd International Conference on Soil Mechanics and Foundation Engineering 1953;1:152-155.

[2] Wakamatsu K, Yoshida N, Kiku H. Liquefaction during the 2004 Niigata-Ken-Chuetsu earthquake- General aspect and geotechnical and geomorphologic conditions. Doboku Gakkai Ronbunshuu 2006;62:263-276.

[3] Polshin DE, Tokar RA. Maximum allowable non-uniform settlement of structures. Proceedings of the 4th ICSMFE 1957;1:402-406.

[4] Youd TL. Ground failure investigations following the 1964 Alaska earthquake. Tenth U.S. National Conference on Earthquake Engineering 2014.

[5] Ishihara K, Koga Y. Case Studies of Liquefaction in the 1964 Niigata Earthquake. Soils Found 1981;21:35-52.

[6] Seed HB, Idriss IM, Analysis of soil liquefaction: Niigata earthquake, Dept. of Civil Engineering [and] Institute of Transportation and Traffic Engineering, University of California, Berkeley, Calif., 1967.

[7] Iwasaki T, Tatsuoka F, Tokia K, Yasuda S. A practical method for assessing soil liquefaction potential based on case studies at various sites in Japan. Proceedings of the 2nd International Conference on Microzonation 1978.

[8] Soga K. Soil liquefaction effects observed in the Kobe earthquake of 1995. Proceedings of the Institution of Civil Engineers - Geotechnical Engineering 1998;131:34-51.

[9] Rajendran K, Rajendran CP, Thakkar M, Tuttle MP. The 2001 Kutch (Bhuj) earthquake: Coseismic surface features and their significance. Current Sci 2001;80:1397-1405.

[10] Cubrinovski M, Bray JD, Taylor M, Giorgini S, Bradley B, Wotherspoon L, Zupan J. Soil Liquefaction Effects in the Central Business District during the February 2011 Christchurch Earthquake. Seismological Research Letters 2011;82:893-904.

[11] Rathje E, Bachhuber J, Cox B, French J, Green R, Olson S, Rix G, Wells D, Suncar O. Geotechnical Engineering Reconnaissance of the 2010 Haiti Earthquake. GEER Report 2010, Version 1.

[12] Kusumawardani R, Chang M, Upomo TC, Huang R-C, Fansuri MH, Prayitno GA. Understanding of Petobo liquefaction flowslide by 2018.09.28 Palu-Donggala Indonesia earthquake based on site reconnaissance. Landslides 2021.

[13] Mavroulis S, Lekkas E, Carydis P. Liquefaction Phenomena Induced by the 26 November 2019, Mw = 6.4 Durrës (Albania) Earthquake and Liquefaction Susceptibility Assessment in the Affected Area. Geosciences 2021;11.

[14] Miranda E, Brzev S, Bijelic N, Arbanas Ž, Bartolac M, Jagodnik V, Lazarević D, Mihalić Arbanas S, Zlatović S, Acosta A, Archbold J, Bantis J, Borozan J, Božulić I, Blagojević N, Cruz C, Dávalos H, Fischer E, Gunay S, Hadzima-Nyarko M, Heresi P, Lignos D, Lin T, Marinković M, Messina A, Miranda S, Poulos A, Scagliotti G, Tomac I, Tomic I, Ziotopoulou K, Žugić Ž, Robertson I. Petrinja, Croatia December 29, 2020, Mw 6.4 Earthquake Joint Reconnaissance Report (JRR). 2021;PRJ-2959.

[15] Ishihara K. Liquefaction and flow failure during earthquakes. Géotechnique 1993;43:351-451.

[16] Wong RT, Seed HB, Chan CK. Liquefaction of gravelly soil under cyclic loading conditions. J Geotech Eng Div 1975;101:574-583.

[17] Bray JD, Sancio RB. Assessment of the Liquefaction Susceptibility of Fine-Grained Soils. J Geotech Geoenviron Eng 2006;132:1165-1177.

[18] Boulanger R, W., Idriss IM. Liquefaction Susceptibility Criteria for Silts and Clays. J Geotech Geoenviron Eng 2006;132:1413-1426.

[19] Kiernan M, Montgomery J. Numerical Simulations of Fourth Avenue Landslide Considering Cyclic Softening. J Geotech Geoenviron Eng 2020;146:04020099.

[20] Seed HB, Lee KL. Liquefaction of saturated sands during cyclic loading. J Soil Mech Found Div 1966;92:105-134.

[21] Wu J, Kammerer AM, Riemer MF, Seed RB, Pestana JM. Laboratory study of liquefaction triggering criteria. 13th World Conference on Earthquake Engineering 2004.

[22] Kramer SL, Liquefaction in: P.T. Bobrowsky (Ed.) Encyclopedia of Natural Hazards, Springer Netherlands, Dordrecht, 2013, pp. 629-633.

[23] Ladd RS, Dobry R, Dutko P, Yokel FY, Chung RM. Pore-Water Pressure Buildup in Clean Sands Because of Cyclic Straining. J Geotech Test 1989;12:77-86.

[24] Youd TL, Idriss IM, Andrus RD, Arango I, Castro G, Christian JT, Dobry R, Finn WDL, Harder LF, Hynes ME, Ishihara K, Koester JP, Liao SSC, Marcuson WF, Martin GR, Mitchell JK, Moriwaki Y, Power MS, Robertson PK, Seed RB, Stokoe KH. Liquefaction Resistance of Soils: Summary Report from the 1996 NCEER and 1998 NCEER/NSF Workshops on Evaluation of Liquefaction Resistance of Soils. J Geotech Geoenviron Eng 2001;127:817-833.

[25] Boulanger Ross W, Idriss IM. CPT-Based Liquefaction Triggering Procedure. J Geotech Geoenviron Eng 2016;142:04015065.

[26] Idriss IM, Boulanger RW. SPT-Based Liquefaction Triggering Procedures. Report No. UCD/CGM-10/02 2010.

[27] El Ghoraiby MA, Manzari MT. LEAP-2020: Cyclic direct simple shear tests performed at GWU. DesignSafe-CI 2020.

[28] Tokimatsu K, Seed HB. Evaluation of settlements in sands due to earthquake shaking. J Geotech Eng 1987;113:861-878.

[29] Ishihara K, Yoshimine M. Evaluation of settlements in sand deposits following liquefaction during earthquakes. Soils Found 1992;32:173-188.

[30] Pradel D. Procedure to evaluate earthquake-induced settlements in dry sandy soils. J Geotech Geoenviron Eng 1998;124:364-368.

[31] Zhang G, Robertson PK, Brachman RWI. Estimating liquefaction-induced ground settlements from CPT for level ground. Can Geotech J 2002;39:1168-1180.

[32] Sento N, Kazama M, Uzuoka R. Experiment and idealization of the volumetric compression characteristics of clean sand after undrained cyclic shear. J Jpn Soc Civ Eng 2004;764:307-317.

[33] Yoshimine M, Nishizaki H, Amano K, Hosono Y. Flow deformation of liquefied sand under constant shear load and its application to analysis of flow slide of infinite slope. Soil Dynam Earthq Eng 2006;26:253-264.

[34] Robertson PK, Shao L. Estimation of Seismic Compression in Dry Soils Using the CPT. International Conferences on Recent Advances in Geotechnical Earthquake Engineering and Soil Dynamics 2010.

[35] Geyin M, Maurer BW, An analysis of liquefaction-induced free-field ground settlement using 1,000+ case histories: Observations vs. state-of-practice predictions in: Geo-Congress 2019, 2019, pp. 489-498.

[36] Banister JR, Winters L, Ellett DM, Pyke RM. In-situ pore presure measurements at Rio Blanco. J Geotech Eng Div 1976;102:1073-1091.

[37] Beyzaei CZ, Bray JD, Cubrinovski M, Bastin S, Stringer M, Jacka M, Ballegooy Sv, Riemer M, Wentz R. Characterization of silty soil thin layering and groundwater conditions for liquefaction assessment. Can Geotech J 2020;57:263-276.

[38] Youd TL, Garris CT. Liquefaction-induced ground-surface disruption. J Geotech Eng 1995;121:805-809.

[39] Green RA, Maurer BW, Ballegooy SV, The influence of the non-liquefied crust on the severity of surficial liquefaction manifestations: Case history from the 2016 Valentine's day earthquake in New Zealand in: Geotechnical Earthquake Engineering and Soil Dynamics V, 2018, pp. 21-32.

[40] Lewis MR, Arango I, McHood MD, Site characterization philosophy and liquefaction evaluation of aged sands: A Savannah river site and Bechtel perspective in: From Research to Practice in Geotechnical Engineering, 2008, pp. 540-558.

[41] Bwambale B, Andrus RD. State of the art in the assessment of aging effects on soil liquefaction. Soil Dynam Earthq Eng 2019;125:105658.

[42] Popescu R, Prevost JH. Centrifuge validation of a numerical model for dynamic soil liquefaction. Soil Dynam Earthq Eng 1993;12:73-90.

[43] Sharp MK, Dobry R, Abdoun T. Liquefaction centrifuge modeling of sands of different permeability. J Geotech Geoenviron Eng 2003;129:1083-1091.

[44] Ecemis N. Simulation of seismic liquefaction: 1-g model testing system and shaking table tests. Eur J Environ Civ Eng 2013;17:899-919.

[45] Kutter BL. Dynamic centrifuge modeling of geotechnical structures. Transportation Research Record, TRB, National Research Council 1992:24-30.

[46] Iai S, Tobita T, Nakahara T. Generalised scaling relations for dynamic centrifuge tests. Géotechnique 2005;55:355-362.

[47] Ha D, Abdoun T, O'Rourke M, Laak PV, O'Rourke T, Stewart H. Split-containers for centrifuge modeling of permanent ground deformation effects on buried pipeline systems. 6th International Conference on Physical Modelling in Geotechnics 2006:729-734.

[48] Srilatha N, Madhavi Latha G, Puttappa CG. Effect of frequency on seismic response of reinforced soil slopes in shaking table tests. Geotextiles and Geomembranes 2013;36:27-32.

[49] Byrne PM, Park S-S, Beaty M, Sharp M, Gonzalez L, Abdoun T. Numerical modeling of liquefaction and comparison with centrifuge tests. Can Geotech J 2004;41:193-211.

[50] Dashti S, Bray JD. Numerical simulation of building response on liquefiable sand. J Geotech Geoenviron Eng 2013;139:1235-1249.

[51] Chian SC, Tokimatsu K, Madabhushi SPG. Soil liquefaction–induced uplift of underground structures: physical and numerical modeling. J Geotech Geoenviron Eng 2014;140:04014057.

[52] Tang L, Zhang X, Ling X. Numerical simulation of centrifuge experiments on liquefaction mitigation of silty soils using stone columns. KSCE J Civ Eng 2016;20:631-638.

[53] Taylor ML, Clayton PJ, Chin CY. Assessment of liquefaction induced settlement within engineering practice. NZSEE 2021 Annual Conference 2021.

[54] Ramirez J, Barrero AR, Chen L, Dashti S, Ghofrani A, Taiebat M, Arduino P. Site response in a layered liquefiable deposit: evaluation of different numerical tools and methodologies with centrifuge experimental results. J Geotech Geoenviron Eng 2018;144:04018073.

[55] Giannakou A, Travasarou T, Chacko J. Numerical Modeling of Liquefaction-Induced Slope Movements. Geo-Congress GSP-225 2012.

[56] Forcellini D. Numerical simulations of liquefaction on an ordinary building during Italian (20 May 2012) earthquake. Bull Earthq Eng 2019;17:4797-4823.

[57] Beaty MH, Byrne PM. UBCSAND constitutive model version 904aR. Itasca UDM Web Site 2011;69.

[58] Boulanger RW, Ziotopoulou K. PM4Sand (Version 3.1): A sand plasticity model for earthquake engineering applications. Report No. UCD/CGM-17/01, Davis, CA: University of California, Davis. 2017.

[59] Wang Z-L, Dafalias YF, Shen C-K. Bounding surface hypoplasticity model for sand. J Eng Mech 1990;116:983-1001.

[60] Elgamal A, Yang Z, Parra E. Computational modeling of cyclic mobility and post-liquefaction site response. Soil Dynam Earthq Eng 2002;22:259-271.

[61] Abkenar MR. A Critical State Two-Surface Plasticity Model for Simulation of Flow Liquefaction and Cyclic Mobility. Ph.D dissertation. The George Washington University 2017.

[62] Ziotopoulou K, Boulanger RW. Numerical modeling issues in predicting post-liquefaction reconsolidation strains and settlements. The 10th International Conference on Urban Earthquake Engineering 2013.

[63] Howell R, Rathje EM, Boulanger RW. Evaluation of simulation models of lateral spread sites treated with prefabricated vertical drains. J Geotech Geoenviron Eng 2015;141:04014076.

[64] Armstrong RJ, Boulanger RW. Numerical Simulations of Liquefaction Effects on Piled Bridge Abutments. 6th International Conference on Earthquake Geotechnical Engineering 2015.

[65] Pyke RM, Chan CK, Seed HB. Settlement of Sands under Multidirectional Shaking. J Geotech Eng Div 1975;101:379-398.

[66] Fenton GA, Vanmarcke EH. Spatial variation in liquefaction risk. Géotechnique 1998;48:819-831.

[67] Lumb P. Spatial variability of soil properties. 2nd International Conference on Application of Statistics and Probability in Soil and Structural Engineering 1975:397-421.

[68] Phoon K-K, Kulhawy FH. Characterization of geotechnical variability. Can Geotech J 1999;36:612-624.

[69] Stuedlein AW, Bong T. Effect of Spatial Variability on Static and Liquefaction-Induced Differential Settlements. Geo-Risk GSP 282 2017.

[70] DeGroot DJ, Baecher GB. Estimating Autocovariance of In-Situ Soil Properties. J Geotech Eng 1993;119:147-166.

[71] Griffiths DV, Fenton GA, Manoharan N. Bearing Capacity of Rough Rigid Strip Footing on Cohesive Soil: Probabilistic Study. J Geotech Geoenviron Eng 2002;128:743-755.

[72] Bong T, Stuedlein AW. Spatial Variability of CPT Parameters and Silty Fines in Liquefiable Beach Sands. J Geotech Geoenviron Eng 2017;143:04017093.

[73] Baecher GB, Jaksa MB, Brooker PI, Kaggwa WS. Inaccuracies Associated with Estimating Random Measurement Errors. J Geotech Geoenviron Eng 1999;125:79-80.

[74] Vanmarcke EH. Probabilistic Modeling of Soil Profiles. J Geotech Eng Div 1977;103:1227-1246.

[75] Bong T, Stuedlein AW. Effect of Cone Penetration Conditioning on Random Field Model Parameters and Impact of Spatial Variability on Liquefaction-Induced Differential Settlements. J Geotech Geoenviron Eng 2018;144:04018018.

[76] Popescu R, Prevost JH, Deodatis G. Effects of spatial variability on soil liquefaction: some design recommendations. Géotechnique 1997;47:1019-1036.

[77] Montgomery J, Boulanger RW. Effects of spatial variability on liquefaction-induced settlement and lateral spreading. J Geotech Geoenviron Eng 2017;143:04016086.

[78] Dafalias YF, Manzari MT. Simple plasticity sand model accounting for fabric change effects. J Eng Mech 2004;130:622-634.

[79] Itasca. FLAC (Version 8.0) – Fast Lagrangian Analysis of Continua. Itasca Consulting Group, Inc., Minneapolis, Minnesota 2016.

[80] Popescu R, Prevost JH, Deodatis G. 3D effects in seismic liquefaction of stochastically variable soil deposits. In: Risk and Variability in Geotechnical Engineering, 2005, pp. 81-91.

[81] Montoya-Noguera S, Lopez-Caballero F. Numerical modeling of discrete spatial heterogeneity in seismic risk analysis: application to treated ground soil foundation. Georisk: Assessment and Management of Risk for Engineered Systems and Geohazards 2016;10:66-82.

[82] Rahmani A, Ghasemi Fare O, Pak A. Investigation of the influence of permeability coefficient on the numerical modeling of the liquefaction phenomenon. Sci Iran 2012;19:179-187.

[83] Ghassemi A, Seyfi S, Shahir H. Evaluation of variable permeability model in simulation of seismic behavior of uniform level and gently sloping sand layers. Earth Sci Res J 2020;24:335-343.

6.2 REFERENCES (CHAPTER 2)

[1] Shahir H, Pak A, Taiebat M, Jeremić B. Evaluation of variation of permeability in liquefiable soil under earthquake loading. Comput Geotech 2012;40:74-88.

[2] Adamidis O, Madabhushi SPG. Experimental investigation of drainage during earthquake-induced liquefaction. Géotechnique 2018;68:655-665.

[3] Ramirez J, Barrero AR, Chen L, Dashti S, Ghofrani A, Taiebat M, Arduino P. Site response in a layered liquefiable deposit: evaluation of different numerical tools and methodologies with centrifuge experimental results. J Geotech Geoenviron Eng 2018;144:04018073.

[4] Mehrzad B, Jafarian Y, Lee CJ, Haddad AH. Centrifuge study into the effect of liquefaction extent on permanent settlement and seismic response of shallow foundations. Soils Found 2018;58:228-240.

[5] Ecemis N. Experimental and numerical modeling on the liquefaction potential and ground settlement of silt-interlayered stratified sands. Soil Dynam Earthq Eng 2021;144:106691.

[6] Thevanayagam S, Kanagalingam T, Reinhorn A, Tharmendhira R, Dobry R, Pitman M, Abdoun T, Elgamal A, Zeghal M, Ecemis N, El Shamy U. Laminar box system for 1-g physical modeling of liquefaction and lateral spreading. J Geotech Test 2009;32:438-449.

[7] Iai S, Tobita T, Nakahara T. Generalised scaling relations for dynamic centrifuge tests. Géotechnique 2005;55:355-362.

[8] Itasca. FLAC (Version 8.0) – Fast Lagrangian Analysis of Continua. Itasca Consulting Group, Inc., Minneapolis, Minnesota 2016.

[9] Boulanger RW, Ziotopoulou K. PM4Sand (Version 3.1): A sand plasticity model for earthquake engineering applications. Report No. UCD/CGM-17/01, Davis, CA: University of California, Davis. 2017.

[10] Howell R, Rathje EM, Boulanger RW. Evaluation of simulation models of lateral spread sites treated with prefabricated vertical drains. J Geotech Geoenviron Eng 2015;141:04014076.

[11] Ziotopoulou K, Boulanger RW. Numerical modeling issues in predicting post-liquefaction reconsolidation strains and settlements. In: The 10th International Conference on Urban Earthquake Engineering. 2013.

[12] Ishihara K, Yoshimine M. Evaluation of settlements in sand deposits following liquefaction during earthquakes. Soils Found 1992;32:173-188.

[13] Amat AS. Elastic stiffness moduli of Hostun sand. Master thesis. Department of Civil Engineering, University of Bristol, UK 2007.

[14] Goudarzy M, Rahemi N, Rahman MM, Schanz T. Predicting the maximum shear modulus of sands containing nonplastic fines. J Geotech Geoenviron Eng 2017;143:06017013.

[15] El Ghoraiby MA, Park H, Manzari MT. Stress-strain behavior and liquefaction strength characteristics of Ottawa F65 sand. Soil Dynam Earthq Eng 2020;138:106292.

[16] Jafarian Y, Mehrzad B, Lee CJ, Haddad AH. Centrifuge modeling of seismic foundation-soil-foundation interaction on liquefiable sand. Soil Dynam Earthq Eng 2017;97:184-204.

[17] Andrus RD, Stokoe IIKH. Liquefaction Resistance of Soils from Shear-Wave Velocity. J Geotech Geoenviron Eng 2000;126:1015-1025.

[18] Idriss IM, Boulanger RW. SPT-Based Liquefaction Triggering Procedures. Report No. UCD/CGM-10/02 2010.

[19] Bouferra R, Shahrour I. Influence of fines on the resistance to liquefaction of a clayey sand. Ground Improvement 2004;8:1-6.

[20] Arab A, Shahrour I, Lancelot L. A laboratory study of liquefaction of partially saturated sand. Journal of Iberian Geology 2011;37:29-36.

[21] Krim A, Arab A, Bouferra R, Sadek M, Shahrour I. Characteristics of cyclic shear behavior of sandy soils: A laboratory study. Arab J Sci Eng 2016;41:3995-4005.

[22] El Ghoraiby MA, Park H, Manzari MT. Physical and mechanical properties of Ottawa F65 sand. In: Model Tests and Numerical Simulations of Liquefaction and Lateral Spreading. 2020. p. 45-67.

[23] Ueda K, Vargas RR, Ueda K. LEAP-Asia-2018: Stress-strain response of Ottawa F65 sand in cyclic torsional shear tests. DesignSafe-CI [publisher], Dataset, doi:10.17603:DS2D40H 2018.

[24] Vargas RR, Ueda K, Uemura K. Influence of the relative density and K0 effects in the cyclic response of Ottawa F-65 sand - cyclic Torsional Hollow-Cylinder shear tests for LEAP-ASIA-2019. Soil Dynam Earthq Eng 2020;133:106111.

[25] Wu J. Liquefaction triggering and post-liquefaction deformation of Monterey 0/30 sand under UNI-directional cyclic simple shear loading. Ph.D dissertation. Department of Civil and Environmental Engineeering, University of California, Berkeley 2002.

[26] Basu D, Pretell R, Montgomery J, Ziotopoulou K. Numerical Simulations of the Effects of Liquefaction on a Retaining Wall using PM4Sand and FLAC. In: LEAP-2020 Proceedings (Under Review). 2021.

[27] Adamidis O, Madabhushi GSP. Post-liquefaction reconsolidation of sand. Proc R Soc A 2016;472:20150745.

[28] Arulanandan K, Sybico JJ. Post-liquefaction Settlement of Sand. In: Proceeding of the Wroth Memorial Symposium. 1992.

[29] Jafarzadeh F, Yanagisawa E. Settlement of Sand Models under Unidirectional Shaking. In: First International Conference on Earthquake Geotechnical Engineering. 1995. p. 693-698.

[30] Su D, Li X-S, Xing F. Estimation of the apparent permeability in the dynamic centrifuge tests. J Geotech Test 2009;32:22-30.

[31] Wang B, Zen K, Chen GQ, Zhang YB, Kasama K. Excess pore pressure dissipation and solidification after liquefaction of saturated sand deposits. Soil Dynam Earthq Eng 2013;49:157-164.

[32] Ueng T-S, Wang Z-F, Chu M-C, Ge L. Laboratory tests for permeability of sand during liquefaction. Soil Dynam Earthq Eng 2017;100:249-256.

[33] Bayoumi A, Karray M, Chekired M. Measurement of Hydraulic Conductivity Variation in Post Seismic Behavior of Sand Using TxSS. In: GeoEdmonton 2018. 2018.

[34] Balakrishnan A. Liquefaction Remediation at a Bridge Site. Ph.D dissertation. Civil Engineering, University of California Davis 2000.

[35] Gao G-y, Xie W, Song J, Wang Y. Prediction of seismic compression of saturated sand considering the ground motion characteristics and variable permeability. Soil Dynam Earthq Eng 2020;130:105971.

[36] Tsaparli V, Kontoe S, Taborda DMG, Potts DM. Vertical ground motion and its effects on liquefaction resistance of fully saturated sand deposits. Proc R Soc A 2016;472:20160434.

[37] Dobry R, El-Sekelly W, Abdoun T. Calibration of non-linear effective stress code for seismic analysis of excess pore pressures and liquefaction in the free field. Soil Dynam Earthq Eng 2018;107:374-389.

[38] Reyes A, Adinata J, Taiebat M. Impact of bidirectional seismic shearing on the volumetric response of sand deposits. Soil Dynam Earthq Eng 2019;125:105665.

[39] Ishihara K, Review of the predictions for Model 1 in the VELACS program. In: K. Arulanandan, R.F. Scott (Eds.), Rotterdam: A.A. Balkema, 1994, pp. 1353-1368.

[40] Manzari MT, Arulanandan K, Numerical Predictions for Model No. 1, AA, Balkema, Rotterdam, 1993.

[41] Ghassemi A, Seyfi S, Shahir H. Evaluation of variable permeability model in simulation of seismic behavior of uniform level and gently sloping sand layers. Earth Sci Res J 2020;24:335-343.

[42] Rahmani A, Ghasemi Fare O, Pak A. Investigation of the influence of permeability coefficient on the numerical modeling of the liquefaction phenomenon. Sci Iran 2012;19:179-187.

[43] Yang M, Barrero AR, Taiebat M. Application of a SANISAND Model for Numerical Simulations of the LEAP 2017 Experiments. In: Model Tests and Numerical Simulations of Liquefaction and Lateral Spreading. 2020. p. 595-610.

[44] Shahir H, Mohammadi-Haji B, Ghassemi A. Employing a variable permeability model in numerical simulation of saturated sand behavior under earthquake loading. Comput Geotech 2014;55:211-223.

[45] Carrier WD. Goodbye, Hazen; Hello, Kozeny-Carman. J Geotech Geoenviron Eng 2003;129:1054-1056.

[46] Hazen A. Discussion of "Dams on Sand Foundations" Transactions 1911;73:199-203.

[47] Terzaghi K, Peck RB, Mesri G, Soil Mechanics in Engineering Practice, 3rd ed., Wiley, New York, 1996.

[48] Beber R, Madabhushi SSC, Dobrisan A, Haigh SK, Madabhushi SPG, LEAP GWU 2017: Investigating Different Methods for Verifying the Relative Density of a Centrifuge Model. In: Physical Modelling in Geotechnics, CRC Press, 2018.

[49] Bartlett SF, Youd TL. Empirical Prediction of Liquefaction-Induced Lateral Spread. J Geotech Eng 1995;121:316-329.

[50] Sadeghi H, Pak A, Pakzad A, Ayoubi P. Numerical-probabilistic modeling of the liquefaction-induced free fields settlement. Soil Dynam Earthq Eng 2021;149:106868.

[51] Geyin M, Maurer BW. An analysis of liquefaction-induced free-field ground settlement using 1,000+ case histories: Observations vs. state-of-practice predictions. In: Geo-Congress 2019 GSP 308. 2019. p. 489-498.

[52] Green RA, Maurer BW, Ballegooy SV, The influence of the non-liquefied crust on the severity of surficial liquefaction manifestations: Case history from the 2016 Valentine's

day earthquake in New Zealand. In: Geotechnical Earthquake Engineering and Soil Dynamics V, 2018, pp. 21-32.

[53] Lewis MR, Arango I, McHood MD, Site characterization philosophy and liquefaction evaluation of aged sands: A Savannah river site and Bechtel perspective. In: From Research to Practice in Geotechnical Engineering, 2008, pp. 540-558.

[54] Bwambale B, Andrus RD. State of the art in the assessment of aging effects on soil liquefaction. Soil Dynam Earthq Eng 2019;125:105658.

6.3 REFERENCES (CHAPTER 3)

[1] Beber R, Madabhushi SSC, Dobrisan A, Haigh SK, Madabhushi SPG, LEAP GWU 2017: Investigating Different Methods for Verifying the Relative Density of a Centrifuge Model. In: Physical Modelling in Geotechnics, CRC Press, 2018.

[2] Arulanandan K, Sybico JJ. Post-liquefaction Settlement of Sand. In: Proceeding of the Wroth Memorial Symposium. 1992.

[3] Su D, Li X-S, Xing F. Estimation of the apparent permeability in the dynamic centrifuge tests. J Geotech Test 2009;32:22-30.

[4] Itasca. FLAC (Version 8.0) – Fast Lagrangian Analysis of Continua. Itasca Consulting Group, Inc., Minneapolis, Minnesota 2016.

[5] Boulanger RW, Ziotopoulou K. PM4Sand (Version 3.1): A sand plasticity model for earthquake engineering applications. Report No. UCD/CGM-17/01, Davis, CA: University of California, Davis. 2017.

[6] El Ghoraiby MA, Park H, Manzari MT. Stress-strain behavior and liquefaction strength characteristics of Ottawa F65 sand. Soil Dynam Earthq Eng 2020;138:106292.

[7] Zeghal M. LEAP-RPI 2020, Version 0.91 Model Specifications. 2019.

[8] Kutter BL. Dynamic centrifuge modeling of geotechnical structures. In: Transportation Research Record, TRB, National Research Council. 1992. p. 24-30.

[9] El Ghoraiby MA, Manzari MT. LEAP 2020: Cyclic direct simple shear tests performed at GWU. DesignSafe-CI [publisher], Dataset, doi: being updated 2019.

[10] El Ghoraiby MA, Park H, Manzari MT. LEAP 2017: Soil characterization and element tests for Ottawa F65 sand. Geotech. Report. The George Washington University, Washington, DC 2017.

[11] El Ghoraiby MA, Park H, Manzari MT. Physical and mechanical properties of Ottawa F65 sand. In: Model Tests and Numerical Simulations of Liquefaction and Lateral Spreading. 2020. p. 45-67.

[12] Lee KL, Seed H. Drained strength characteristics of sands. J Soil Mech Found Div 1967;93:117-141.

[13] Morales B, Ziotopoulou K. Direct simple testing of Ottawa F-65 sand. UC Davis Soil Interactions Laboratory data report 2018.

[14] Ueda K, Vargas RR, Ueda K. LEAP-Asia-2018: Stress-strain response of Ottawa F65 sand in cyclic torsional shear tests. DesignSafe-CI [publisher], Dataset, doi:10.17603:DS2D40H 2018.

[15] Vargas RR, Ueda K, Uemura K. Influence of the relative density and K0 effects in the cyclic response of Ottawa F-65 sand - cyclic Torsional Hollow-Cylinder shear tests for LEAP-ASIA-2019. Soil Dynam Earthq Eng 2020;133:106111.

[16] Idriss IM, Boulanger RW. SPT-Based Liquefaction Triggering Procedures. Report No. UCD/CGM-10/02 2010.

[17] Tasiopoulou P, Ziotopoulou K, Humire F, Giannakou A, Chacko J, Travasarou T. Development and implementation of semiempirical framework for modeling postliquefaction shear deformation accumulation in sands. J Geotech Geoenviron Eng 2020;146:04019120.

[18] Parra Bastidas AM. Ottawa F-65 sand characterization. Ph.D dissertation. Department of Civil and Enviropnmental Engineering, University of California, Davis 2016.

[19] Ashmawy AK, Sukumaran B, Hoang VV, Evaluating the influence of particle shape on liquefaction behavior using discrete element modeling, In: 13th International Offshore and Polar Engineering Conference, Honolulu, HI, USA, 2003, pp. 542-549.

[20] Dennis ND, Influence of specimen preparation techniques and testing procedures on undrained steady state shear strength. In: R.T. Donaghe, R.C. Chaney, M.L. Silver (Eds.), ASTM International, West Conshohocken, PA, 1988, pp. 642-654.

[21] Santamarina JC, Cho GC. Determination of critical state parameters in sandy soils - Simple procedure. J Geotech Test 2001;24:185-192.

[22] Sasitharan S, Robertson PK, Sego DC, Morgenstern NR. Collapse behavior of sand. Can Geotech J 1993;30:569-577.

[23] Sasitharan S, Robertson PK, Sego DC, Morgenstern NR. State-boundary surface for very loose sand and its practical implications. Can Geotech J 1994;31:321-334.

[24] Carraro JAH, Prezzi M, Salgado R. Shear strength and stiffness of sands containing plastic or nonplastic fines. J Geotech Geoenviron Eng 2009;135:1167-1178.

[25] Sukumaran B, Ashmawy AK. Quantitative characterisation of the geometry of discrete particles. Géotechnique 2001;51:619-627.

[26] Carey TJ, Stone N, Kutter BL. Grain size analysis and maximum and minimum dry density testing of Ottawa F-65 sand for LEAP-UCD-2017. In: Model Tests and Numerical Simulations of Liquefaction and Lateral Spreading. 2020. p. 31-44.

[27] Vasko A, El Ghoraiby MA, Manzari MT. LEAP-GWU-2015 Laboratory tests. DesignSafe-CI [publisher], Dataset, doi:10.17603/DS2TH7Q 2018.

[28] Bolton MD, Gui M. The study of relative density effects of cone penetration tests in centrifuge. CUED/D-Soils/TR256 1993.

[29] Adams V, Askenazi A. Building better products with finite element analysis. In: B. Kohl, D. Bentley (Eds.), OnWord Press, 1999.

[30] Ghosh B, Madabhushi SPG. Centrifuge modelling of seismic soil structure interaction effects. Nucl Eng Des 2007;237:887-896.

[31] Basu D, Pretell R, Montgomery J, Ziotopoulou K. Numerical Simulations of the Effects of Liquefaction on a Retaining Wall using PM4Sand and FLAC. In: LEAP-2020 Proceedings (Under Review). 2021.

[32] Jafarzadeh F, Yanagisawa E. Settlement of Sand Models under Unidirectional Shaking. In: First International Conference on Earthquake Geotechnical Engineering. 1995. p. 693-698.

[33] Shahir H, Pak A, Taiebat M, Jeremić B. Evaluation of variation of permeability in liquefiable soil under earthquake loading. Comput Geotech 2012;40:74-88.

[34] Ueng T-S, Wang Z-F, Chu M-C, Ge L. Laboratory tests for permeability of sand during liquefaction. Soil Dynam Earthq Eng 2017;100:249-256.

[35] Bayoumi A, Karray M, Chekired M. Measurement of Hydraulic Conductivity Variation in Post Seismic Behavior of Sand Using TxSS. In: GeoEdmonton 2018. 2018.

[36] Tsaparli V, Kontoe S, Taborda DMG, Potts DM. Vertical ground motion and its effects on liquefaction resistance of fully saturated sand deposits. Proc R Soc A 2016;472:20160434.

[37] Gao G-y, Xie W, Song J, Wang Y. Prediction of seismic compression of saturated sand considering the ground motion characteristics and variable permeability. Soil Dynam Earthq Eng 2020;130:105971.

[38] Adamidis O, Madabhushi GSP. Post-liquefaction reconsolidation of sand. Proc R Soc A 2016;472:20150745.

[39] Ishihara K, Review of the predictions for Model 1 in the VELACS program. In: K. Arulanandan, R.F. Scott (Eds.), Rotterdam: A.A. Balkema, 1994, pp. 1353-1368.

[40] Sadeghi H, Pak A, Pakzad A, Ayoubi P. Numerical-probabilistic modeling of the liquefaction-induced free fields settlement. Soil Dynam Earthq Eng 2021;149:106868.

[41] Geyin M, Maurer BW. An analysis of liquefaction-induced free-field ground settlement using 1,000+ case histories: Observations vs. state-of-practice predictions. In: Geo-Congress 2019 GSP 308. 2019. p. 489-498.

[42] Versluis M. Hydrodynamic pressures on large rock structures. MS thesis. Department of Civil Engineering, TU Delft 2010.

6.4 REFERENCES (CHAPTER 4)

[1] Popescu R, Prevost JH, Deodatis G. Effects of spatial variability on soil liquefaction: some design recommendations. Géotechnique 1997;47:1019-1036.

[2] Montgomery J, Boulanger RW. Effects of spatial variability on liquefaction-induced settlement and lateral spreading. J Geotech Geoenviron Eng 2017;143:04016086.

[3] Baker JW, Faber MH. Liquefaction Risk Assessment Using Geostatistics to account for Soil Spatial Variability. J Geotech Geoenviron Eng 2008;134:14-23.

[4] Vivek B, Raychowdhury P. Probabilistic and spatial liquefaction analysis using CPT data: a case study for Alameda County site. Nat Hazard 2014;71:1715-1732.

[5] Stuedlein AW, Gianella TN, Canivan G. Densification of Granular Soils Using Conventional and Drained Timber Displacement Piles. J Geotech Geoenviron Eng 2016;142:04016075.

[6] Gianella TN, Stuedlein AW. Performance of Driven Displacement Pile–Improved Ground in Controlled Blasting Field Tests. J Geotech Geoenviron Eng 2017;143:04017047.

[7] Bong T, Stuedlein AW. Effect of Cone Penetration Conditioning on Random Field Model Parameters and Impact of Spatial Variability on Liquefaction-Induced Differential Settlements. J Geotech Geoenviron Eng 2018;144:04018018.

[8] Boulanger RW, Ziotopoulou K. PM4Sand (Version 3.1): A sand plasticity model for earthquake engineering applications. Report No. UCD/CGM-17/01, Davis, CA: University of California, Davis. 2017.

[9] Itasca. FLAC (Version 8.0) – Fast Lagrangian Analysis of Continua. Itasca Consulting Group, Inc., Minneapolis, Minnesota 2016.

[10] Stuedlein AW, Gianella T. Drained timber pile ground improvement for liquefaction mitigation. NCHRP IDEA project report 180 2016.

[11] Mahvelati S, Coe JT, Stuedlein AW, Asabere P, Gianella TN. Time-Rate Variation of the Shear Wave Velocity (Site Stiffness) Following Blast-Induced Liquefaction. In: Geo-Chicago GSP 271. 2016.

[12] Mahvelati S, Coe JT, Stuedlein AW, Asabere P, Gianella TN, Kordjazi A. Recovery of small-strain stiffness following blast-induced liquefaction based on shear wave velocity measurements. Can Geotech J 2020;58:848-865.

[13] Bong T, Stuedlein AW. Spatial Variability of CPT Parameters and Silty Fines in Liquefiable Beach Sands. J Geotech Geoenviron Eng 2017;143:04017093.

[14] Stuedlein AW, Bong T. Effect of Spatial Variability on Static and Liquefaction-Induced Differential Settlements. In: Geo-Risk GSP 282. 2017.

[15] Baecher GB, Jaksa MB, Brooker PI, Kaggwa WS. Inaccuracies Associated with Estimating Random Measurement Errors. J Geotech Geoenviron Eng 1999;125:79-80.

[16] Ziotopoulou K, Boulanger RW. Numerical modeling issues in predicting post-liquefaction reconsolidation strains and settlements. In: The 10th International Conference on Urban Earthquake Engineering. 2013.

[17] Howell R, Rathje EM, Boulanger RW. Evaluation of simulation models of lateral spread sites treated with prefabricated vertical drains. J Geotech Geoenviron Eng 2015;141:04014076.

[18] Ishihara K, Yoshimine M. Evaluation of settlements in sand deposits following liquefaction during earthquakes. Soils Found 1992;32:173-188.

[19] Idriss IM, Boulanger RW. Soil liquefaction during earthquakes. Monograph MNO-12 2008.

[20] Gianella TN. Ground improvement and liquefaction mitigation using driven timber piles. Master thesis. Department of Civil and Construction Engineering, Oregon State University 2015.

[21] Boulanger Ross W, Idriss IM. CPT-Based Liquefaction Triggering Procedure. J Geotech Geoenviron Eng 2016;142:04015065.

[22] Arulanandan K, Sybico JJ. Post-liquefaction Settlement of Sand. In: Proceeding of the Wroth Memorial Symposium. 1992.

[23] Jafarzadeh F, Yanagisawa E. Settlement of Sand Models under Unidirectional Shaking. In: First International Conference on Earthquake Geotechnical Engineering. 1995. p. 693-698.

[24] Shahir H, Pak A, Taiebat M, Jeremić B. Evaluation of variation of permeability in liquefiable soil under earthquake loading. Comput Geotech 2012;40:74-88.

[25] Jayaram N, Lin T, Baker JW. A Computationally Efficient Ground-Motion Selection Algorithm for Matching a Target Response Spectrum Mean and Variance. Earthquake Spectra 2011;27:797-815.

[26] Unified hazard tool, https://earthquake.usgs.gov/hazards/interactive.

[27] Nuttli OW, Bollinger GA, Herrmann RB. The 1886 Charleston, South Carolina, Earthquake – A 1986 Perspective. US Geological Survey report 1986.

[28] Kramer SL, Mitchell RA. Ground Motion Intensity Measures for Liquefaction Hazard Evaluation. Earthquake Spectra 2006;22:413-438.

[29] Seed HB, Lee KL. Liquefaction of saturated sands during cyclic loading. J Soil Mech Found Div 1966;92:105-134.

[30] Ishihara K. Liquefaction and flow failure during earthquakes. Géotechnique 1993;43:351-451.

[31] Wu J, Kammerer AM, Riemer MF, Seed RB, Pestana JM. Laboratory study of liquefaction triggering criteria. In: 13th World Conference on Earthquake Engineering. 2004.

[32] Yoshimine M, Nishizaki H, Amano K, Hosono Y. Flow deformation of liquefied sand under constant shear load and its application to analysis of flow slide of infinite slope. Soil Dynam Earthq Eng 2006;26:253-264.

[33] Basu D, Montgomery J, Stuedlein AW. Comparison of post-liquefaction settlements at a liquefaction test site considering numerical and empirical methods. In: 7th International Conference on Earthquake Geotechnical Engineering. 2019.

[34] Chakrabortty P, Popescu R. Numerical simulation of centrifuge tests on homogeneous and heterogeneous soil models. Comput Geotech 2012;41:95-105.